

AD-A041 726

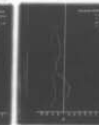
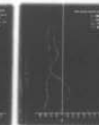
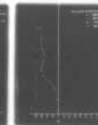
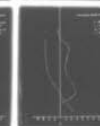
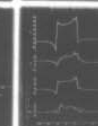
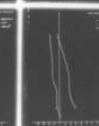
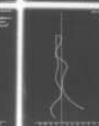
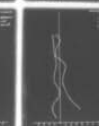
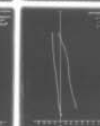
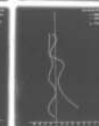
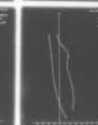
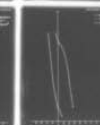
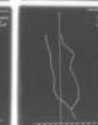
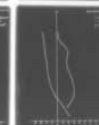
CRANFIELD INST OF TECH (ENGLAND) SCHOOL OF MECHANICA--ETC F/G 20/4
SQUARE-WAVE CIRCUMFERENTIAL PRESSURE DISTORTION EFFECTS IN COMP--ETC(U)
MAR 77 R E PEACOCK

UNCLASSIFIED

AFOSR-TR-77-0075

NL

1 OF 2
AD
A041 726



(Handwritten: 12 B.S.)

AD A 041 726

Cranfield

Institute of Technology

**School of Mechanical Engineering
Thermal Power Group**



(Handwritten signature and date: 17/7/77)

AD No. _____
DDC FILE COPY

DDC
JUL 19 1977
(Handwritten: C.A.S.)



Cranfield Bedford MK43 OAL England
Telephone 0234 - 750111 (Bedford 750111) Telex 825072

Approved for public release
distribution unlimited.

AIR FORCE OFFICE OF SCIENTIFIC RESEARCH (AFSC)

NOTICE OF TRANSMITTAL TO DDC

This technical report has been reviewed and is
approved for public release IAW AFR 190-12 (7b).
Distribution is unlimited.

A. D. BLOGE

Technical Information Officer

(11)

CRANFIELD INSTITUTE OF TECHNOLOGY

FINAL REPORT PREPARED FOR

UNITED STATES AIR FORCE OFFICE OF SCIENTIFIC RESEARCH (AFSC) USA

EUROPEAN OFFICE OF AEROSPACE RESEARCH AND DEVELOPMENT,

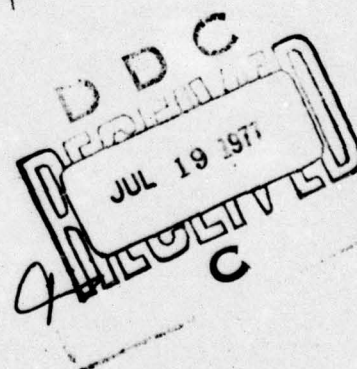
LONDON, GREAT BRITAIN

SQUARE-WAVE CIRCUMFERENTIAL
PRESSURE DISTORTION EFFECTS IN
COMPRESSORS

PRINCIPAL INVESTIGATOR: R.E. PEACOCK

GRANT No. AFOSR-74-~~7~~^{2708 New}
(061345)

ACCESSION FOR	
NTIS	White Section <input checked="" type="checkbox"/>
DDC	Dark Section <input type="checkbox"/>
UNANNOUNCED	
JUSTIFICATION	
BY	
DISTRIBUTION/AVAILABILITY CODES	
Dist.	AVAIL. AND OF SPECIAL
A	



DISTRIBUTION STATEMENT A

Approved for public release;
Distribution Unlimited

The School of Mechanical Engineering
Cranfield Institute of Technology
Cranfield, Bedford, Great Britain.
Telephone: (0234) 750111 Ext. 523

March, 1977

mt

LIST OF CONTENTS

1.0	INTRODUCTION
2.0	OBJECTIVE
3.0	SIGNIFICANCE
4.0	REVIEW OF RIG & INSTRUMENTATION
4.1	The Compressor Rig
4.2	Compressor Blading Aerodynamic Design
4.3	Compressor Blading Manufacture
4.4	Rotor Instrumentation
4.5	Peripheral Instrumentation
5.0	EXPERIMENTAL PROGRAMME
5.1	Undistorted Inlet Flow Experiments
5.2	Distorted Inlet Flow Experiments
6.0	DISCUSSION OF CLEAN INLET FLOW RESULTS
6.1	Overall Characteristics
6.2	Rotor Steady State Pressure Distributions
7.0	DISCUSSION OF DISTORTED FLOW EXPERIMENTS
7.1	Effect of Distortion upon Compressor Performance
7.2	Measurements of Generated Distortions
7.3	Effect of Compressor Throttle Position
7.4	Effect of Screen Porosity upon Distortion Pattern
7.5	Effect of Screen Proximity to Rotor Row
7.6	Detailed Measurements of Distortion at Compressor Open Throttle
7.7	Rotor Response Measurements
8.0	ROTATING STALL OBSERVATIONS
8.1	Rotating Stall with Clean Inlet Flow
8.2	Rotating Stall with High Porosity Screen
9.0	CONCLUSIONS
10.0	REFERENCES
	APPENDIX
	TABLE

1.0. INTRODUCTION

The overall effects of distorting inlet flows to compressors is well known. In general, a reduction in performance is accompanied by a reduced surge margin which can, in certain circumstances, lead to a surge condition. The distortion also creates unsteady cyclic loading on rotor blades which can accelerate fatigue leading to mechanical failure. Further, the cyclic loading can act as a noise generator.

Of the various classes of distortion encountered in compressors, the circumferential distortion is usually reckoned to make the major contribution to performance reduction. Circumferential pressure distortions are often encountered as wakes from upstream struts or objects ahead of intakes: they may also be a component part of a more complex distortion pattern created by a separated flow due to a high angle of incidence or yaw of the intake or through shock wave boundary layer interactions.

The effect of the distortion on the compressor blading does however lead to the changes in overall performance already cited. Because of this, the circumferential pressure distortion in compressor and cascades has been the subject of much mathematical modelling and experimental observation.

It was to investigate the symbiotic relationship between overall performance change and the detailed internal aerodynamics of compressors in the presence of distorted flows that the Cranfield research programme into maldistributed flows in compressors was initiated. Part of that programme involved a detailed investigation of circumferential 'Square-wave' pressure distorted flows and the associated rotor reactions. Support for the programme was through the United States Air Force Grant AFOSR - 74 - 2708, a two-year programme (Ref.1) now concluded after a two-month no cost extension.

This is the final report for that programme and, as such, it records the progress made over the whole period of the research.

2.0. OBJECTIVE

The overall long-term aim of the Cranfield research programme is to produce:-

1. an improved parameter for quantifying distortion.
2. improvements in performance prediction techniques for compressors in quasi-steady distorted flows.
3. a prediction technique for compressors in pulsating flows.
4. a design method that will reduce compressor sensitivity to inlet flow distortions.

This involves an integrated programme of research in which five experimental rigs are being used. In parallel, mathematical models of distorted flows and compressor reactions to them are under development.

The detailed aim of that part of the programme covered by the research grant AFOSR 74-2708 and proposed in Ref. 1 is to examine:-

1. transient rotor response to a range of circumferential square-wave pressure distortions.
2. the flow structure in the distorted flow region.
3. the variation of the overall compressor characteristics and surge line in the presence of inlet circumferential distortion.

3.0. SIGNIFICANCE

An understanding of the dynamic interactions taking place within a compressor in the presence of flow distortions will lead to a mathematical model of the flow. In application this may enhance design procedures so that distortion effects upon performance may be minimised, permitting, for example, higher 'g' aircraft manoeuvres without fear of surge and easing the airframe/engine interactive problems sometimes encountered upon engine installation. Such a model may also be used to predict performance change of a compressor of known geometry.

In order to establish the model, however, there are two vital areas of investigation, both in part forming the core of the research, reported here. These are:

1. the rotor response to an upstream distortion. Early work has indicated a response of a rotor to a square-wave distortion characterised by an initial normal force peak, followed by smaller secondary and tertiary peaks in a dynamic stall situation. From this, recovery is delayed until the rotor is well clear of the region of distorted flow. Clearly the resolution of this mechanism is necessary to help establish the model.
2. the cross-coupling effect between the rotor and the distortion. It has been seen that, because of the rotor reaction, the square wave distortion pattern can take on a non-symmetrical form and, to aid testing techniques, as well as the creation of the model, this must be understood.

4.0. REVIEW OF RIG AND INSTRUMENTATION

4.1. The Compressor Rig

The experimental programme has been executed on a lightly loaded single stage compressor rig. (Plate 1)

The compressor comprised alternative designs of free vortex $\alpha_0 = 0$ blading with rotor chordal lengths of 1.91" or 3.02" (see section 4.2.) No inlet guide vanes were used and in each case, the same stator design was used (see Table 1). The design point rotational speed of the compressor was 1500 rev/min. The annulus was of constant section with a hub/tip ratio of 0.5 and an outer diameter of 20.0". The drive was from an upstream located electric motor (Plate 1) and mass flow was controlled by a throttle valve at the tail-pipe exit (fig. 1).

Since the use of rotor-borne instrumentation was one of the features of the research programme, ready access to the rotor was necessary. This necessitated mounting the tail-pipe assembly on a set of rails for rapid removal.

In order to accommodate the larger chord blades used in the later part of the programme a new rotor disc was manufactured with extended fixing bolts.

4.2. Compressor Blading Aerodynamic Design

The choice of blading used in this exercise is indicated in Table 1.

In each build, a free vortex, $\alpha_0 = 0$ type of blading was used, the only difference being in the rotor blade chord, leading consequently to a different rotor blade thickness and aspect ratio.

The chordal length chosen for the large chord blades allowed design point operation at a Reynolds' No. ($Re = 2.29 \times 10^5$) somewhat above that normally associated with low Reynolds No. effects, and far enough removed from the design point Reynolds No. of the narrow chord blades ($Re = 1.43 \times 10^5$) to show any Reynolds No. effect on the behaviour of the small chord blades. Further, in choosing a chordal length of 3.02" it was possible to build the compressor

with a blade mid-height pitch/chord ratio indentical to that of the small chord blades or alternatively, with a further set of blades of 3.02" chord and smaller hub diameter to build the compressor with the same aspect ratio as that of the small chord blades, using the maximum channel height obtainable on the compressor.

4.3. Compressor Blading Manufacture

The construction adopted for the compressor blades involved a casting technique using a hot-setting epoxy resin sandwich with fibre-glass lay-ups close both to the convex and concave surfaces. The method of manufacture (a multi-stage process in which a surface finish resin was laid in each half mould, followed by fibre-glass lay-ups before the two half moulds were united for the pour of the core resin) introduced voids into the core resin during the final process (Plate 2.) Some development of the casting technique was therefore necessary since the voids led to a rotor blade failure in test.

4.4. Rotor Instrumentation

Of several schemes considered, that initially chosen for the rotor-mounted instrumentation involved mounting transducers at the blade mid-height section on three rotors, the transducers to be encapsulated during the blade casting process. The scheme included machining a section from the mid-height region of a cast blade, fitting the transducers to this and casting a new blade about this section. The acknowledged disadvantage was that a damaged transducer could not be replaced.

During the experimental programme however a fatigue line was propagated from the trailing-edge at the casting interface of the instrumented portion with the newly cast blade, resulting in blade failure. It was not possible to overcome completely the fatigue crack propagation, so a new construction was resorted to.

This led to the design of an entirely new standard of on-rotor instrumentation. It consisted of specially cast blades, each with eight straight bores cast in (Plate 3), a carbon fibre lay up being used for strength. Into each bore was inserted a close fitting tube upon which was mounted a pressure transducer, backed by a sealing ring, the wires from the transducer passing through the tube (Plate 4). The location of the transducer may be seen in Plate 5, just above the static

pressure tapping, drilled after casting the blade. Two blades were used in each experiment (Plate 3). The output from each transducer was fed to a multiplexer board (Plate 6) mounted on the rotor disc where some signal processing was executed before it was passed through a slip-ring assembly to peripheral recording equipment (Plate 1).

This system, used in conjunction with the peripheral instrumentation (section 4.5.) permitted any eight channels of the available sixteen to be transmitted simultaneously. In operation this system proved to be entirely satisfactory and permitted the rapid recording of large quantities of data.

4.5. Peripheral Instrumentation

Instrumentation peripheral to the rig (Plate 1) consisted of potentiometers for bridge balancing of the transducer signals, signal amplifiers and data recording equipment.

As reported in Ref. 2, data could be recorded by several methods. For the experiments reported herein, digital voltmeters were used for time-steady data, cathode ray oscilloscopes were used to monitor transducer out-puts and UV strip recorders were used to make an analogue history of each test.

5.0. EXPERIMENTAL PROGRAMME

A range of experiments has been completed in which measurements were made both in undistorted inlet flow conditions and with a series of upstream screens of varying porosity and sector size. For convenience of presentation these are sub-divided as follows:-

5.1. Undistorted Inlet Flow Experiments

For both builds of compressor (short chord and long chord rotor) the overall characteristic map was measured at 1000, 1250 and 1500 rev/min.

Using the large chord rotor blades and the associated rotor-borne instrumentation, static pressure distributions were measured at the blade mid-height section at 1250 rev/min over a range of mass flows and hence incidences.

During this part of the programme interesting evidence of rotating stall emerged and, following a further investigation, a section is included on this unsteady flow feature.

5.2. Distorted Inlet Flow Experiments

Experiments have been carried out using a range of screens, each having a uniform porosity, but with blockage values varying from screen to screen such that situations both of low blockage (low distortion level) and high blockage (high distortion level) were investigated. A further variable included in the programme was sector angle of the screen which ranged from 75° to 90° .

From the data obtained several effects were isolated and examined. Of these, the effect of the distortion screen upon the compressor characteristic was noted initially. Varying the operating point of the compressor upon its characteristic yielded an understanding of the effect of throttle position upon the distortion propagated by the screen. Since it was found that there appeared to be an effect upon the propagated distortion of the rotor unsteady reaction, tests with different lower blockage screens showed the effect of screen porosity and rotor reaction upon the generated distortion. An investigation of the coupling effect of rotor and distorted screen led to a series of tests in which the axial location of the distortion screen was varied.

Finally, the rotor-borne instrumentation was used to assess the rotor dynamic response to a 90° sector distortion of blockage coefficient $K = 3.813$ (see Appendix 1).

6.0 DISCUSSION OF CLEAN INLET FLOW RESULTS

6.1 Overall Characteristics

The overall characteristic map was evaluated at 1000, 1250 and 1500 rev/min for both long chord and short chord configuration blades. The results are shown superimposed on fig.2.

As well as changes in chordal length, leading to variations in aspect ratio, there was a slight geometric variation in the compressor downstream ducting.

The immediately observable differences are that with the long chord blading there was an extended mass flow range and a movement of the stability limit of the compressor. In each instance, the main contribution could be from the compressor downstream ducting, which, in the instance of the long chord blading, had a lower pressure drop characteristic and also a larger total volume. At any particular mass flow/rotational speed condition the long chord blading produced, in general, a slightly superior pressure ratio.

6.2 Rotor Steady State Pressure Distributions

Using the rotor-borne instrumentation, rotor blade mid-height pressure distributions were measured over a range of mass flows and rotational speeds under steady state (undistorted inlet flow) conditions using the long chord blades. These have been plotted in terms of C_p v chordal position (x/c) where

$$C_p = \frac{p - p_1}{\frac{1}{2} \rho V_1^2}$$

At about the design incidence ($i = -0.4^\circ$) the pressure distribution obtained both for the convex and concave surfaces is plotted in fig.3. Superimposed upon the same figure are data obtained from the short chord blade at $i = 0.2^\circ$ and the predicted distribution gained from a Martensen (Ref. 3) type solution. Slight differences are evident between sets of data but a close, and predictable, similarity exists in the shape of the distributions which follow patterns recognised in cascade flow.

This ordered pattern was not maintained at off-design incidences however. As incidence was reduced to large negative values a series of steady, time-independent, ripples grew progressively on the convex surface (figs. 4 - 18), the pattern being similar at all speeds, and hence Reynolds' Numbers tested ($N = 1000, 1250, 1500$ rev/min.). The range of Reynolds' Number was 1.1×10^5 to 2.2×10^5 . With an increase of incidence from the design point to high positive values, a similar pattern of ripples grew (figs. 19 - 30), differing however in that the location of low pressure peaks became approximately that of previous high pressure peaks and vice versa.

The observations are not immediately recognised as any known two-dimensional phenomena, nor are they predicted by potential flow methods. Earlier work (Ref. 4) of a similar nature using the small chord blades does not record other than smooth pressure distributions in the unstalled regions, except for an isolated case at low Reynolds Number which was attributed to a laminar bubble. Altering the instrumentation by interchanging transducer locations and amplifiers did not alter the data and since, near the design point incidence, predictable results were secured, credence is lent to the instrumentation. It is therefore concluded that the ripples represent real phenomena and are not a product of the instrumentation.

Since these data were recorded on one set of blades, it might be thought that the ripples were a function of the blade geometry. The possibility of waviness in the blade mid-height section contact may be ruled out however because of the opposite sense of the ripples in negative and positive incidence flow and their absence at the design incidence. The low aspect ratio of the blading (1.656) cannot however be ignored since the narrow chord blades, where aspect ratio was 2.618.

An earlier paper (Ref. 4) discusses time-steady measurements at the hub, mid-height and tip sections of the narrow chord blade. In the

absence of the corner separation that characterises the blade convex surface/annulus wall or sidewall and because rotor mid-height stall was delayed to incidences in excess of 15° , it was concluded that strong centrifugal effects on the rotor boundary layers resulted in a radial migration from hub to tip. In the case of the low aspect ratio blading this three-dimensional effect may have been magnified, the secondary distributed circulation sweeping annulus inner wall boundary layer into the convex surface/annulus wall corner and then, by centrifugal force, radially along the convex surface. It can be noted that in general, the concave surface pressure distributions followed a predictable pattern, although at high positive incidence a high pressure ripple appeared at 10-15% chord.

7.0 DISCUSSION OF DISTORTED FLOW EXPERIMENTS

7.1 Effect of Distortion upon Compressor Performance

Experiments with various geometries of distortion screen in the compressor inlet were executed at a compressor speed of 1250 rev/min. In all cases, when compared with that for undistorted flow, the overall characteristic was depressed in terms of overall pressure ratio and fore-shortened in terms of mass flow range, (see for example fig.31). The effect of screen blockage was to reduce the maximum mass flow and the de-stabilizing effect of the distortion was to precipitate the compressor stability limit at a higher mass flow. Such data are in accord with a large body of published work in the literature shewing results from a wide range of compressor designs.

7.2 Measurements of the Generated Distortion

Detailed field measurements were made for three different geometries of distortion screen each individually of uniform porosity (the blockage factor $K = \text{const}$) but with some variation between screens both of K and the sectoral size θ . These were:

1. $K = 0.971$ $\theta = 90^\circ$ (fig.32)
2. $K = 3.183$ $\theta = 75^\circ$ (fig.33)
3. $K = 3.183$ $\theta = 90^\circ$ (fig.34)

Measurements of the annulus mid-height circumferential variation of stagnation and static pressure for each screen are shewn in figs. 32 to 34.

7.3 Effect of Compressor Throttle Position

Since the stagnation pressure drop across a porous screen is a function of the square of the flow velocity, it is to be anticipated that under open throttle conditions (high mass flow) the maximum distortion would have been encountered for any particular screen.

This was so and is shown in figs. 32 - 34 in terms of the stagnation pressure deficit. In all cases as the throttle was closed the distortion level progressively reduced.

The large stagnation pressure deficit encountered at open throttle for the $\theta = 90^\circ$ screen (fig.34) than for the $\theta = 75^\circ$ screen (fig.33) may be attributed to the fact that the latter experiment was executed using the compressor assembly with short chord blades and higher pressure loss tailpipe which restricted the maximum mass flow (fig.2).

7.4 Effect of Screen Porosity upon Distortion Pattern

It is known that the stagnation pressure drop across a screen is a function of its blockage and the different level of distortion encountered at any particular throttle setting using the $K = 0.971$ screen to that of the $K = 3.183$ screens may be attributed to this.

Apart from that fact though, a predominant feature of the stagnation pressure drop curves is the difference in shape between those of the $K = 0.971$ screen, where the blockage was low, and of the $K = 3.183$ screen, where the blockage was comparatively high. In the former case (fig.32) an essentially flat stagnation pressure deficit plot resulted, with moderate asymmetry in the circumferential variation of static pressure. In the latter case (figs. 33, 34) experiments indicated an asymmetry in the stagnation pressure deficit, the stagnation pressure rising with increased θ (circumferential location, increasing in the direction of rotation) from a minimum value shortly after entry to the screen shadow. It has been observed (Ref. 5) that with such a high distortion level, the rotor was forced into a dynamic stall situation. The effect of stall in the rotor row was to increase locally the aerodynamic blockage of the row, reducing the mass flow locally. The local reduction in mass flow was fed through the screen which provided in consequence a lower stagnation pressure drop. In such circumstances it may be seen (fig.33, 34) that the circumferential static pressure distribution became highly asymmetric, a high pressure disturbance continuing well beyond the exit from the screen shadow. Rotor response measurements have shown that the dynamic stall was not suppressed until after exit from the screen shadow. The resulting continuation of the associated aerodynamic blockage may then be equated with this static pressure rise, consequent upon a local upstream velocity reduction.

In fig.34, data for the $K = 3.183$ screen of 90° sectoral size are presented. It has been noted that in these tests a higher open throttle mass flow was obtained and this was reflected in a higher open throttle distortion level downstream of the screen. From velocity triangle considerations it is evident that increased mass flow results in a reduced rotor incidence. In this case then, under open throttle conditions, the steady state operational point of the rotor would have been remote from stall. Although the stagnation pressure deficit was at a maximum, so was the static pressure change and it will be shown (section 7.7) that the flow perturbation on the rotor was not enough to initiate fully stalled flow. Reference to fig.34 of stagnation pressure deficit shows that under open throttle conditions, the slope of the deficit was much lower, tending, in the last 40° of the shadow, to be flat. At the same time the static pressure perturbation beyond the screen shadow was at its smallest, both in terms of magnitude and extent. All these data support the later observation that, at this operational point, the rotor did not stall.

7.5 Effect of Screen Proximity to the Rotor Row

A cross-coupling effect between the rotor response and the screen generated distortion has already been observed (section 7.4) and reported (Ref. 6).

To examine this in more detail, a series of experiments was carried out in which, for otherwise identical conditions the screen axial location was varied (fig.35) relative to the rotor row.

The asymmetry of the field measurements discussed in section 7.4 increased with reduced separation between rotor and screen (fig.36) confirming the cross-coupling relationship postulated. With movements of the screen from the rotor row, some de-coupling was observed but it was not possible, within the geometric limits of the rig, to de-couple completely the screen and rotor response.

The observations indicate that the distortion experienced by a rotor is dependent, not only on the screen geometry and the compressor operating point, but also upon the relative location of screen and rotor.

7.6 Detailed Measurements of Distortion at Compressor Open Throttle

With the large chord rotor blade configuration, the open throttle operating point of the compressor at 1250 rev/min, using the $K = 3.183$, 90° sectoral size screen, was selected for a more detailed investigation.

Annulus mid-height measurements were made of stagnation pressure, static pressure, axial velocity and the associated rotor air angles which are shown in fig.37.

As the screen shadow was approached it is seen that there was an increase of α_0 and an associated fall of incidence. This was a consequence of streamline curvature in the circumferential sense, created by the static pressure drop in the screen shadow with, in addition, a possible component due to the vorticity in the shear flow. The increased axial velocity in this region was due to the increased pumping capacity of the rotor blade at low incidence.

Within the screen shadow, the sharp fall both in stagnation and static pressure was accompanied by a reduced axial velocity and this, with a fall to negative values of α_0 led to an incidence increase from about -2° to a level of about 15° . The mean level of rotor deviation responded by peaking to a level of 25° before settling generally to that of about 19° . Over most of the screen shadow the incidence was approximately constant, though rising toward the screen shadow trailing edge to a maximum of about 24° . This was contributed to both by the low axial velocity and the streamline curvature of the flow and its vorticity in this region, opposite in sense to that at the screen shadow entry.

7.7 Rotor Response Measurements

A series of plots (figs. 38 - 77) indicate the dynamic static pressure distribution measured around the rotor blade at mid-height in the presence of the distortion from a screen of $K = 3.813$ and sector size 90° at open throttle conditions at 1250 rev/min compressor speed.

The progression is best described as the rotor advances from a fairly quiescent phase of unstalled flow to the active phase in the vicinity of the distortion. Taking the reference location of $\theta = 0^\circ$ at the screen leading edge with respect to the advancing rotor, data will be examined from $\theta = 199^\circ$ to $\theta = 360^\circ (= 0^\circ)$ and then progressively to $\theta = 199^\circ$.

At $\theta = 199^\circ$, the pressure distribution is shown in fig.38. For comparison a closely equivalent steady flow pressure distribution has been superimposed: for the distorted flow case the incidence was -3.9° , the Reynolds' Number 1.71×10^5 and the normal force coefficient 0.54. The pressure ripple observed under steady flow conditions at about 60% chord was repeated in the distorted flow experiment and the profiles show generally good agreement. Although no large scale effect occurred until about $\theta = 280^\circ$ (fig.42), the pressure distribution was never totally quiescent, small scale fluctuations altering slightly its shape. The overall effect on the normal force coefficient, defined as

$$C_N = \int_{t.e}^{l.e} p \, dx$$

and plotted for all circumferential positions in fig.78 was negligible.

Reference to fig.37 shows that from about $\theta = 300^\circ$ to 360° an increase in α_0 - curvature of the inflow towards the screen centre-line - resulted in a reduction of rotor incidence. Rotor response was mainly confined to the leading-edge region where the convex and concave pressure distributions crossed in the manner associated with low incidence operation (e.g. fig.48). The peak depression on the convex surface reduced progressively and this was reflected in a reducing normal force coefficient.

The shear flow at the leading edge of the screen shadow was intercepted at $\theta = 354^\circ$ (fig.48) due to the diffusion of the shear flow region downstream of the screen. At this point, the rotor pressure distribution began to fill out (fig.49) resulting in a rise of the normal force coefficient (fig.51) to a maximum of 0.65 at $\theta = 360^\circ$. This corresponded to a, locally, minimum velocity and was followed by a reduced normal force coefficient. The pressure distributions did not follow the same

dynamic pattern as those for the narrow chord blade under closely analogous conditions. With the narrow chord blades (Ref. 6) a wave was observed to pass from the leading towards the trailing edge, followed by a collapse of the pressure distribution into what was described as a dynamic stall. With the wide chord blades however, figs. 47 to 54 indicate what may be described as a bodily shift of the profiles upon which were superimposed relatively small scale disturbances.

In the region about $\theta = 90^\circ$ the final increase in incidence to its maximum created a further leading edge disturbance (fig.66) that yielded a corresponding peak in normal force coefficient. From this high level, the normal force coefficient reduced to a low level (fig.78).

In fig.78 it is observed that the mean level of normal force coefficient in the screen shadow was greater than that in the undistorted flow region. From this it may be concluded that the result throughout of the increased incidence was increased normal force coefficient, suggesting that stall was not encountered.

It may be noted in fig.37 that over a substantial part of the distortion region the incidence was not greater than $+15^\circ$, this being exceeded only towards the trailing edge of the shadow when it reached, momentarily, $+25^\circ$. In Ref.4 it was shewn that this blade section operated successfully as a compressor rotor at incidences as high as $+15^\circ$ without stall.

The conclusion that in the case of the long chord blades no stall was encountered accounts both for the dissimilarity with the narrow chord blade results and the observed reaction of the rotor pressure distributions in acting in a quasi-steady manner. Further, such a conclusion is in accordance generally with the observed stagnation pressure deficit plot under open throttle conditions (fig.34).

8.0 ROTATING STALL OBSERVATIONS

8.1 Rotating Stall with Clean Inlet Flow

At a compressor speed of 1250 rev/min a series of rotating stall observations was made with clean inlet flow conditions.

It was observed that if the compressor was run up from stationary with a fairly closed throttle setting, the operation was accompanied throughout by rotating stall. At 1250 rev/min the rotating stall decayed as the throttle was opened. On closing the throttle again though, it was necessary to go slightly beyond the original throttle setting before rotating stall was again established in the rotor row.

As may be anticipated with this class of compressor, the stability limit was a rotating stall instability, but this experiment indicates that the location of limit of stability moved, depending upon the direction from which it was approached. Further, it suggests that a higher rotor pressure rise is needed to initiate a rotating stall than to sustain it.

8.2 Rotating Stall with High Porosity Screen

It has been shown that the limit of stability moved with the introduction of a high porosity screen (fig.31). Measurements on the rotor blade surfaces of the rotating stall indicated that the stall cell, once created, passed straight through the screen shadow. Its periodicity was at about one half compressor rotational speed.

With an increase in screen blockage, the rotating stall cell was observed not to pass through the screen shadow, but to be terminated at it.

9.0 CONCLUSIONS

A low speed lightly loaded single stage compressor rig has been modified, re-bladed and fitted with on-rotor instrumentation and peripherals to record time steady and unsteady rotor aerodynamic behaviour. It has been used over a range of experiments both with clean inlet flows and with circumferential pressure distortions generated by upstream screens. The results have been compared with similar experiments using blades of shorter chordal length.

Under clean inlet flow conditions it was found that

- close to the design incidence the wide chord rotor pressure distributions agreed well, both with a similar experiment using narrow chord blades and with mathematical predictions.
- at high or low incidence, ripples, particularly in the convex surface pressure distribution, appeared. These could not be explained either by instrumentation errors or two-dimensional aerodynamics and it was tentatively suggested that they were a three-dimensional phenomenon consequent upon the low aspect ratio of the blading.

Measurements of screen generated distortions indicated that the level and shape of the distortion was dependent upon

- screen porosity
- operating point of the compressor on its characteristic
- screen proximity to the rotor row
- a cross-coupling between the rotor aerodynamics and the screen.

On-rotor measurements while operating open throttle at compressor speed of 1250 rev/min with a high blockage screen shewed

- that the rotor row did not enter into a dynamic stall condition as in a previously reported experiment with the narrow chord rotor blades.

Rotating stall observations indicated that

- the stability limit of the compressor was a rotating stall instability
- the location of the rotating stall limit depended upon the compressor path in approaching it
- the threshold level of rotor pressure rise for rotating stall was greater than the sustaining level.

REFERENCES

1. R.E.Peacock 'Square-Wave Circumferential Pressure Distortion Effects in Compressors'
Research Proposal 950:REP:103:B.
The Cranfield Institute of Technology,
Cranfield, U.K. 1974
2. R.E.Peacock 'Square-Wave Circumferential Pressure Distortion Effects in Compressors'
AFOSR 74-2708 Annual Scientific Report No.1.
The Cranfield Institute of Technology,
Cranfield, U.K. 1975
3. E.Martensen 'The Calculation of the Pressure Distribution of Thick Airfoils by Means of Fredholm Integral Equations of the Second Kind'
NASA TT F-702 July 1971
4. R.E.Peacock 'Incidence Effects & Corner Stall Suppression on Rotor Blades in Compressors'
J.Øverli
Fourth Canadian Congress of Applied Mechanics
École Polytechnique, Montreal, Canada 1973
5. R.E.Peacock 'Dynamic Internal Flows in Compressors with Pressure Maldistributed Inlet Conditions'
J.Øverli
46th P.E.P. Conference of AGARD
Monterey, California 1975
6. R.E.Peacock 'Cross-Coupling Effects between Distortion Screens & Rotors in Compressors'
B.F.J.Cossar
Fifth Canadian Congress of Applied Mechanics
Fredicton, New Brunswick, Canada 1975
7. E.P.Bruce 'Design & Evaluation of Screens to Produce Multi-Cycle $\pm 20\%$ Amplitude Sinusoidal Velocity Profiles'
AIAA 8th Aerodynamic Testing Conference
Bethesda, Maryland July 1974

APPENDIX

The Screen Blockage Factor has been defined (Ref.7)

by
$$K = \frac{cs}{(1-s)^2}$$

where c = loss coefficient of the screen
 s = solidity of the screen

In terms of d = the wire diameter of the screen
 m = the spacing between the centres of wires of a square mesh screen

$$s = 2 \left[\frac{d}{m} \right] - \left[\frac{d}{m} \right]^2$$

The values of K quoted in the text are based upon experimental evaluation of c .

TABLE 1

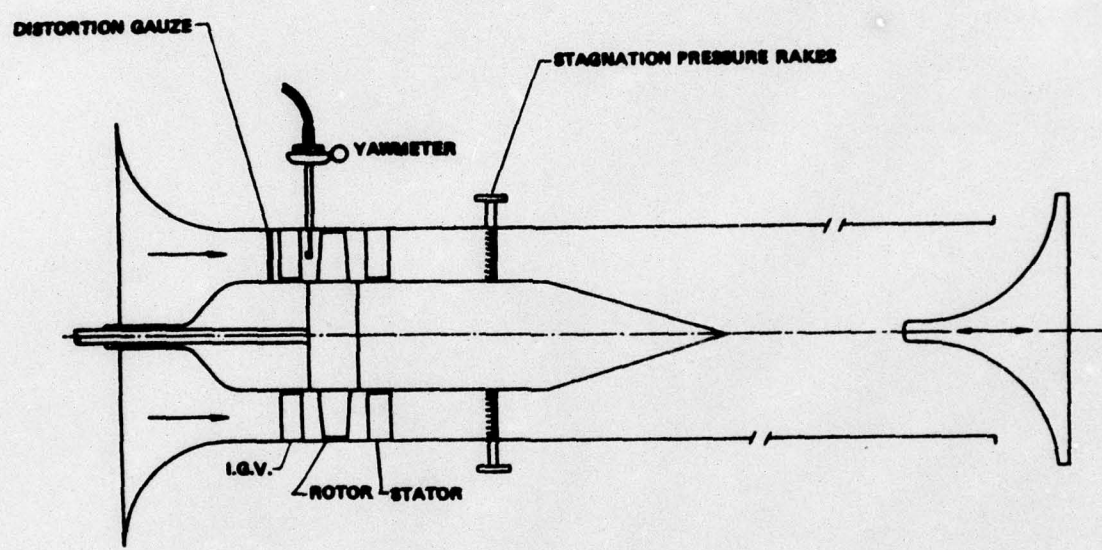
COMPRESSOR BLADING DETAILS

TABLE 1

	Rotors						t/c = 0.12						Stators						t/c = 0.10					
Diameter ins	10.2	12.46	14.6	15.0	17.03	19.4	10.2	12.46	14.6	15.0	17.03	19.4	10.2	12.46	14.6	15.0	17.03	19.4	10.2	12.46	14.6	15.0	17.03	19.4
θ	52.4	38.6	29.6	28.6	23.3	17.0	53.2	47.6	43.0	42.4	39.4	36.0	53.2	47.6	43.0	42.4	39.4	36.0	53.2	47.6	43.0	42.4	39.4	36.0
γ	-9.2	21.6	30.9	31.8	38.3	45.0	13.6	13.0	11.9	11.7	10.5	-9.0	13.6	13.0	11.9	11.7	10.5	-9.0	13.6	13.0	11.9	11.7	10.5	-9.0
β_1	35.4	40.9	45.7	46.1	49.9	53.5	40.2	36.8	33.4	32.9	30.2	27.0	40.2	36.8	33.4	32.9	30.2	27.0	40.2	36.8	33.4	32.9	30.2	27.0
β_2	16.9	2.2	16.1	17.5	26.6	36.5	13.0	10.8	-9.6	-9.5	-9.2	-9.0	13.0	10.8	-9.6	-9.5	-9.2	-9.0	13.0	10.8	-9.6	-9.5	-9.2	-9.0
S/c	.623	.761	.898	.917	1.04	1.18	.615	.750	.886	.905	1.04	1.18	.615	.750	.886	.905	1.04	1.18	.615	.750	.886	.905	1.04	1.18

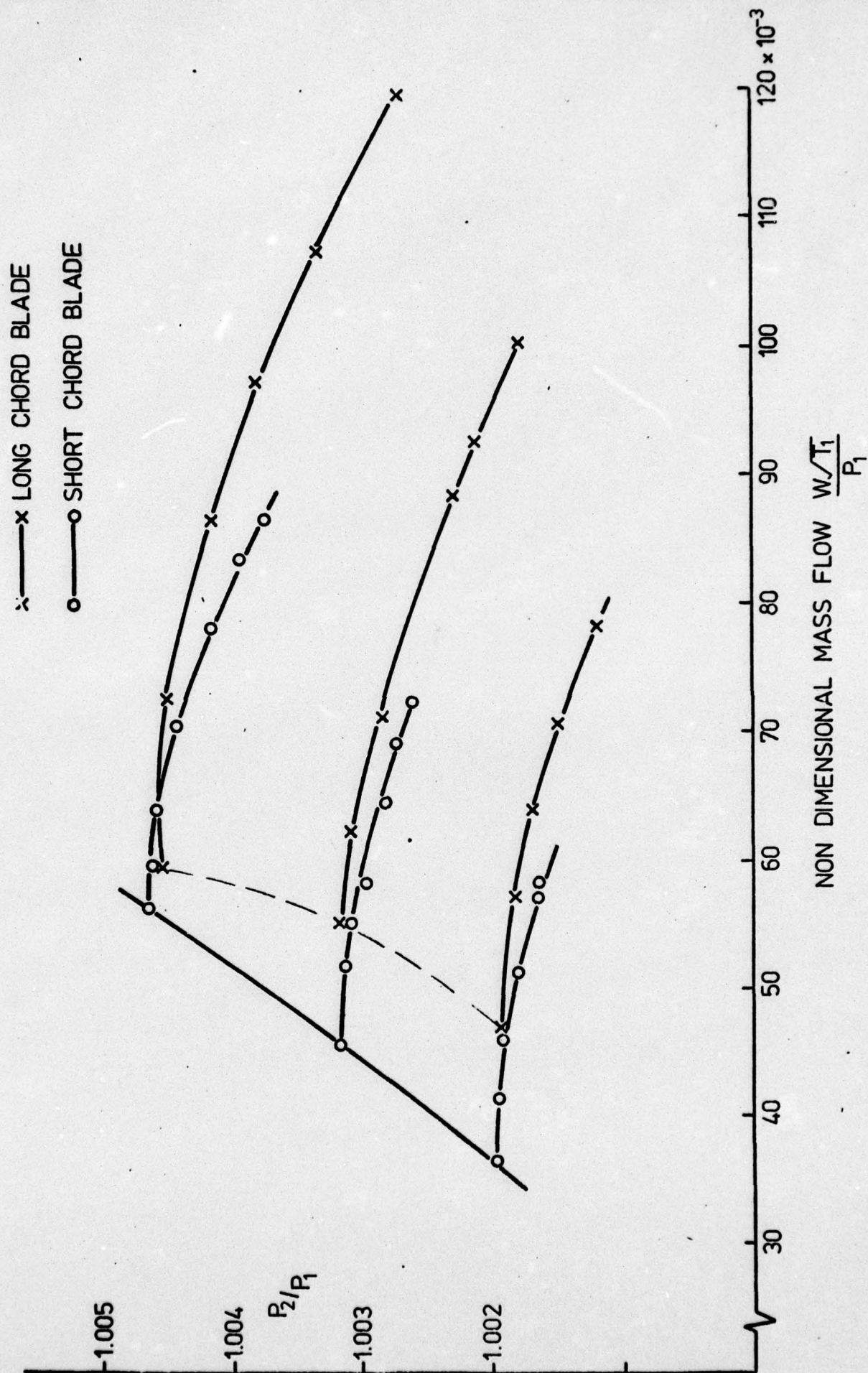
	Chord Ins	No. of Blades	$R_e \times 10^5$	Aspect Ratio
Stators:	1.86	28	1.39	2.69
Rotors:	1.91	27	1.43	2.618
Short Chord	3.02	17	2.29	1.656
Long Chord				

SECTIONAL VIEW OF COMPRESSOR

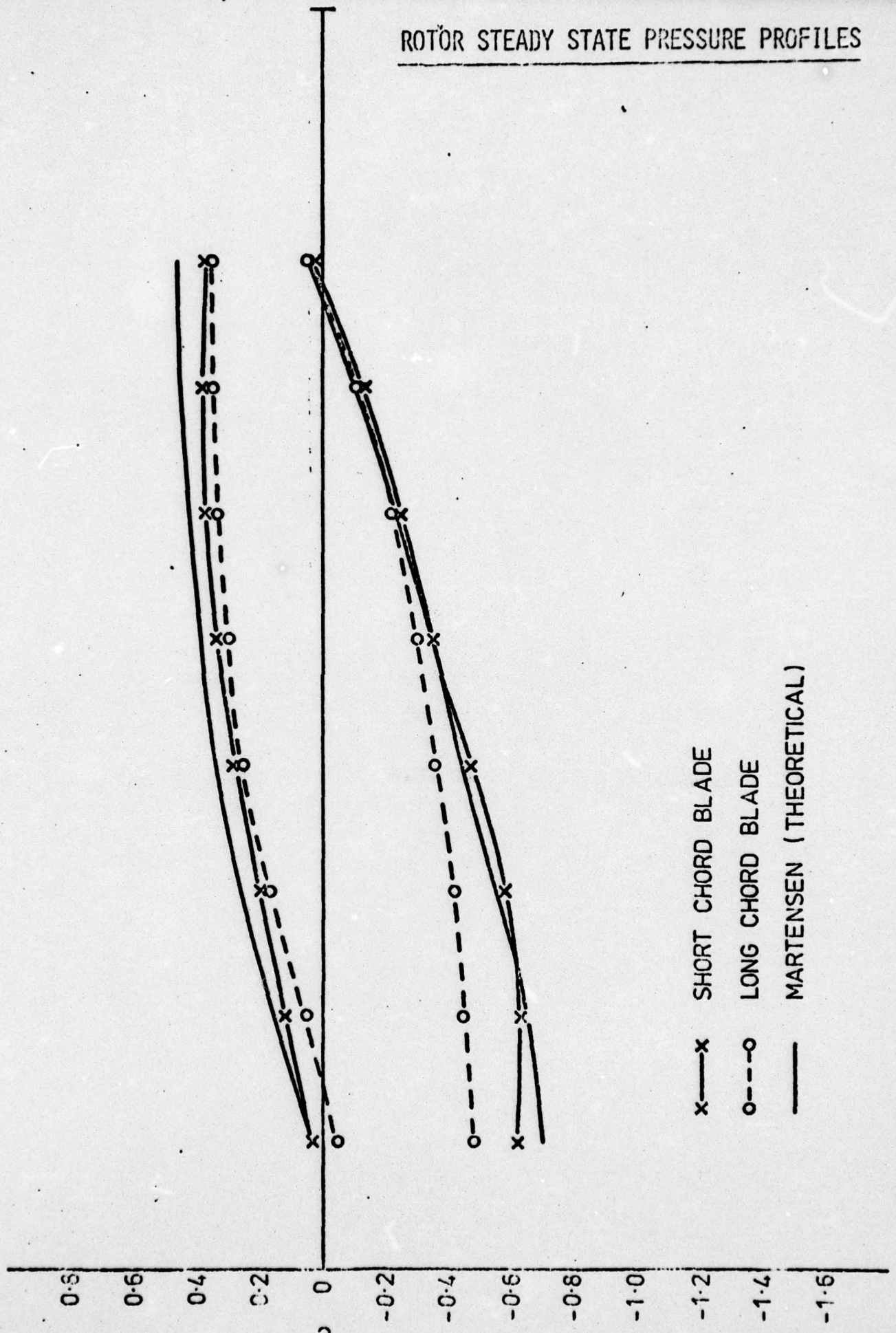


OVERALL CHARACTERISTIC MAP FOR SHORT AND LONG CHORD BLADING

FIG. 2



ROTOR STEADY STATE PRESSURE PROFILES

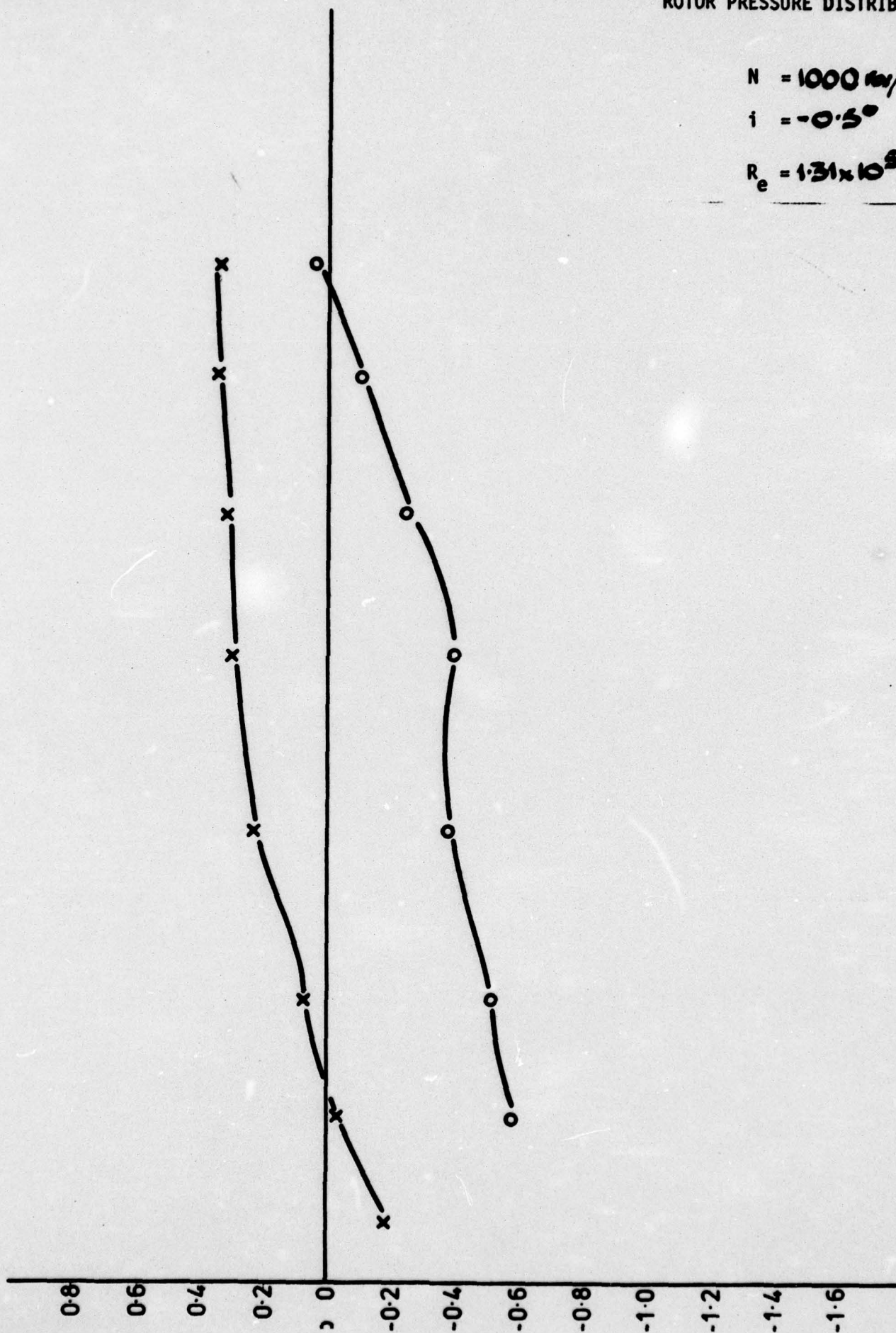


ROTOR PRESSURE DISTRIBUTION

$N = 1000 \text{ rev/min}$

$i = -0.5^\circ$

$R_e = 1.31 \times 10^5$

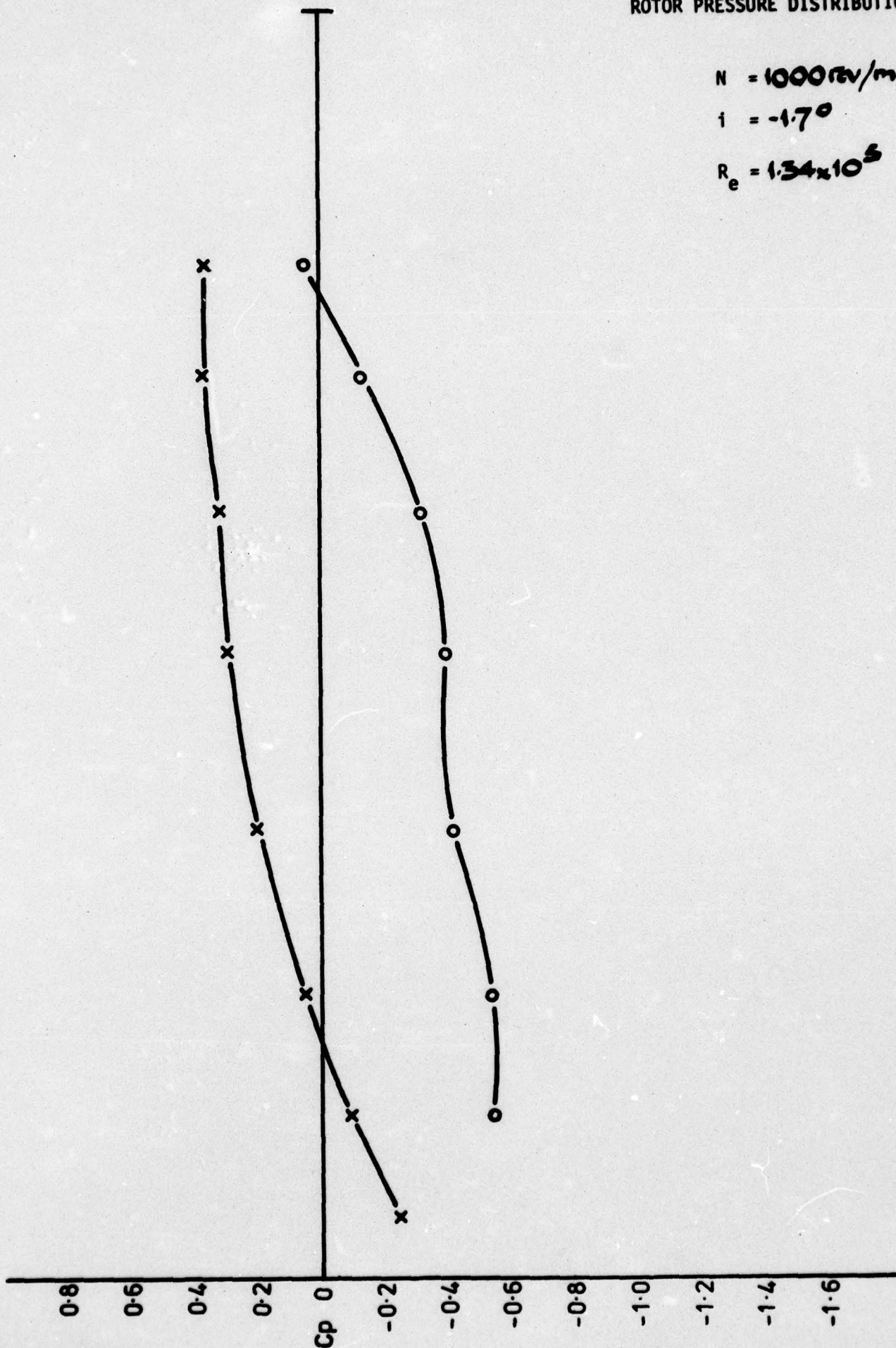


ROTOR PRESSURE DISTRIBUTION

$N = 1000 \text{ rev/min}$

$\Gamma = -1.7^\circ$

$R_e = 1.34 \times 10^5$

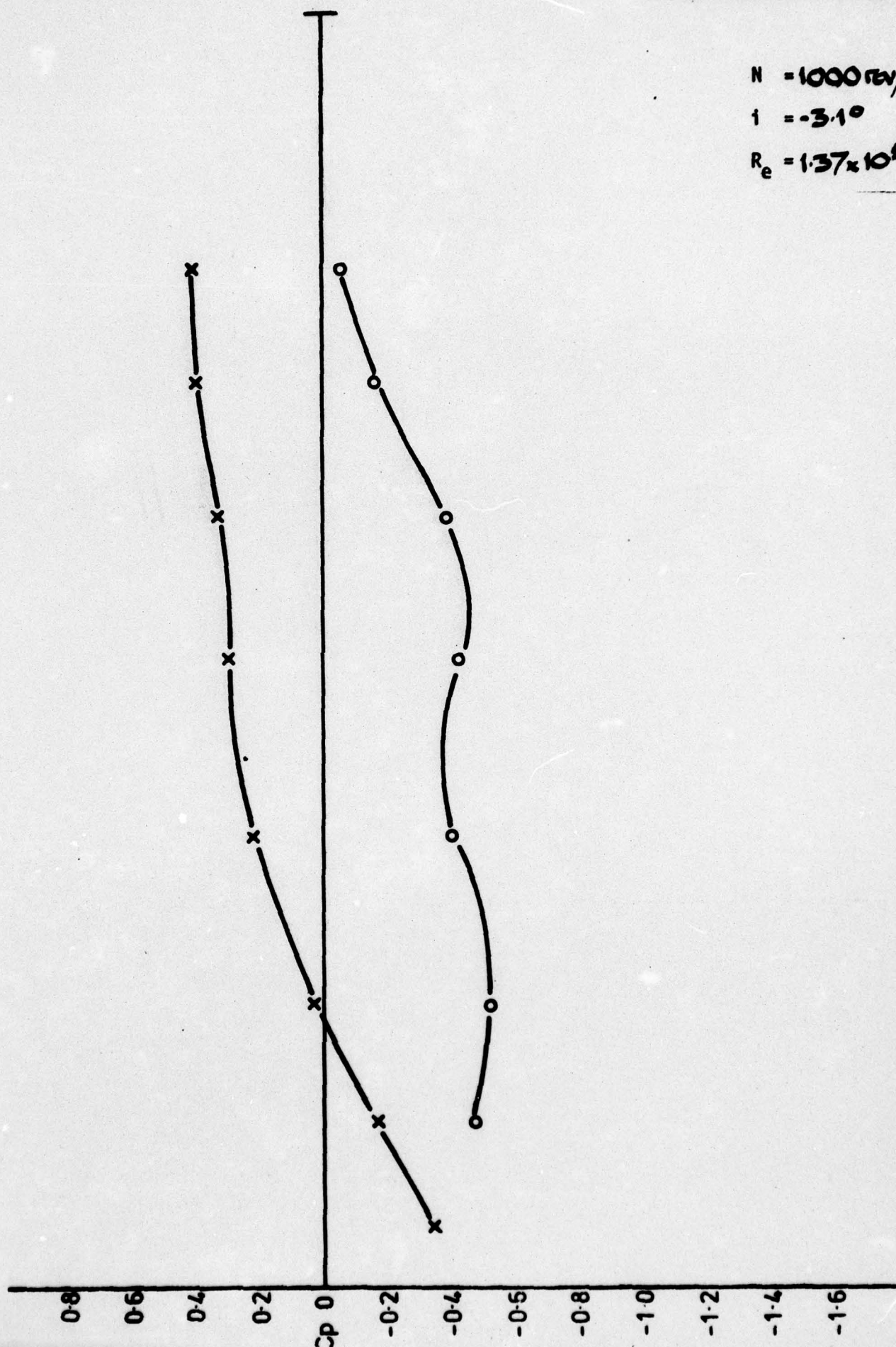


ROTOR PRESSURE DISTRIBUTION

$N = 1000 \text{ rev/min}$

$i = -3.1^\circ$

$R_e = 1.37 \times 10^5$

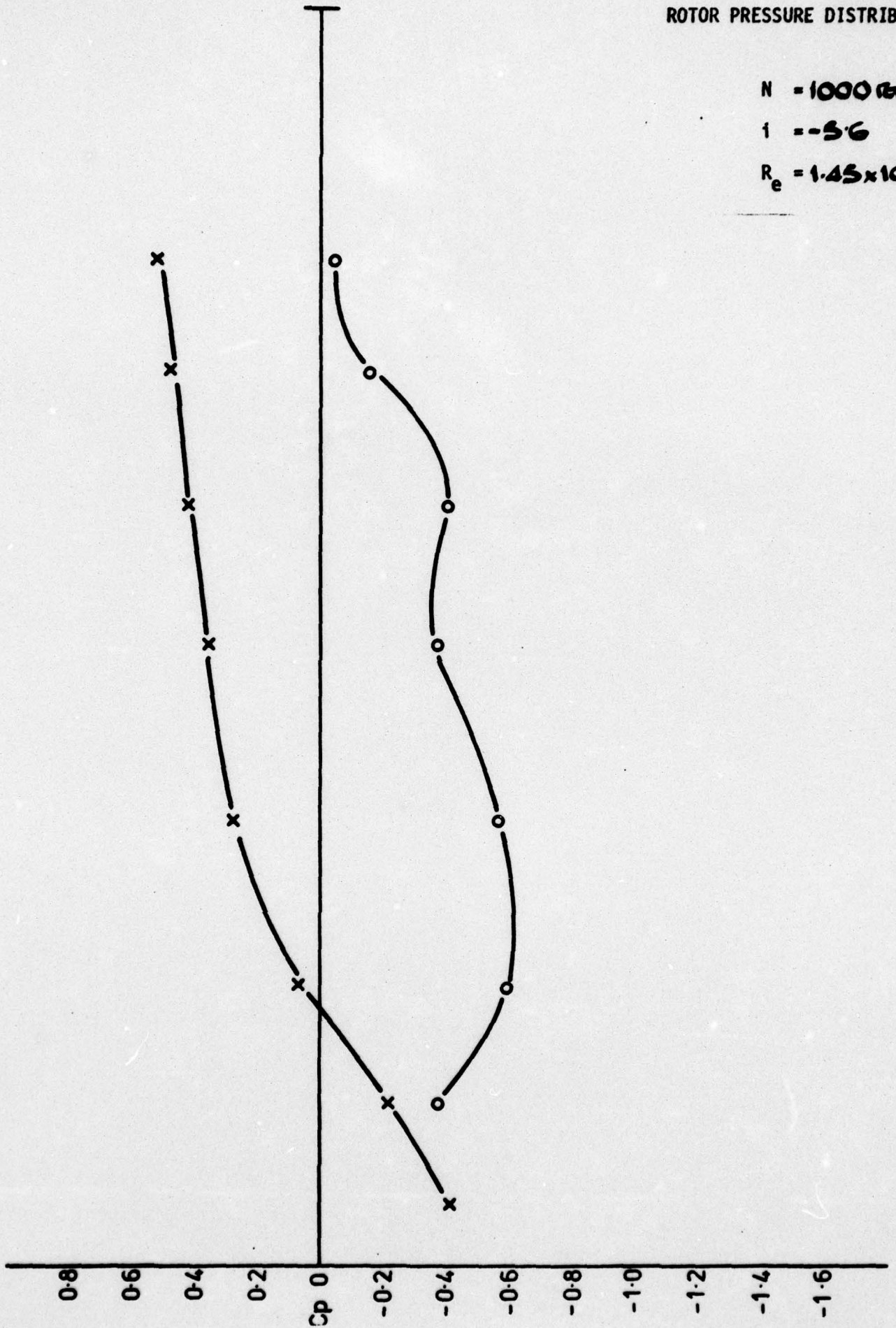


ROTOR PRESSURE DISTRIBUTION

$N = 1000 \text{ rev/min}$

$i = -5.6$

$R_e = 1.45 \times 10^6$

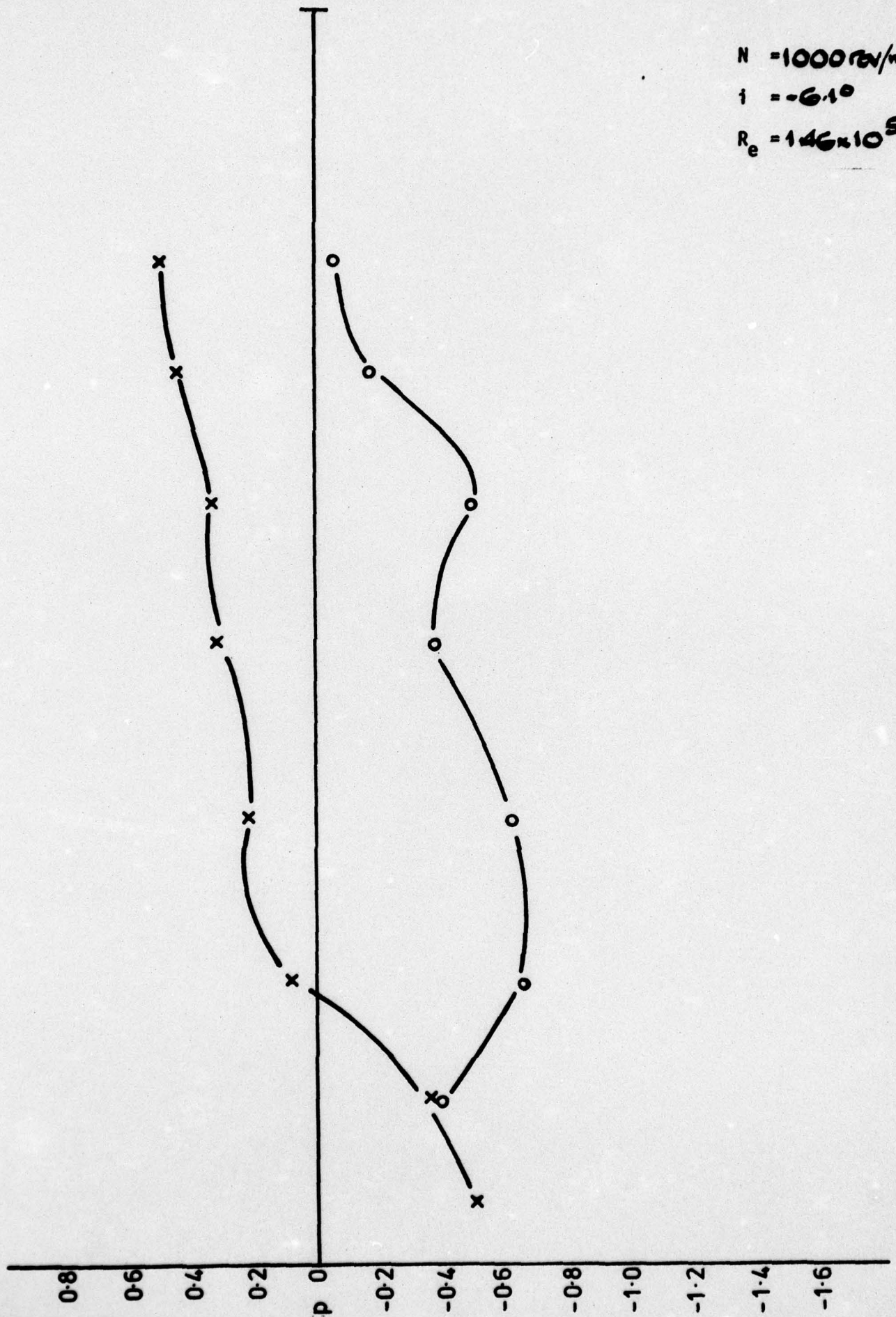


ROTOR PRESSURE DISTRIBUTION

$N = 1000 \text{ rev/min}$

$i = -6.1^\circ$

$R_e = 146 \times 10^5$

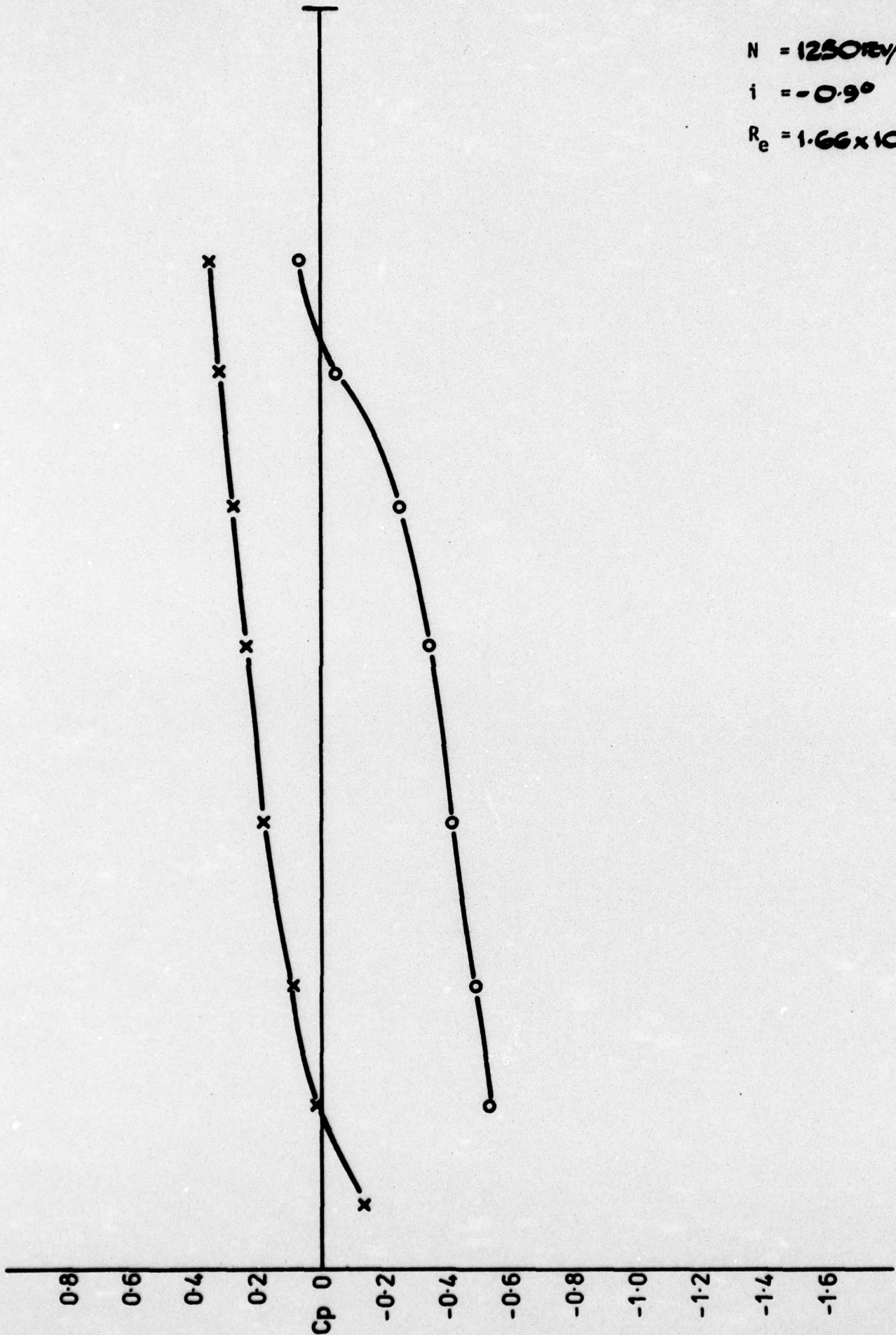


ROTOR PRESSURE DISTRIBUTION

$N = 1250 \text{ rev/min}$

$i = -0.9^\circ$

$R_e = 1.66 \times 10^6$

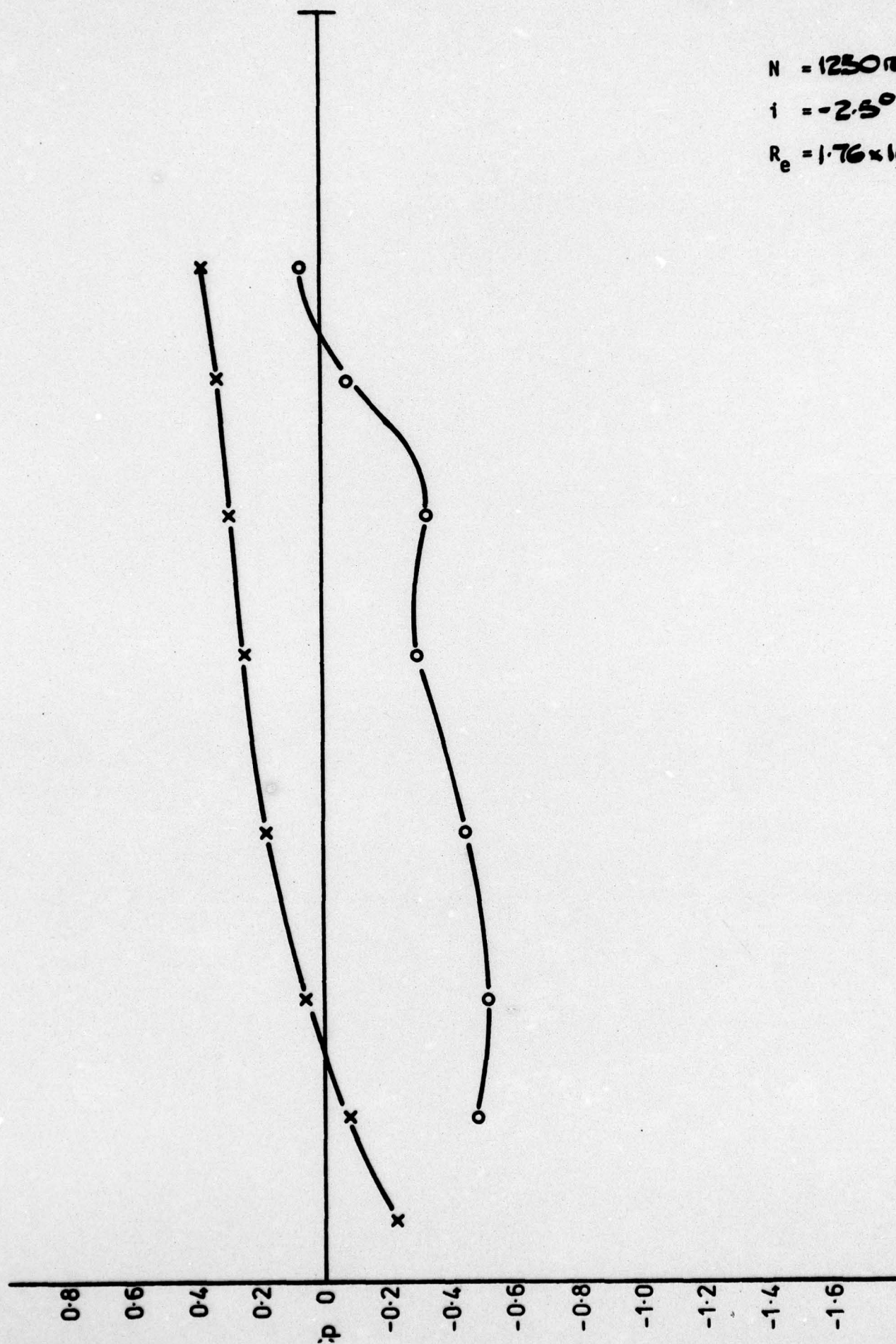


ROTOR PRESSURE DISTRIBUTION

$N = 1250 \text{ rev/min}$

$i = -2.5^\circ$

$R_e = 1.76 \times 10^6$

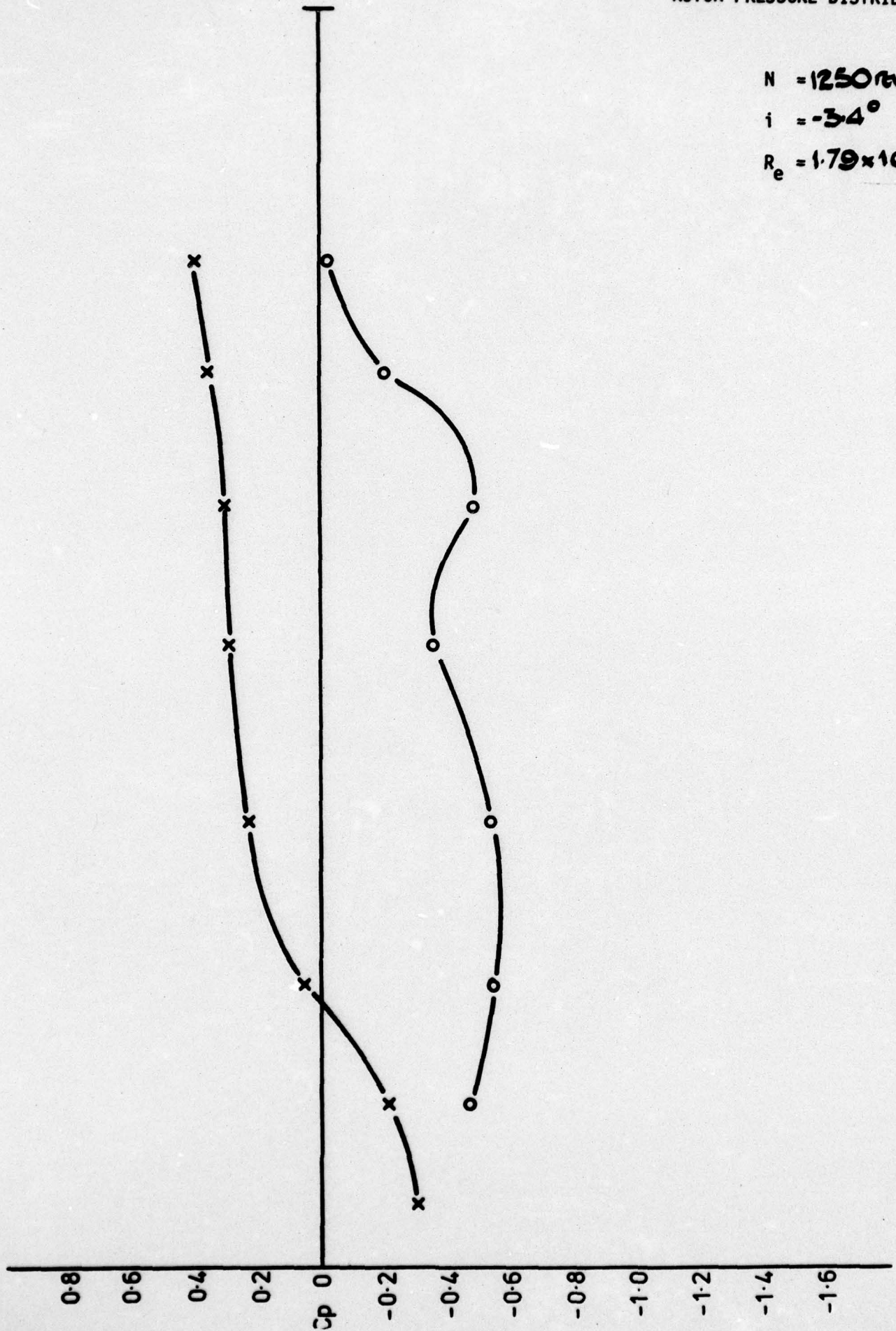


ROTOR PRESSURE DISTRIBUTION

$N = 1250 \text{ rev/min}$

$i = -34^\circ$

$R_e = 1.79 \times 10^5$

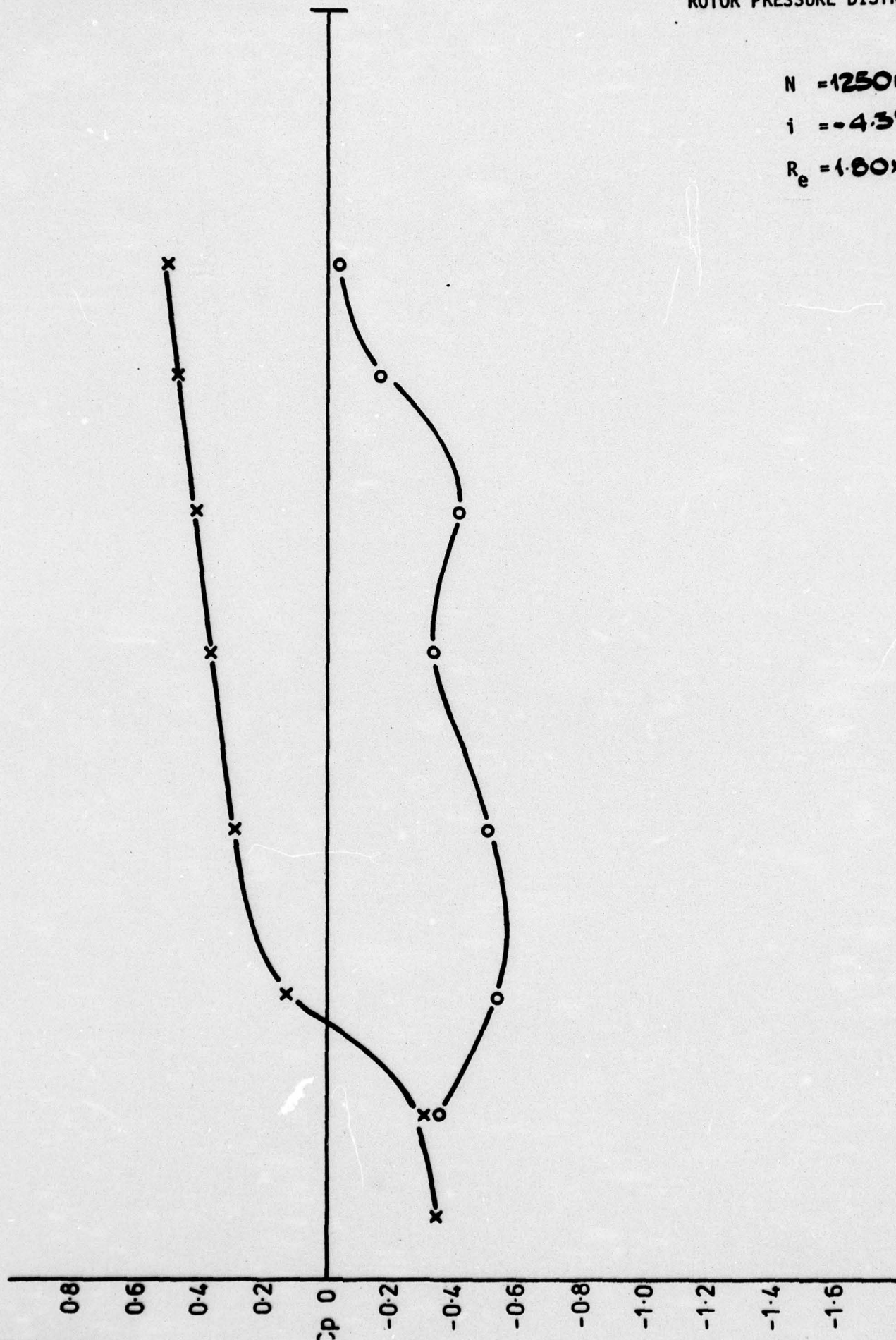


ROTOR PRESSURE DISTRIBUTION

$N = 1250 \text{ rev/min}$

$i = -4.3^\circ$

$R_e = 1.60 \times 10^6$

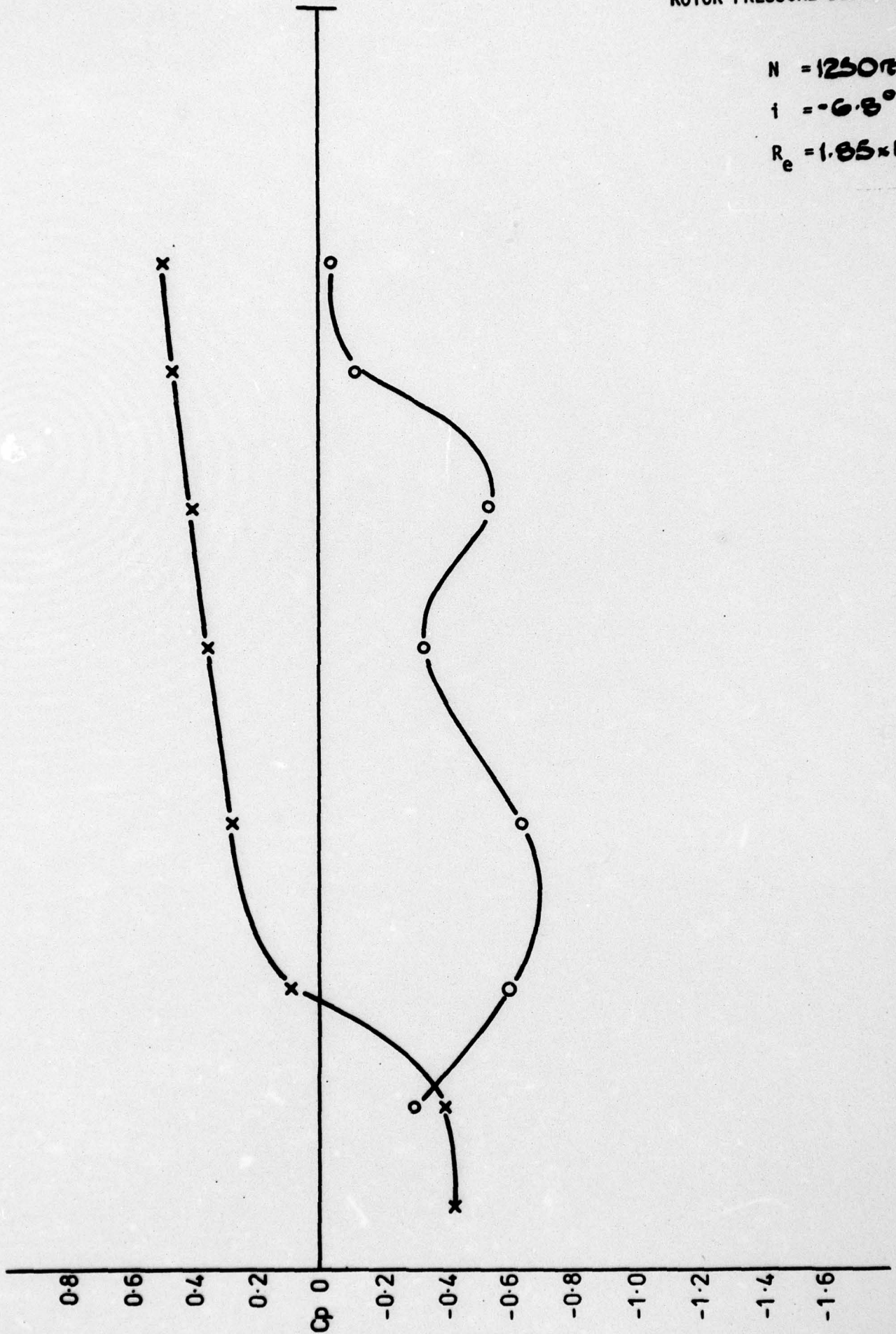


ROTOR PRESSURE DISTRIBUTION

$N = 1250 \text{ rev/min}$

$i = -6.8^\circ$

$R_e = 1.85 \times 10^6$



ROTOR PRESSURE DISTRIBUTION

$N = 1500 \text{ rev/min}$

$i = -0.5^\circ$

$R_e = 1.99 \times 10^6$

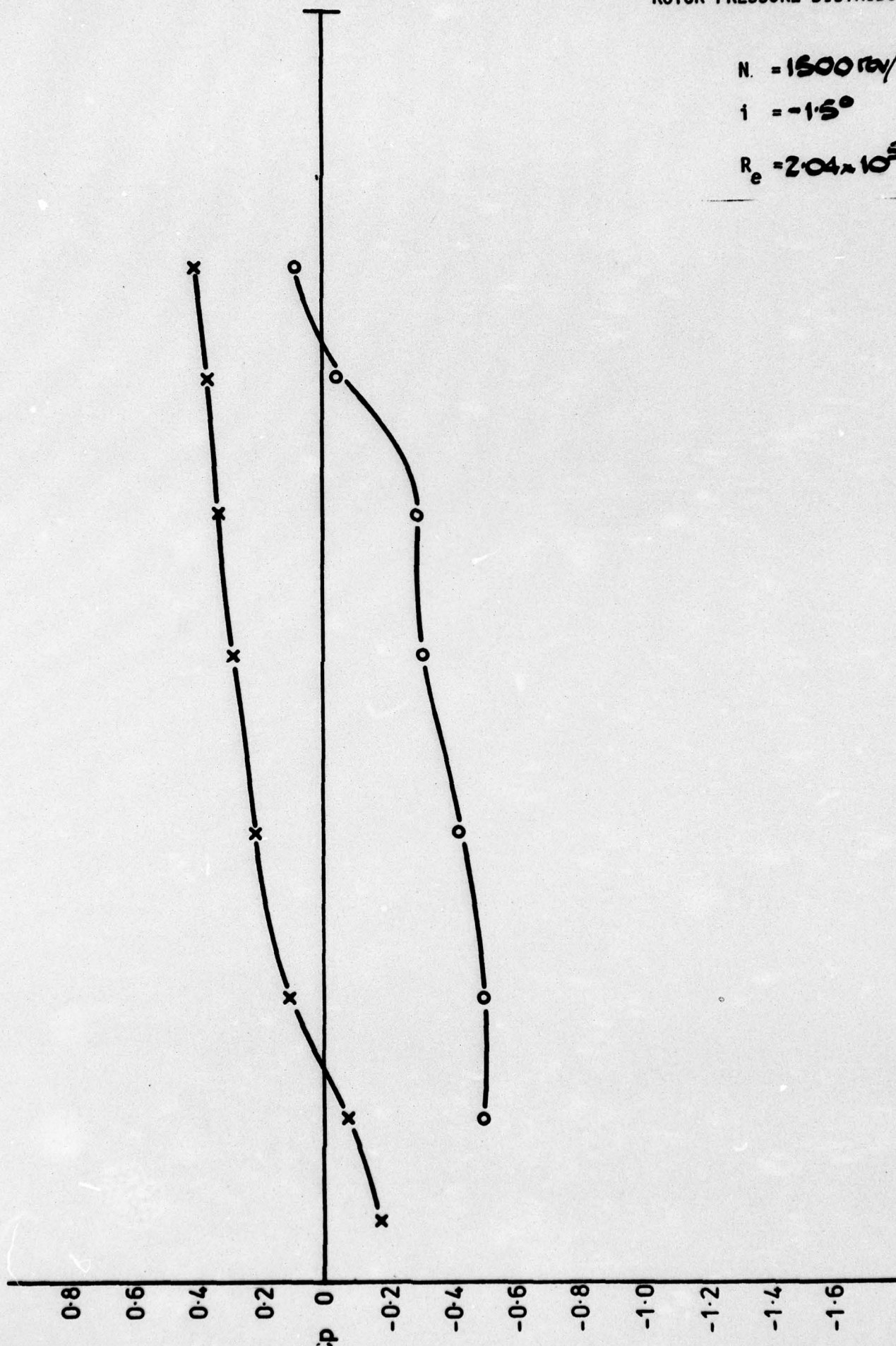


ROTOR PRESSURE DISTRIBUTION

$N = 1500 \text{ rev/min}$

$i = -1.5^\circ$

$R_e = 2.04 \times 10^5$

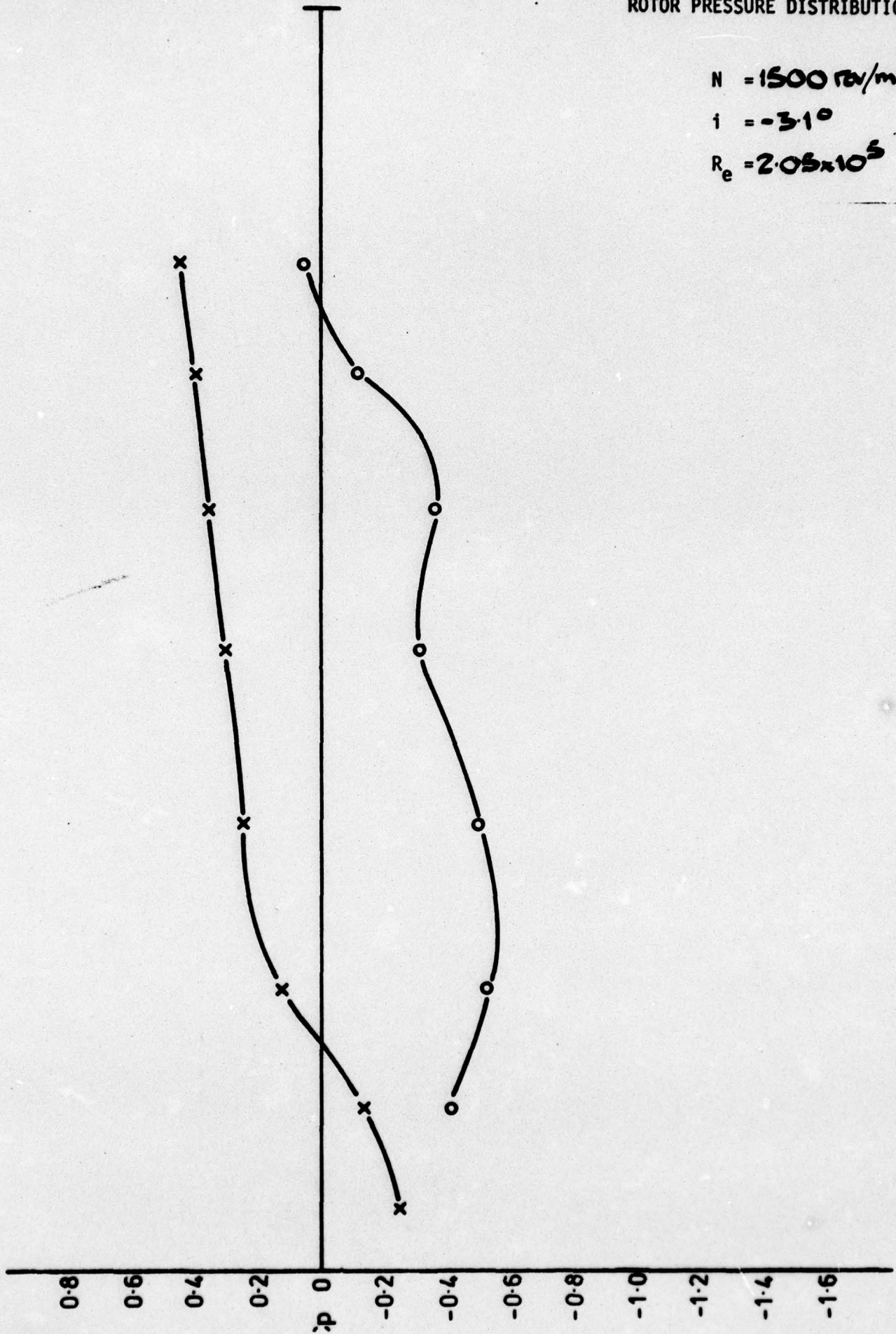


ROTOR PRESSURE DISTRIBUTION

$N = 1500 \text{ rev/min}$

$i = -3.1^\circ$

$R_e = 2.05 \times 10^5$

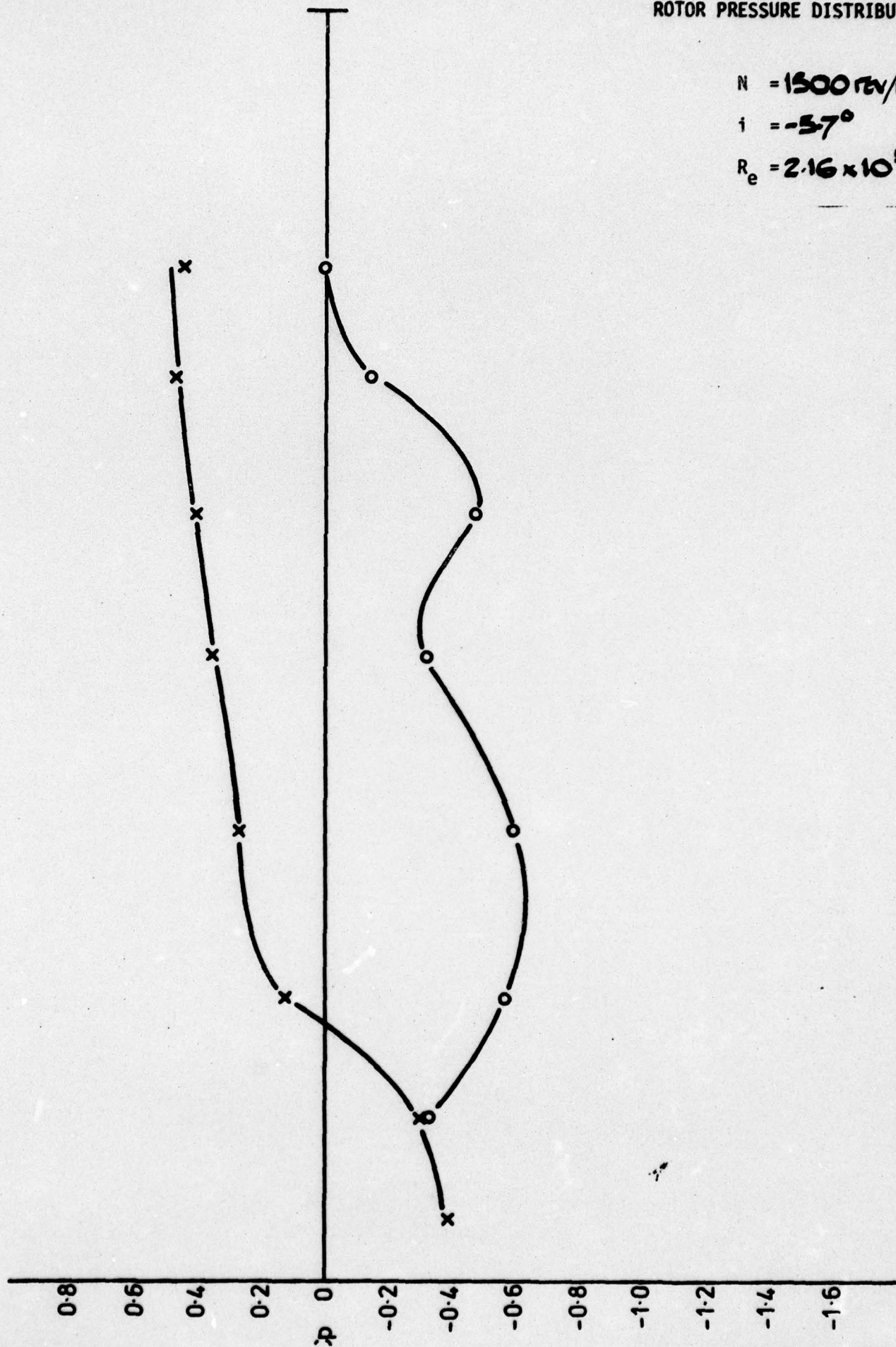


ROTOR PRESSURE DISTRIBUTION

$N = 1500 \text{ rev/min}$

$i = -5.7^\circ$

$R_e = 2.16 \times 10^5$

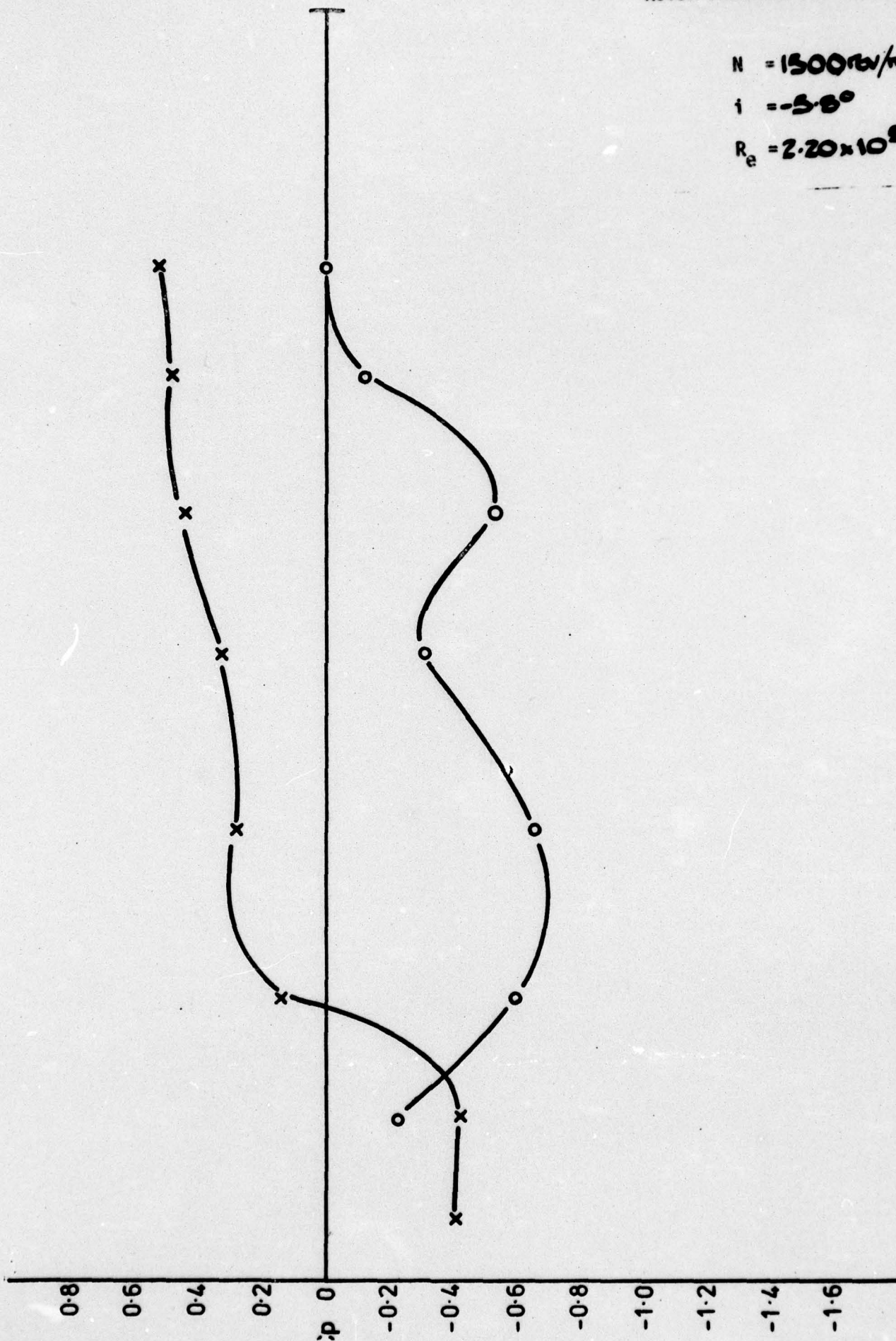


ROTOR PRESSURE DISTRIBUTION

$N = 1500 \text{ rev/min}$

$i = -5.8^\circ$

$R_e = 2.20 \times 10^8$

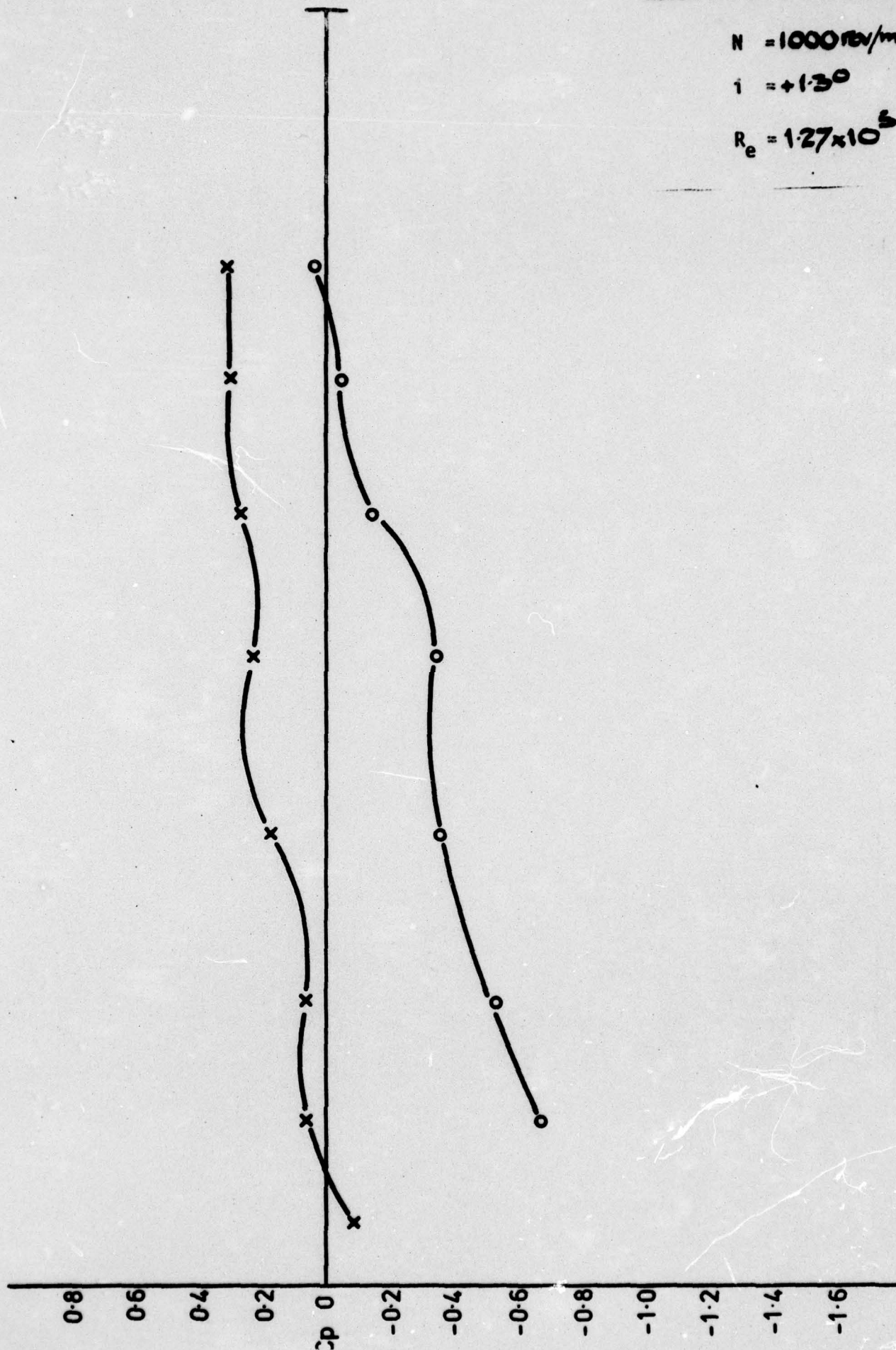


ROTOR PRESSURE DISTRIBUTION

$N = 1000 \text{ rev/min}$

$i = +1.3^\circ$

$R_e = 1.27 \times 10^5$

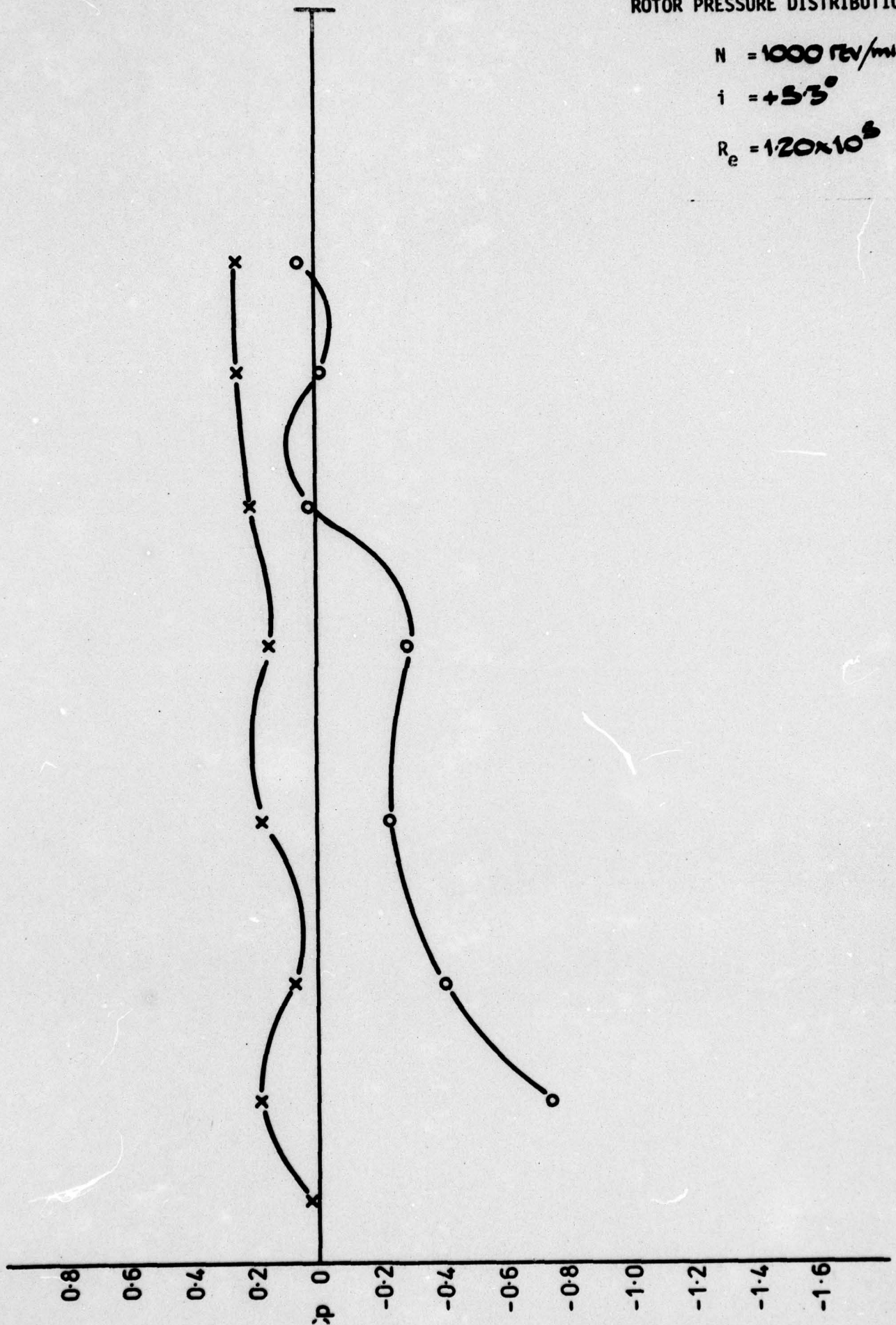


ROTOR PRESSURE DISTRIBUTION

$N = 1000 \text{ rev/min}$

$i = +5.3^\circ$

$R_e = 1.20 \times 10^6$

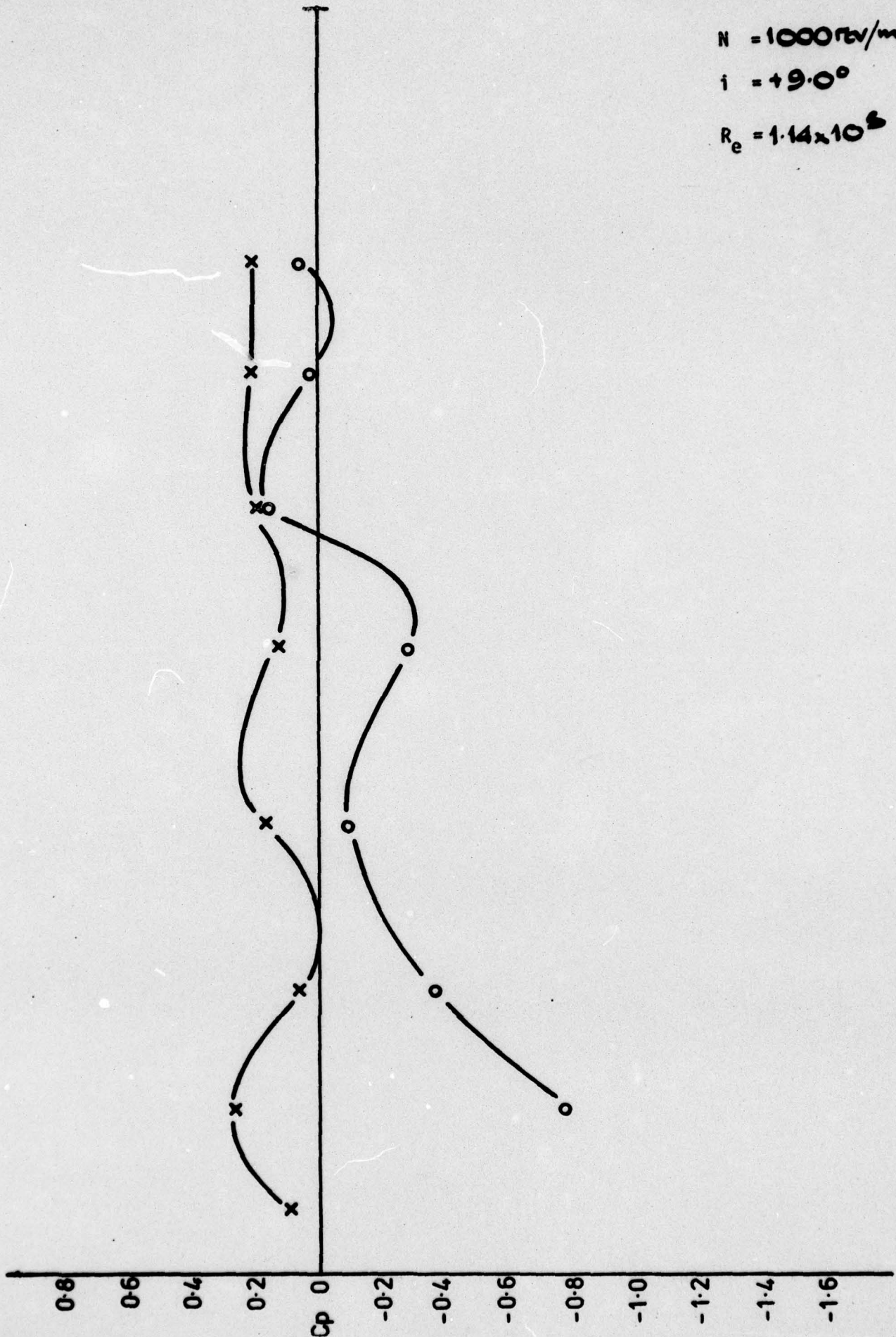


ROTOR PRESSURE DISTRIBUTION

$N = 1000 \text{ rev/min}$

$i = +9.0^\circ$

$R_e = 1.14 \times 10^6$

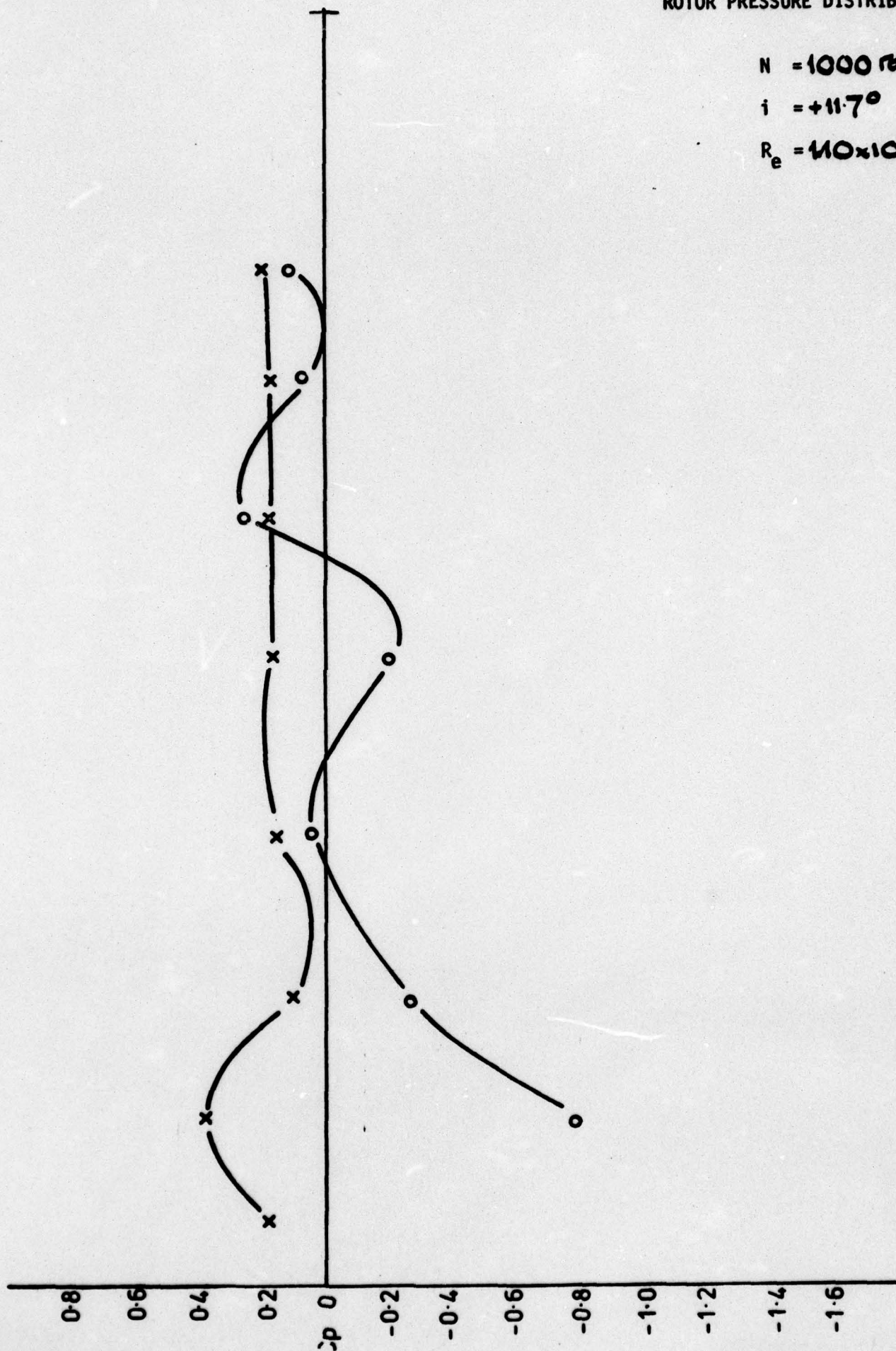


ROTOR PRESSURE DISTRIBUTION

$N = 1000 \text{ rev/min}$

$i = +11.7^\circ$

$R_e = 110 \times 10^5$

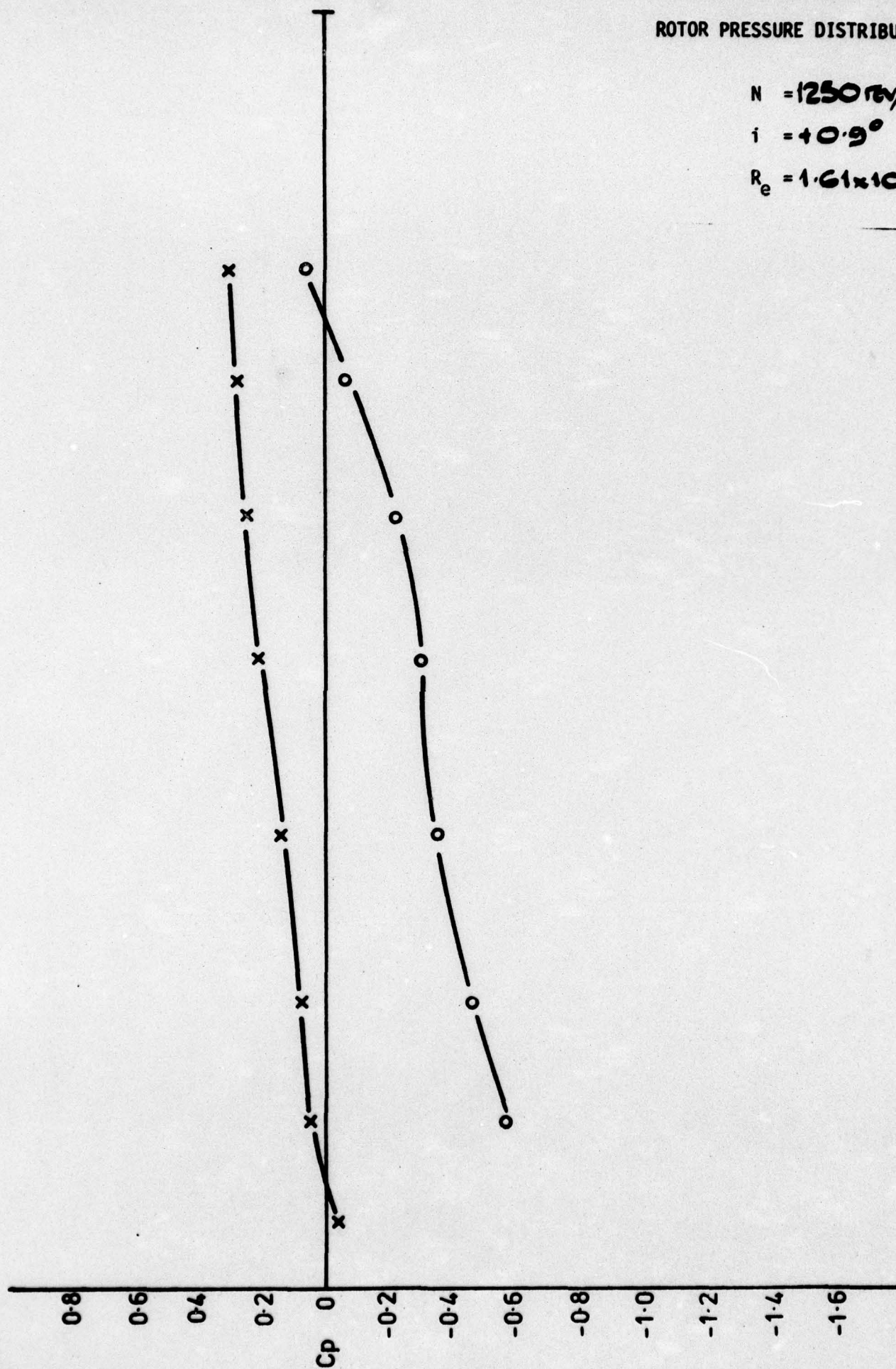


ROTOR PRESSURE DISTRIBUTION

$N = 1250 \text{ rev/min}$

$i = +0.9^\circ$

$R_e = 1.61 \times 10^5$

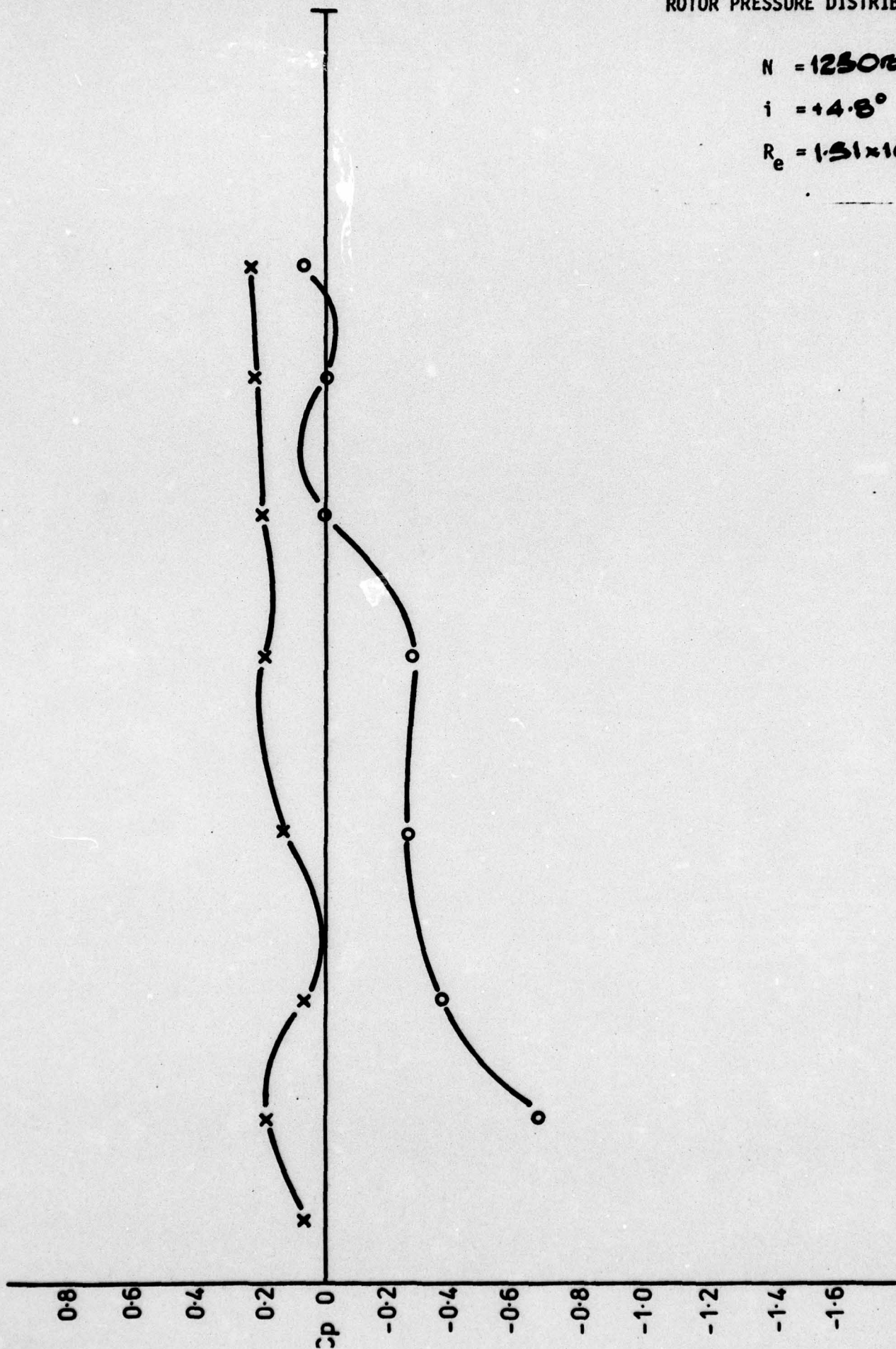


ROTOR PRESSURE DISTRIBUTION

$N = 1250 \text{ rev/min}$

$i = +4.8^\circ$

$R_e = 1.51 \times 10^5$

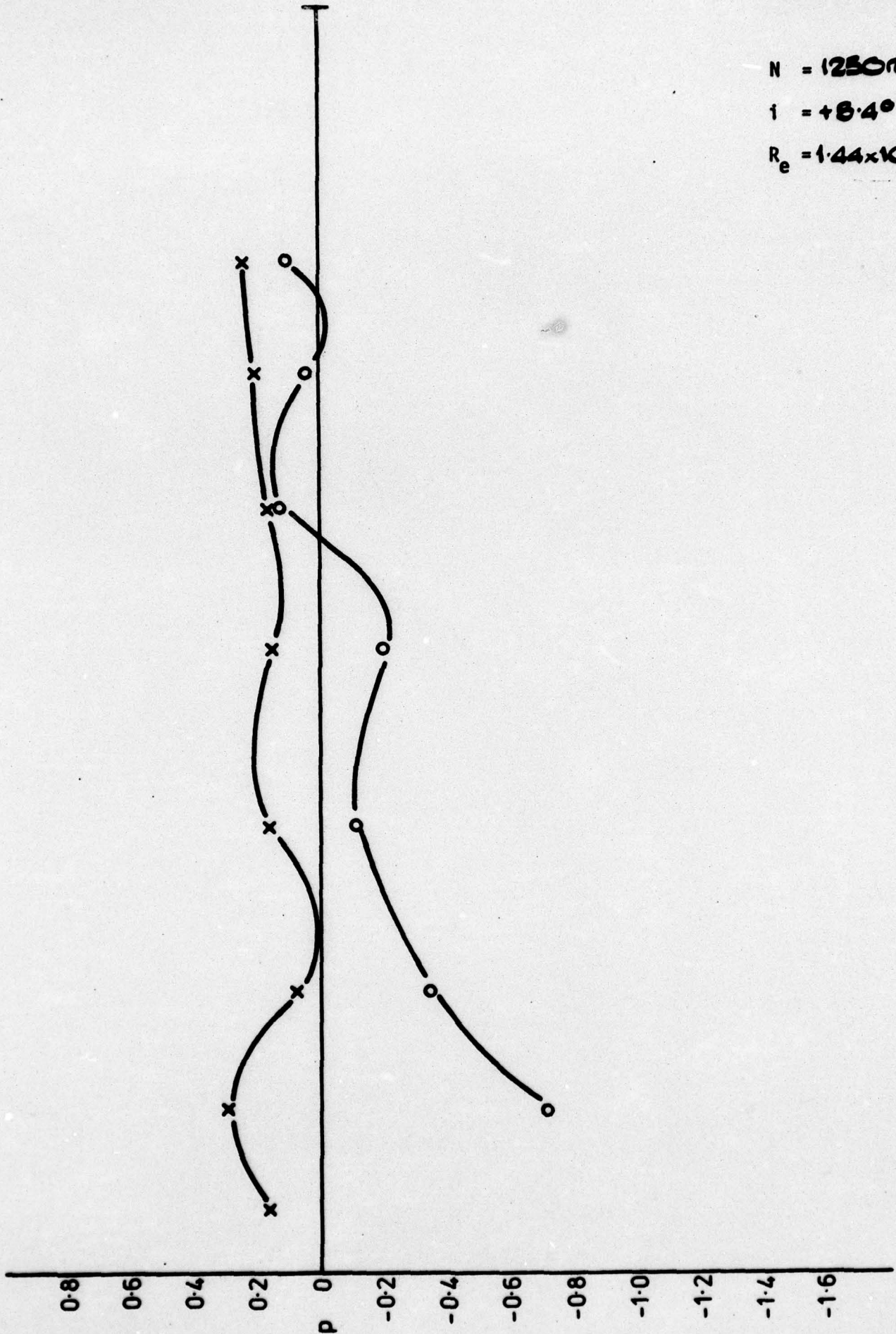


ROTOR PRESSURE DISTRIBUTION

$N = 1250 \text{ rev/min}$

$i = +8.4^\circ$

$R_e = 1.44 \times 10^5$

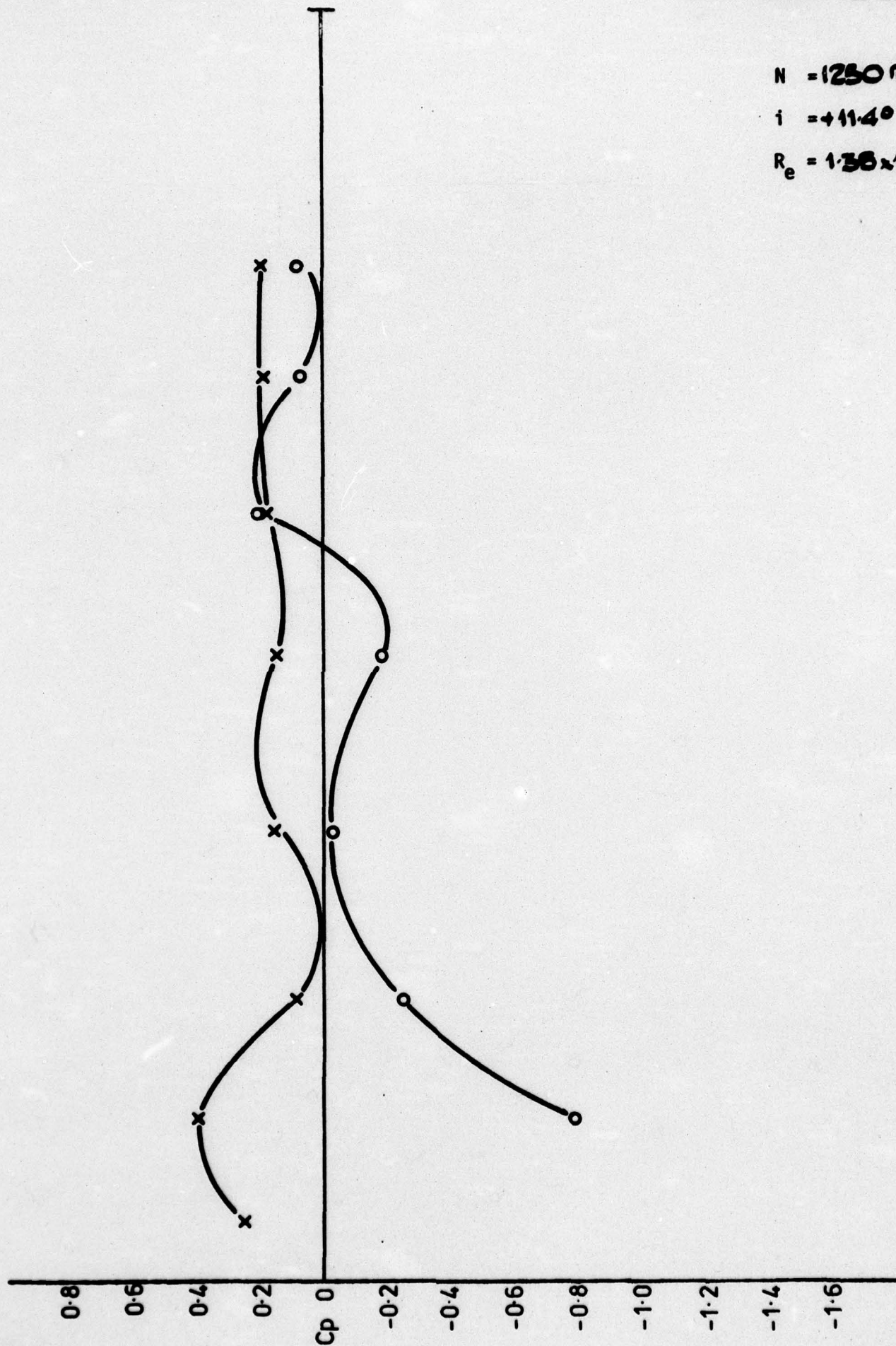


ROTOR PRESSURE DISTRIBUTION

$N = 1250 \text{ rev/min}$

$i = +11.4^\circ$

$R_e = 1.35 \times 10^5$

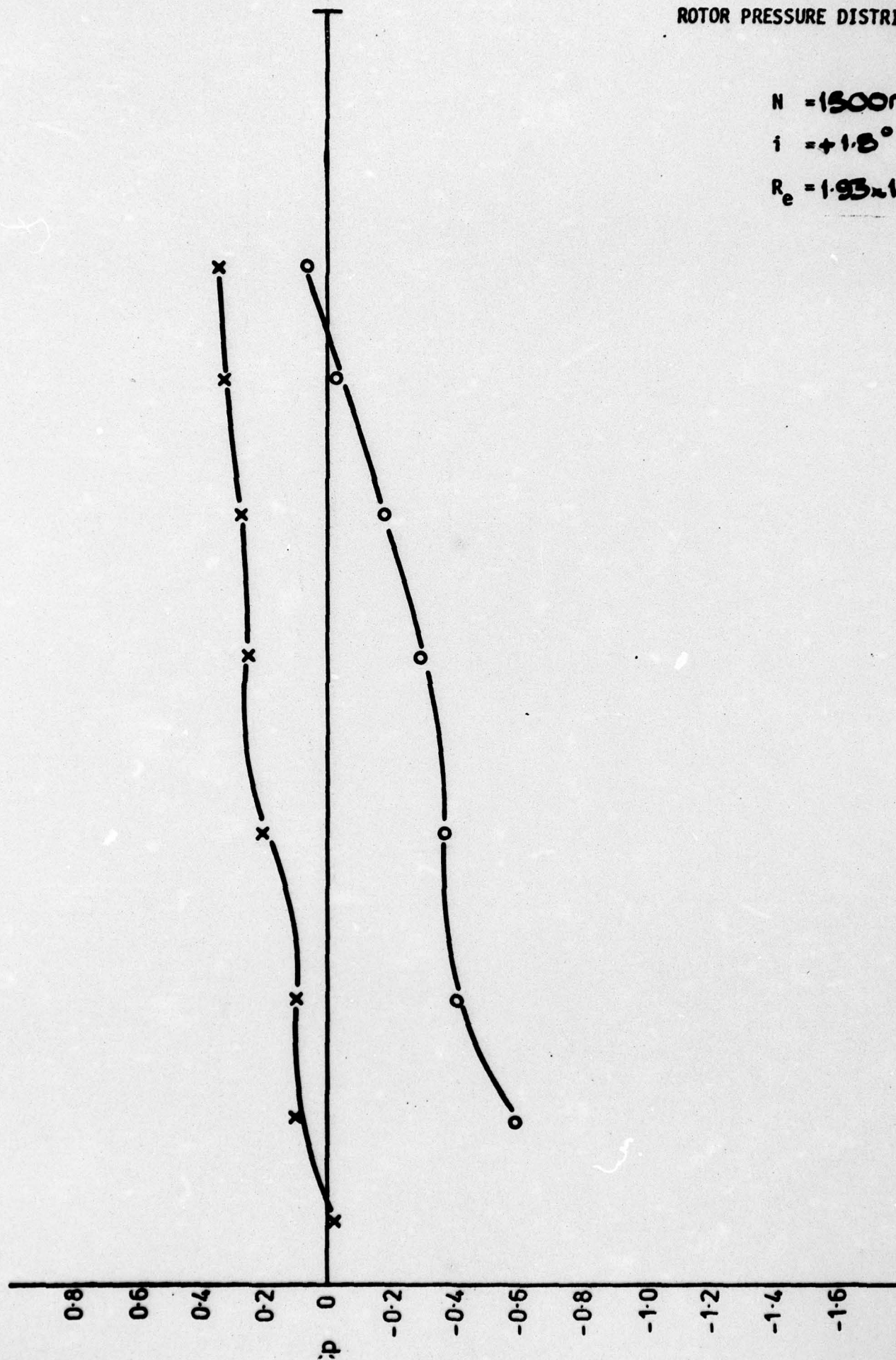


ROTOR PRESSURE DISTRIBUTION

$N = 1500 \text{ rev/min}$

$i = +1.8^\circ$

$R_e = 1.93 \times 10^6$

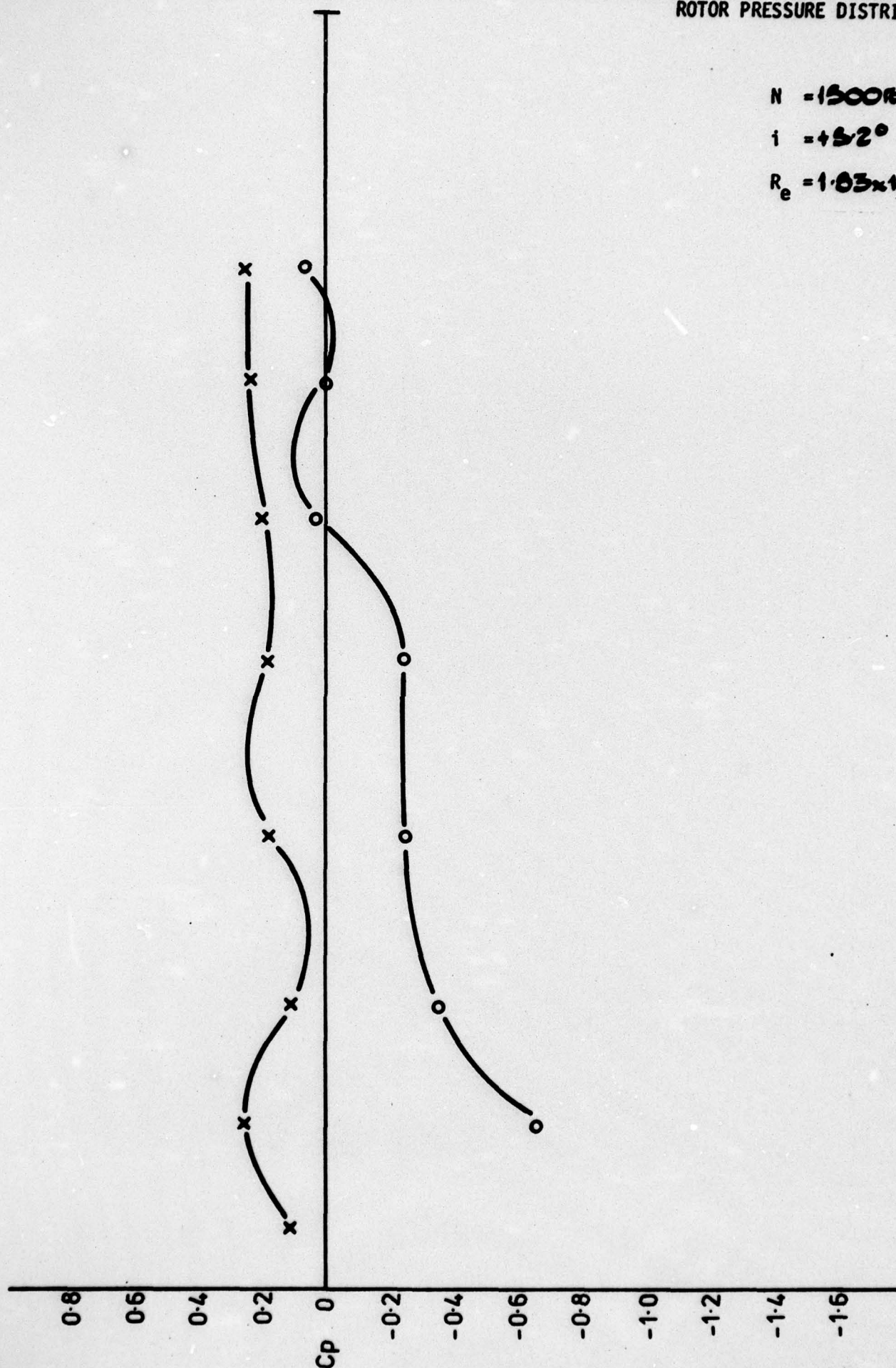


ROTOR PRESSURE DISTRIBUTION

$N = 1500 \text{ rev/min}$

$i = +5.2^\circ$

$R_e = 1.83 \times 10^5$

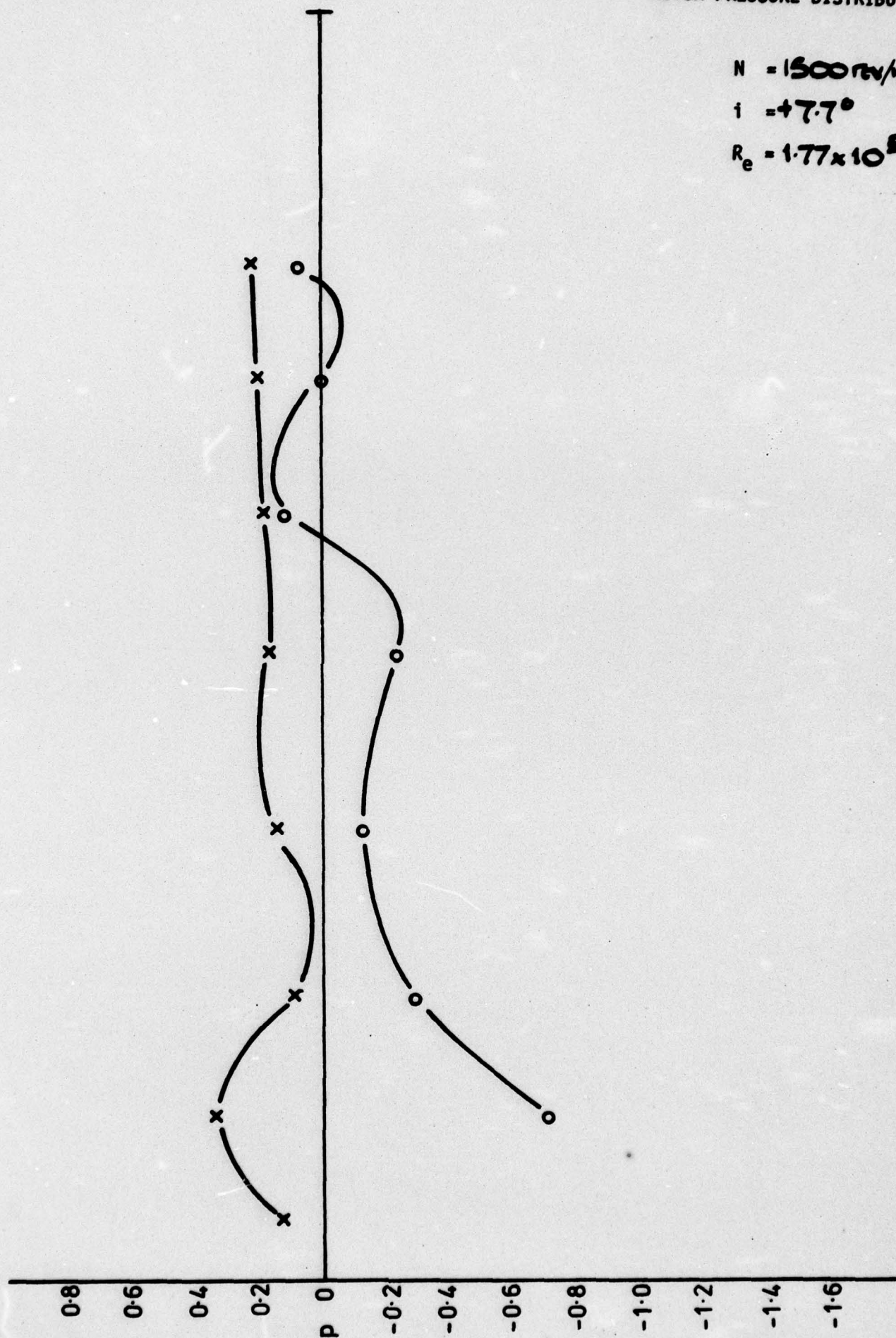


ROTOR PRESSURE DISTRIBUTION

$N = 1500 \text{ rev/min}$

$i = +7.7^\circ$

$R_e = 1.77 \times 10^6$

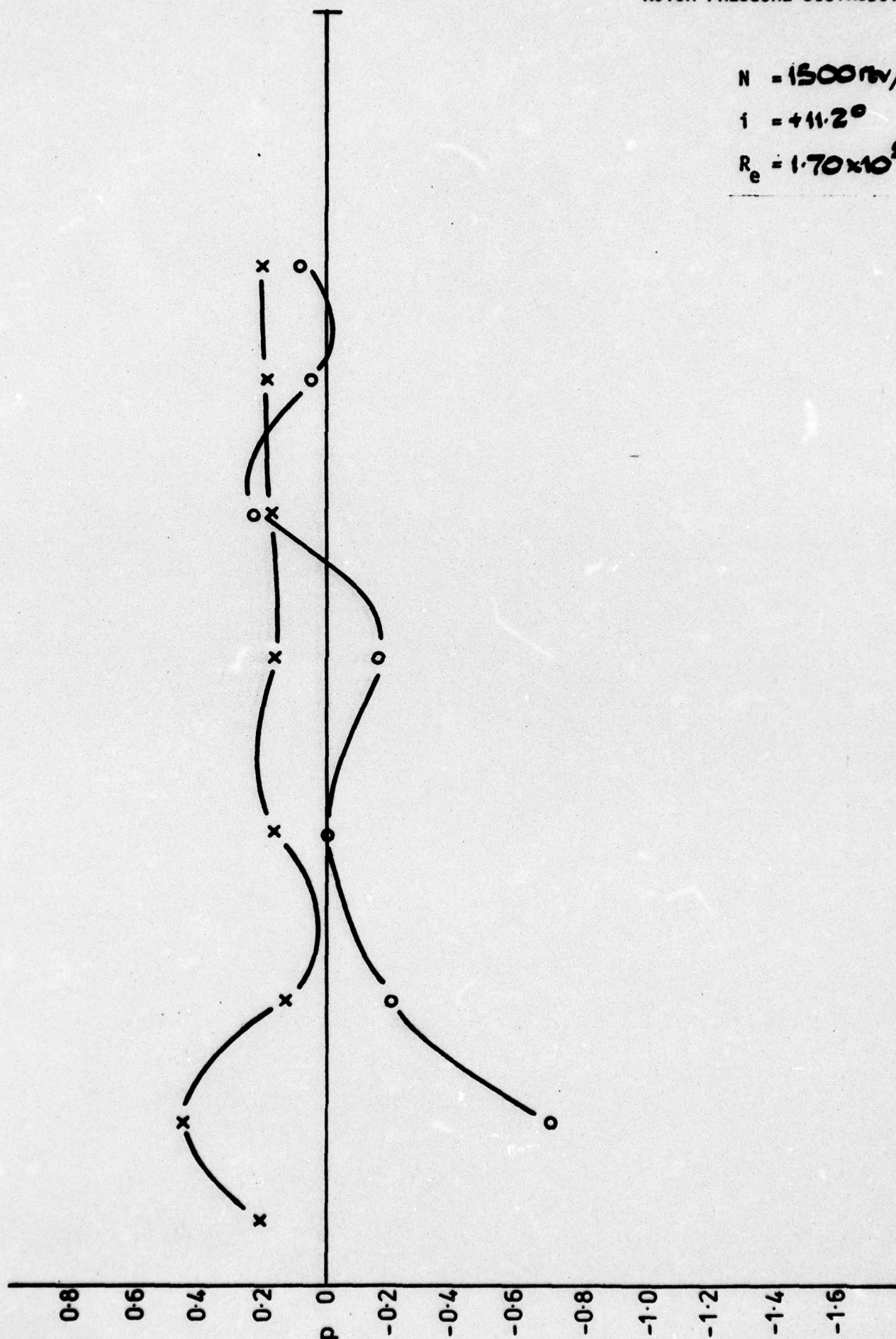


ROTOR PRESSURE DISTRIBUTION

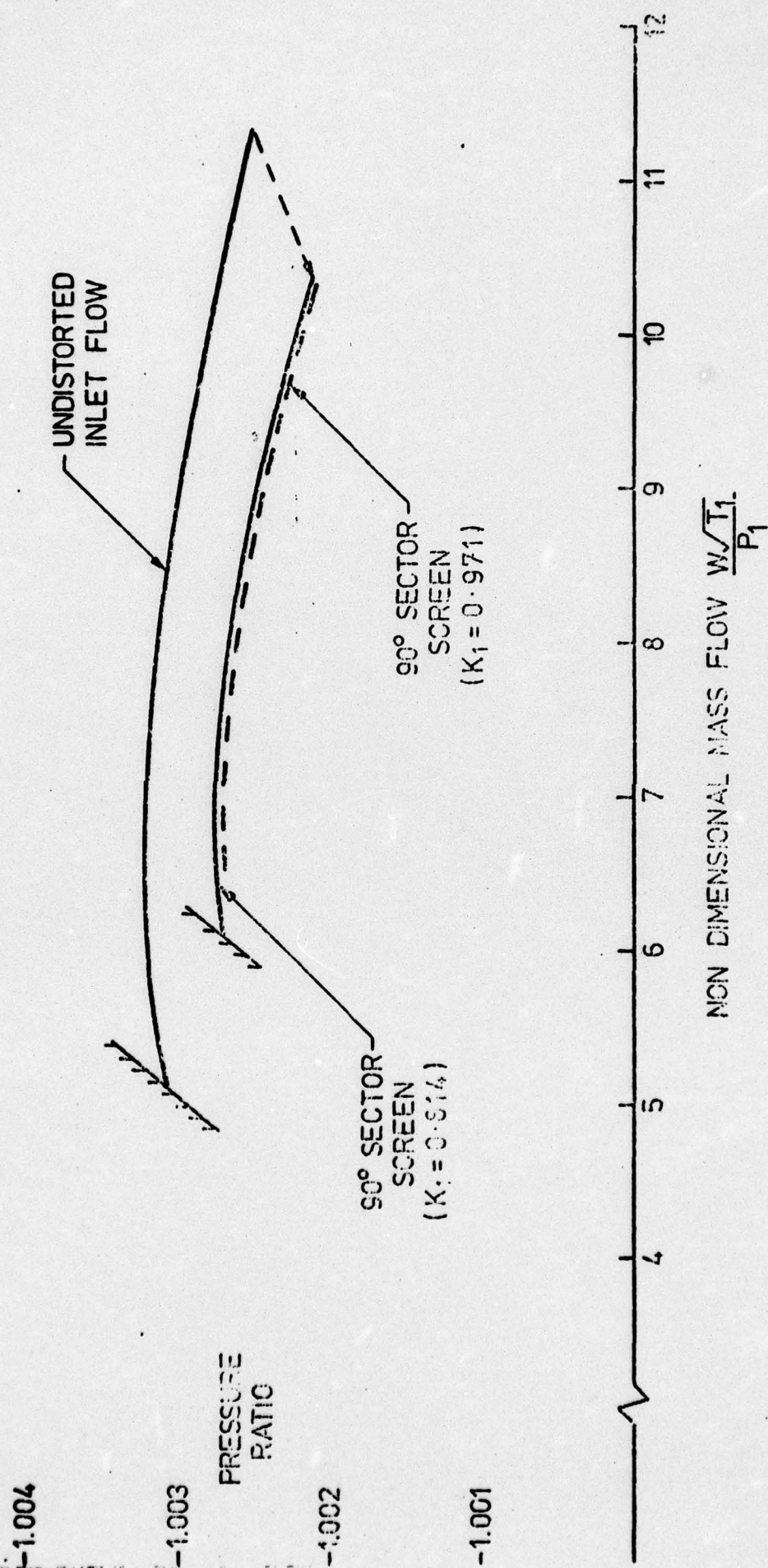
$N = 1500 \text{ rev/min}$

$i = +11.2^\circ$

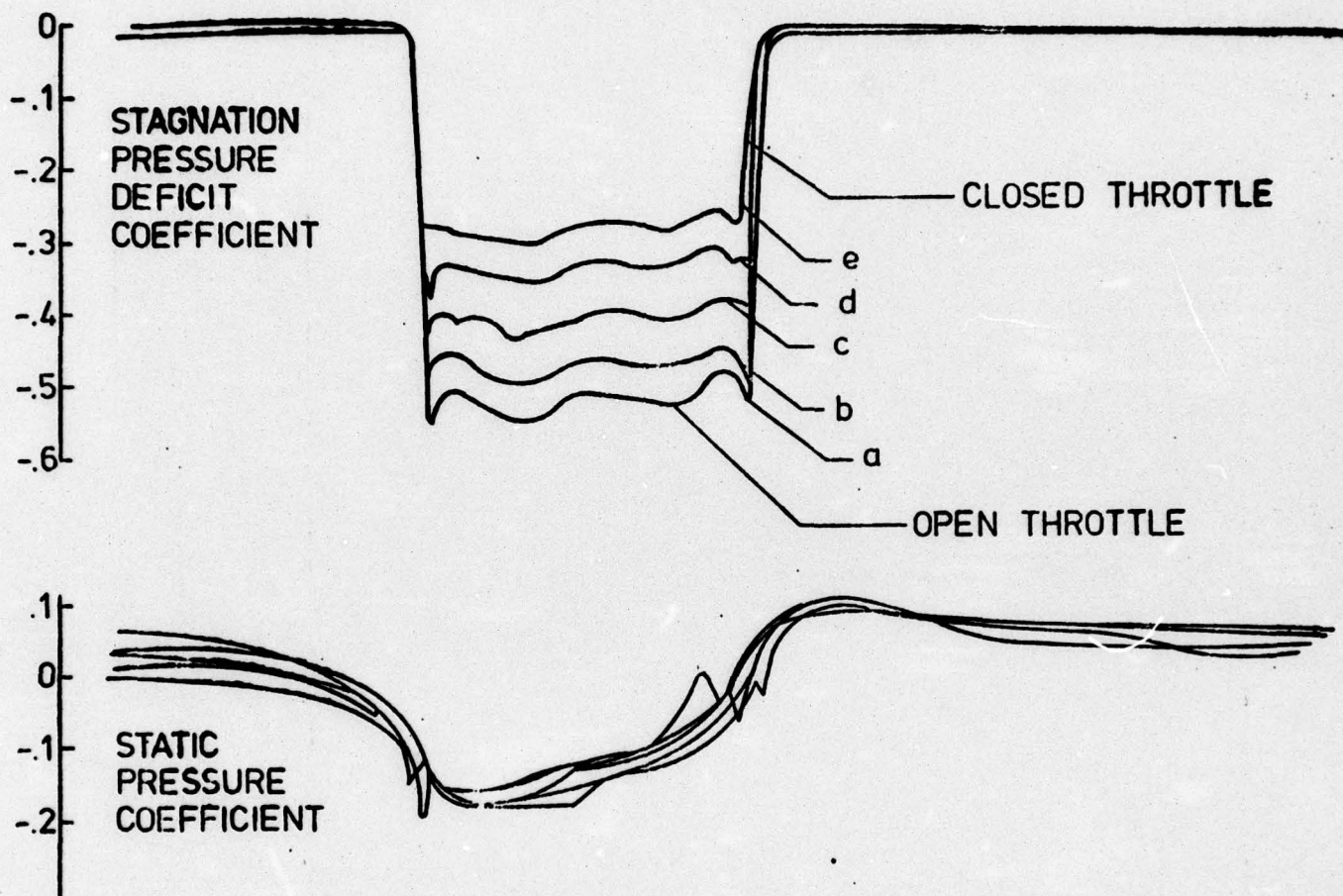
$R_e = 1.70 \times 10^8$



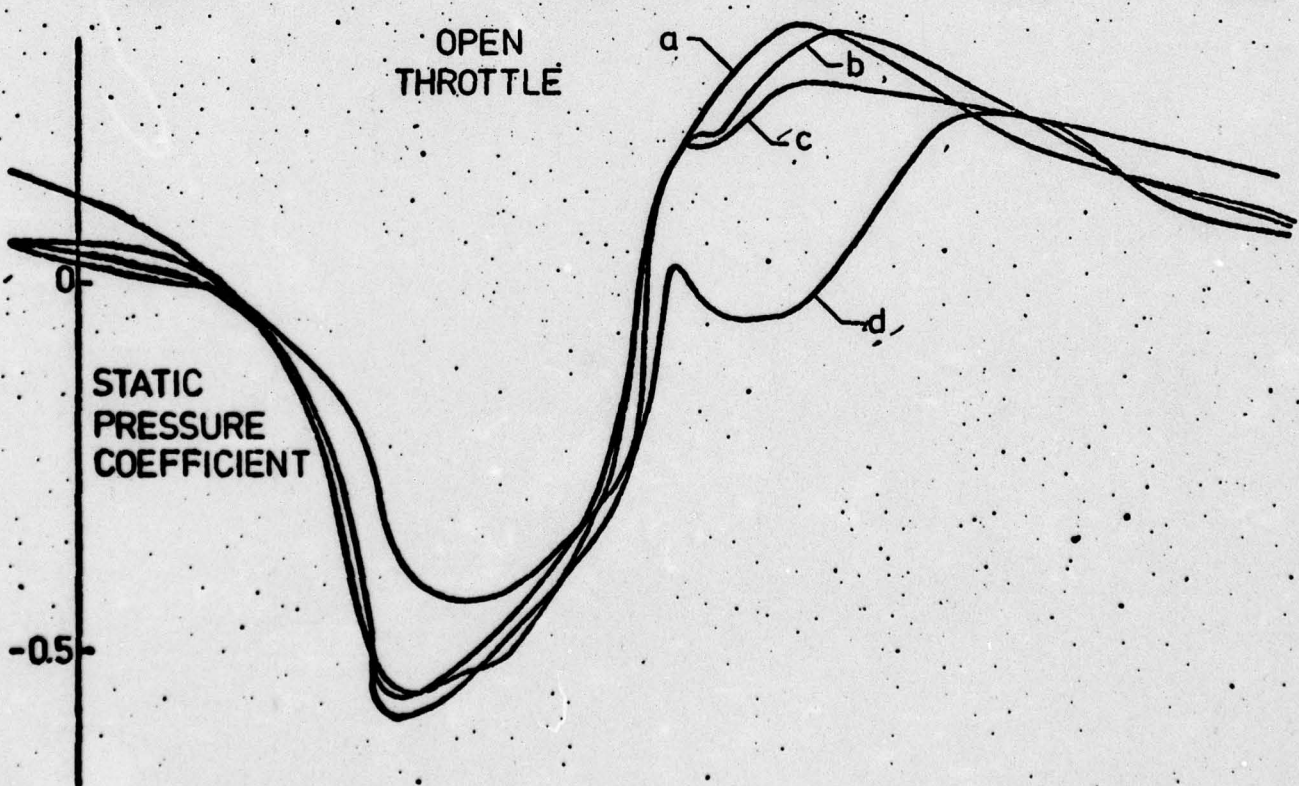
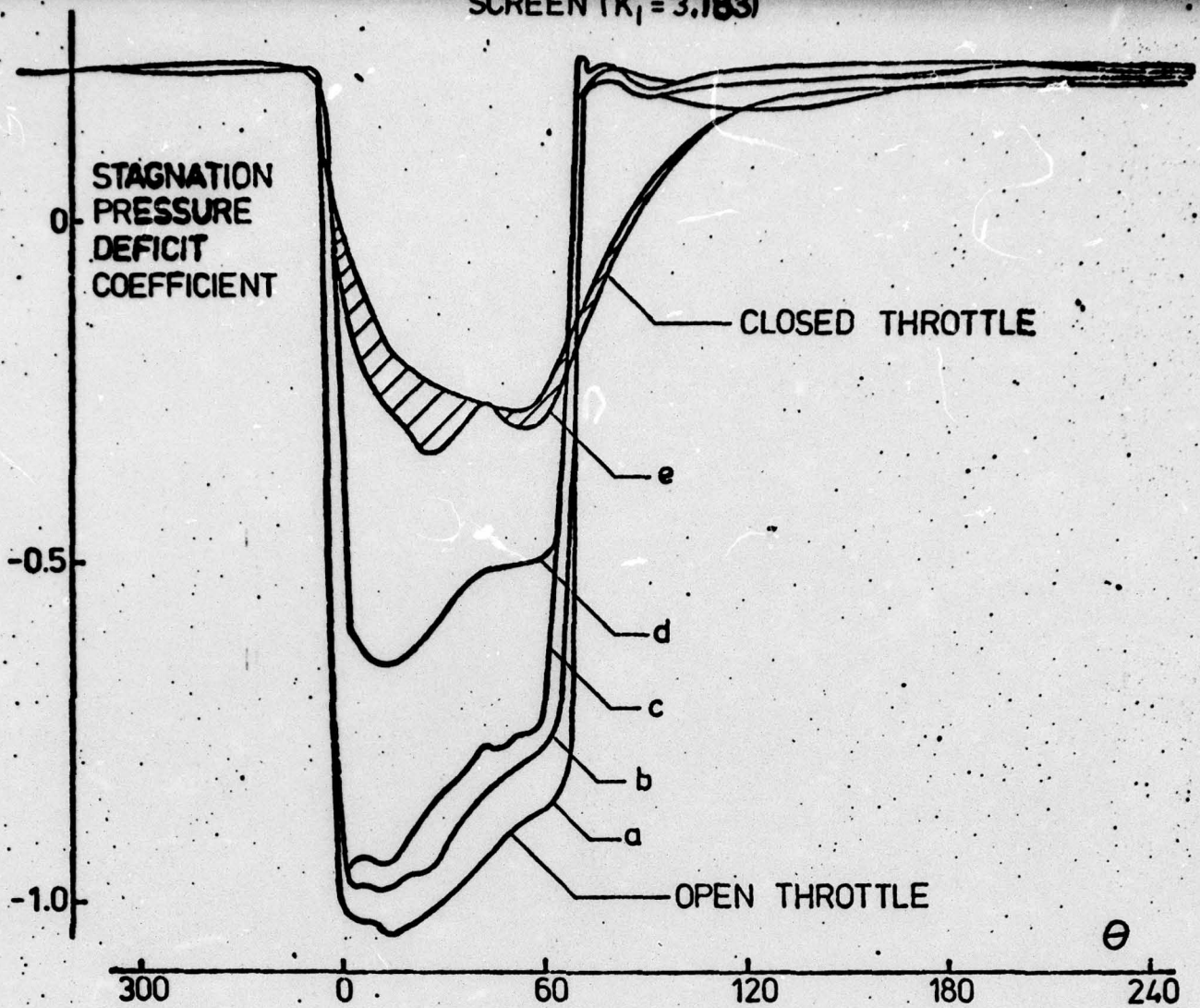
EFFECT UPON COMPRESSOR CHARACTERISTIC (N=1250 rev/min) OF DISTORTIONS.



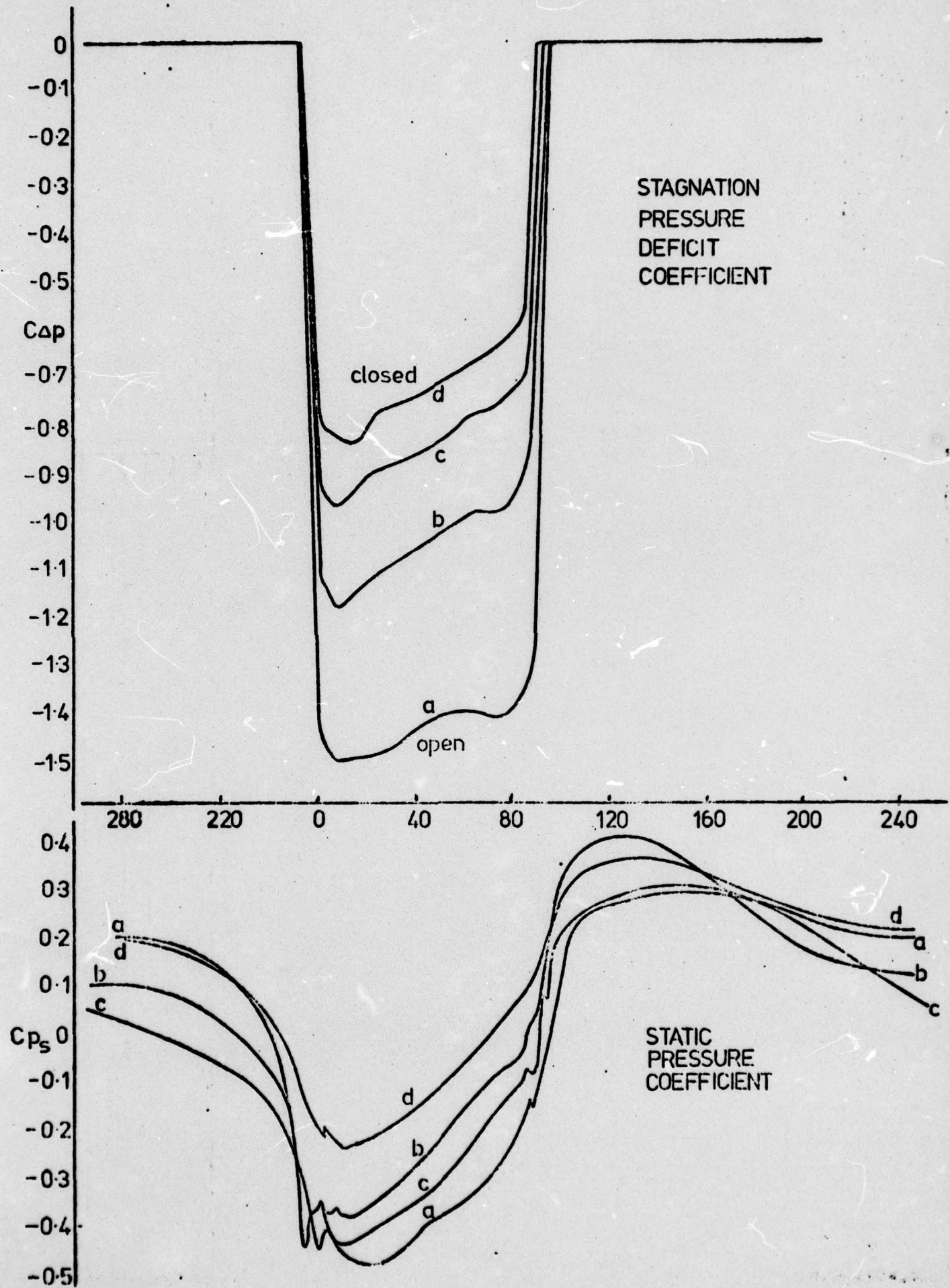
EFFECT OF COMPRESSOR OPERATING POINT ON DISTORTION.
SCREEN ($K_1 = 0.971$)



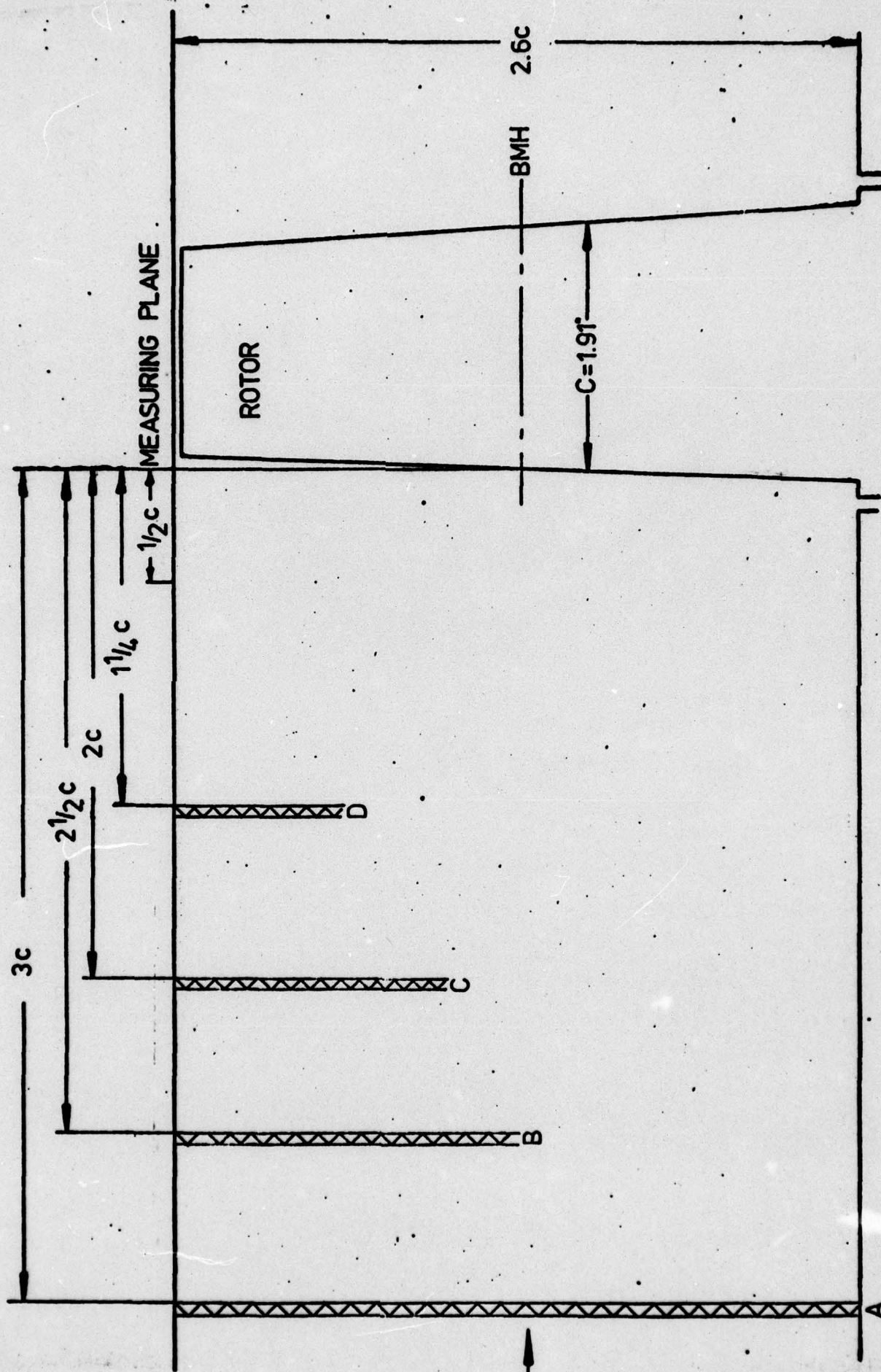
SCREEN ($K_1 = 3.183$)

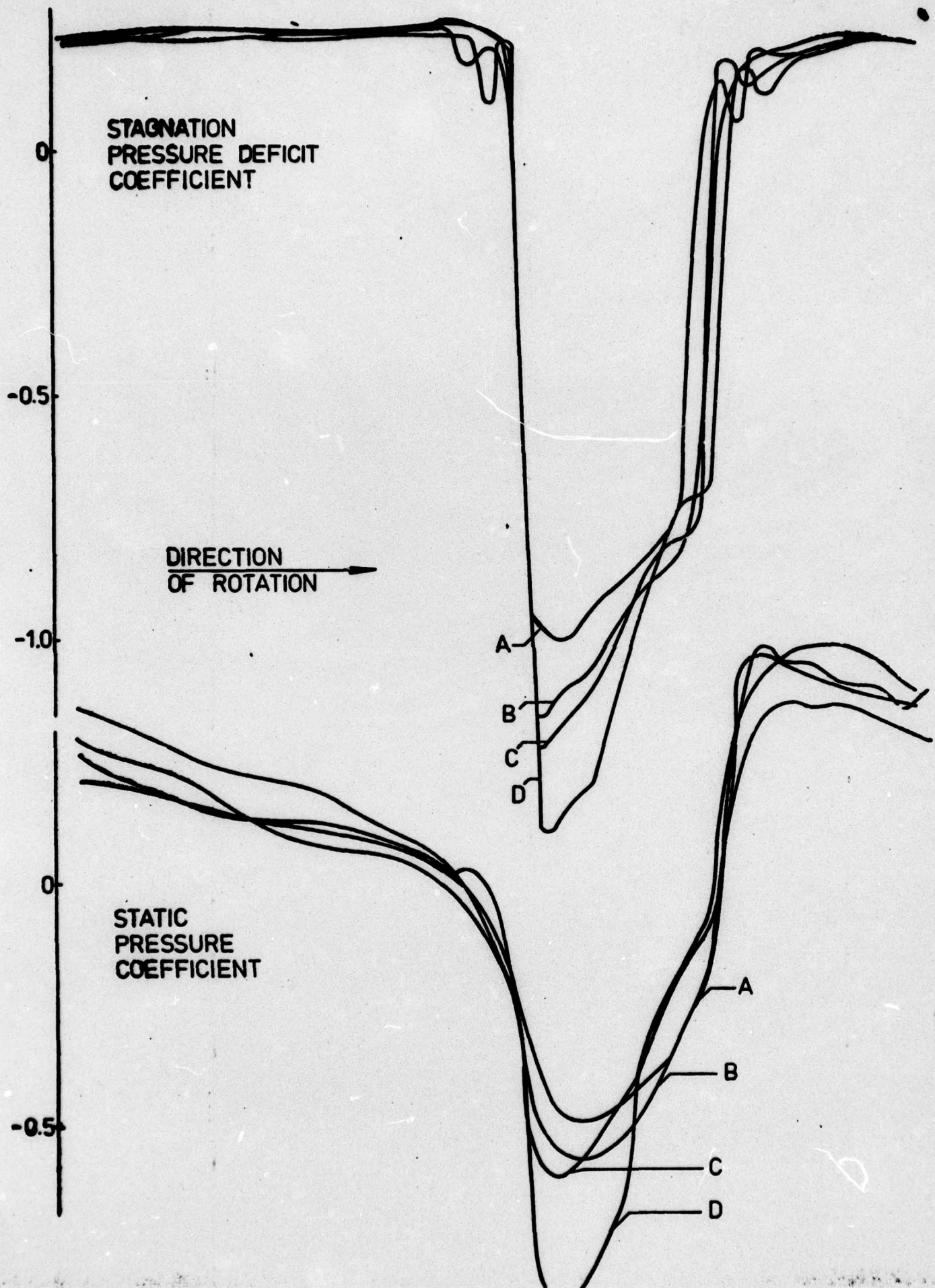


SCREEN (K=3.183)



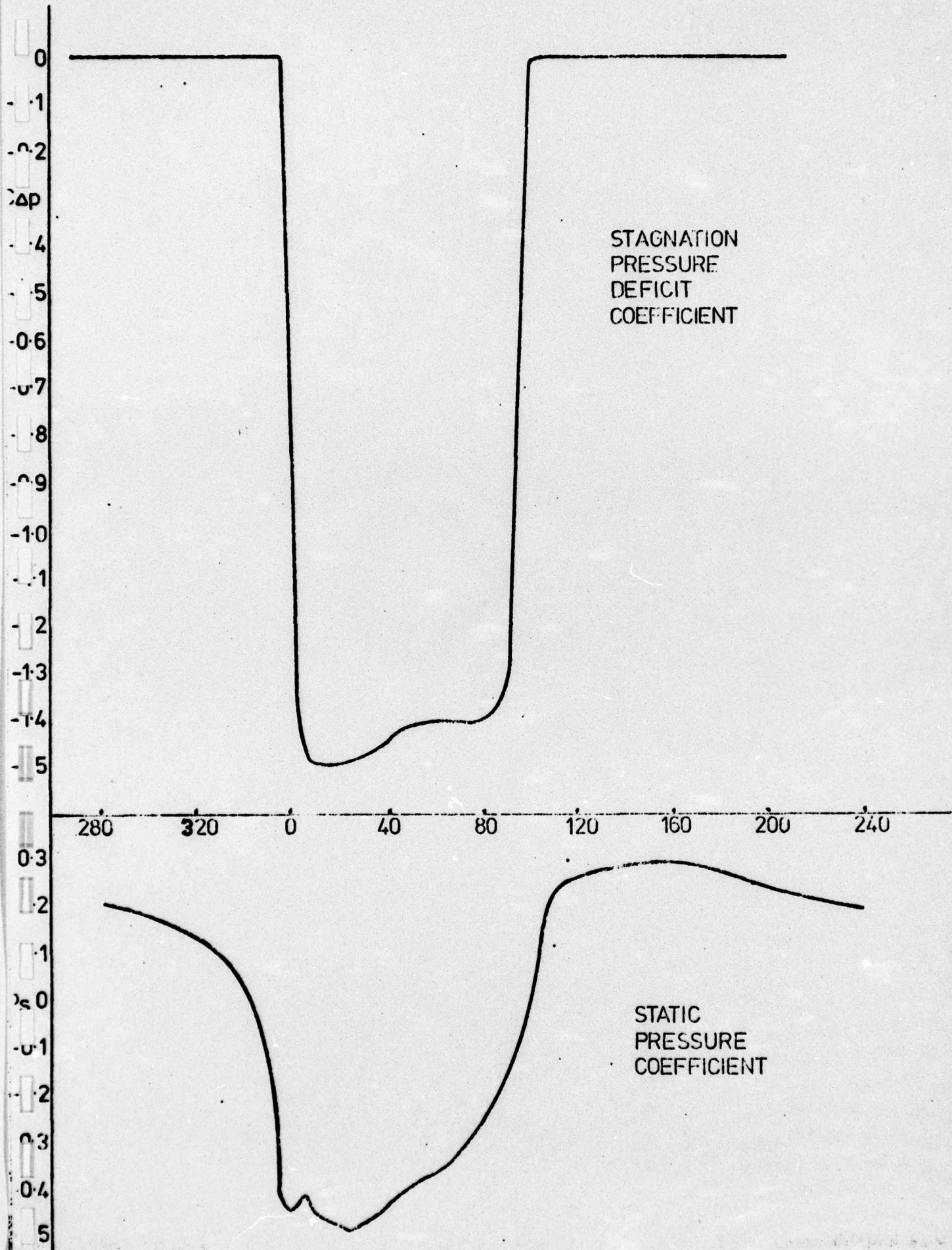
LOCATIONS OF DISTORTION SCREENS WITHIN THE COMPRESSOR INTAKE



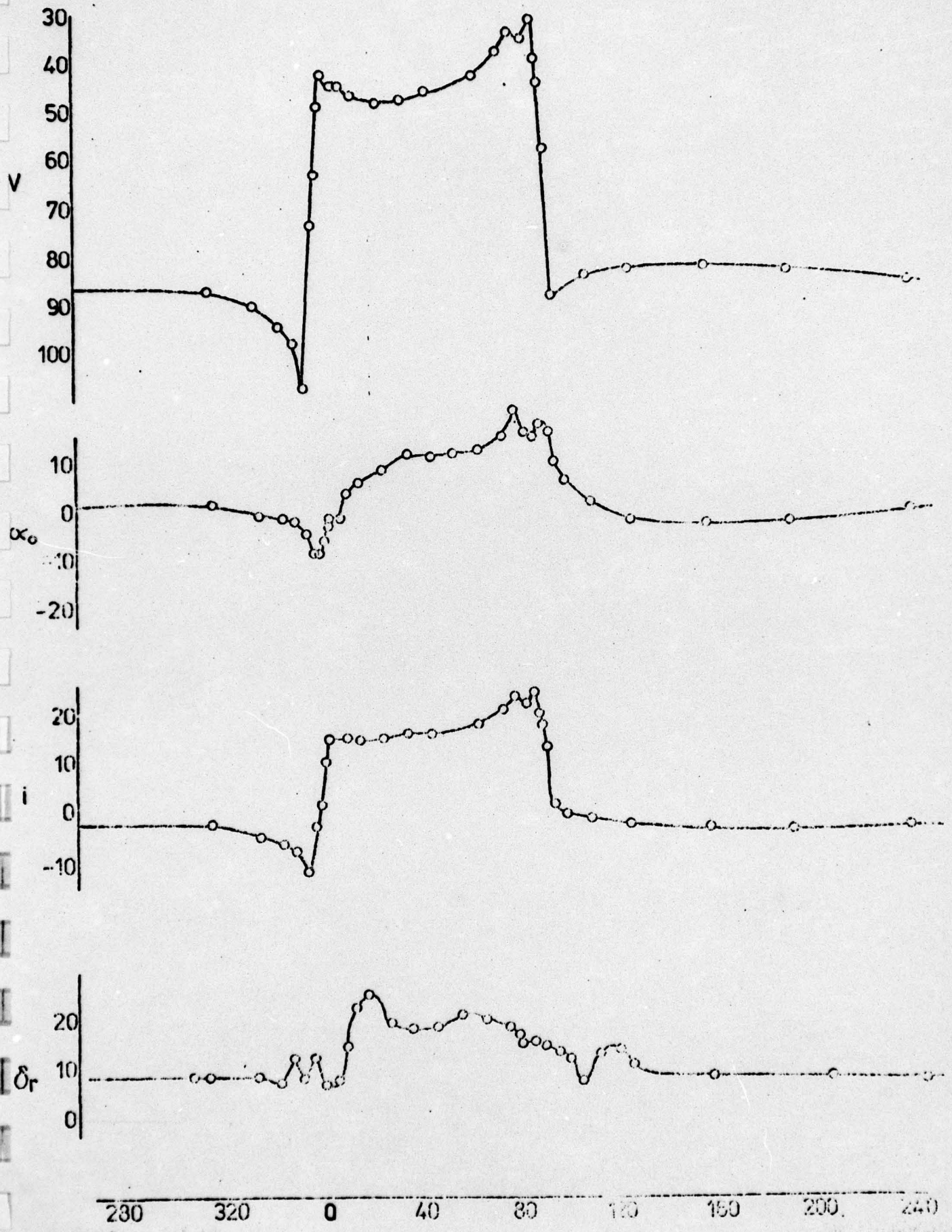


EFFECT OF COMPRESSOR OPERATING POINT ON DISTORTION.
SCREEN (K = 3.183)

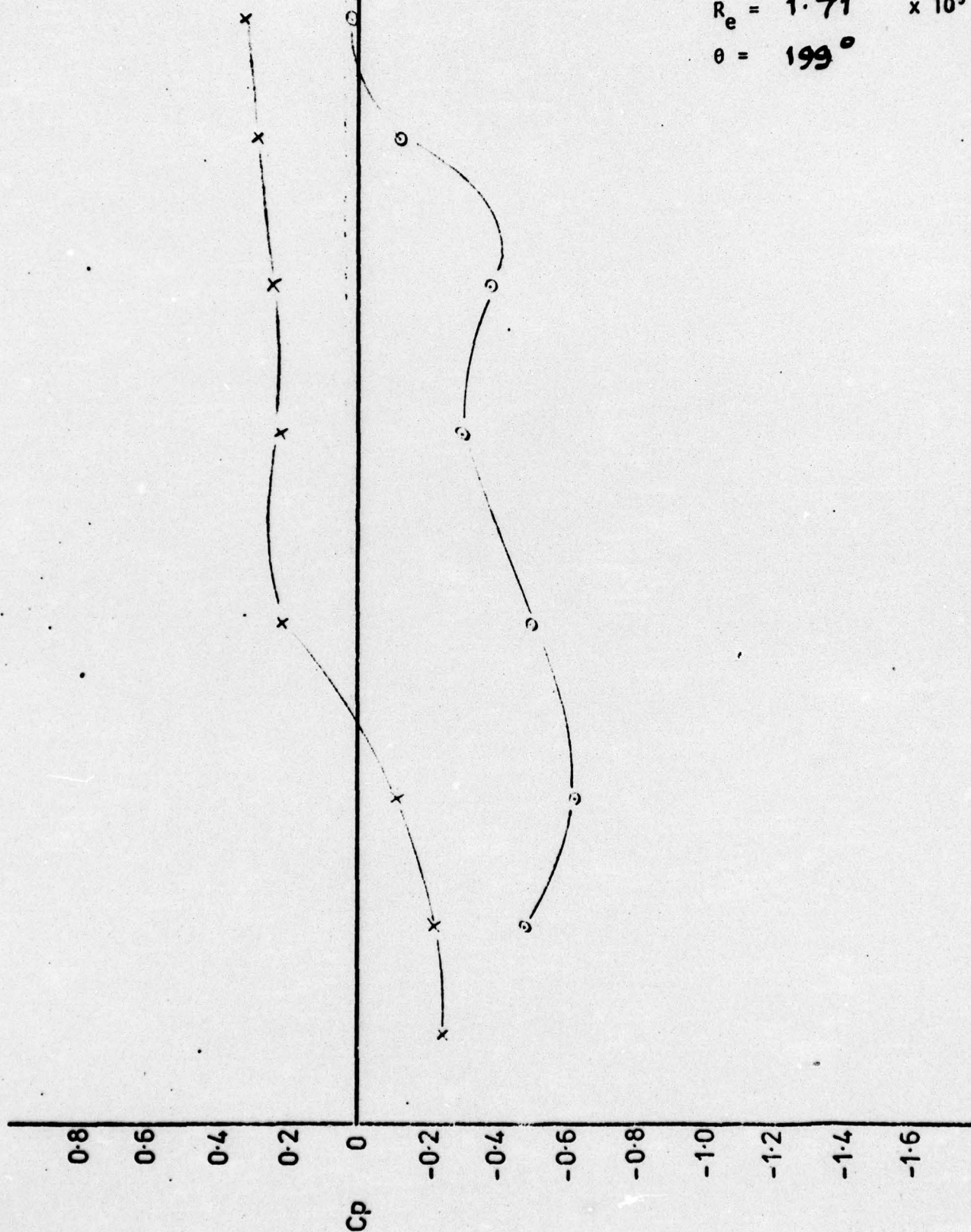
FIG. 278.



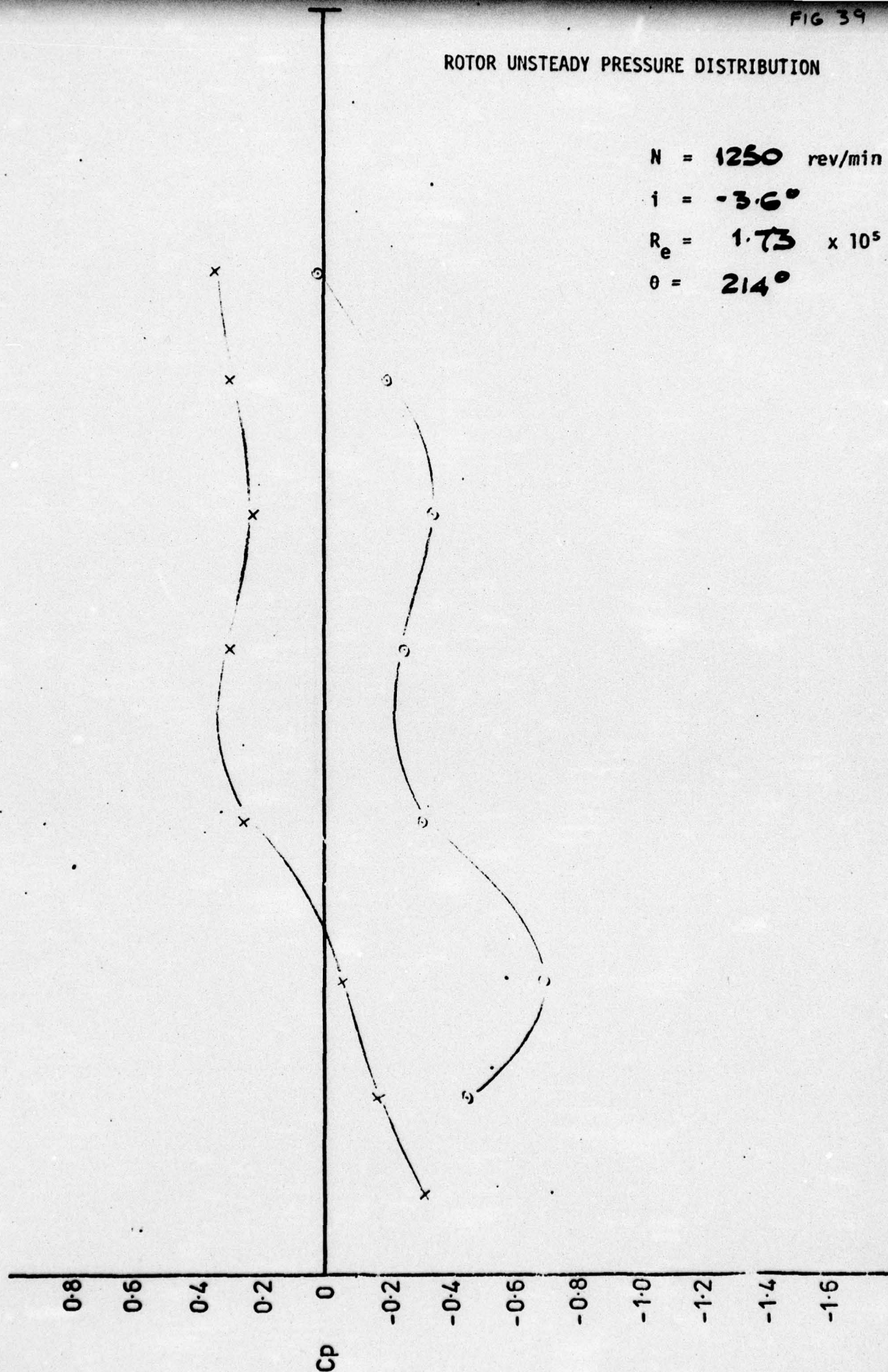
OPEN THROTTLE (N = 1250 REV/MIN) . DISTORTION LEVELS



ROTOR UNSTEADY PRESSURE DISTRIBUTION

 $N = 1250$ rev/min $i = 39^\circ$ $R_e = 1.71 \times 10^5$ $\theta = 199^\circ$ 

ROTOR UNSTEADY PRESSURE DISTRIBUTION

 $N = 1250$ rev/min $i = -3.6^\circ$ $R_e = 1.73 \times 10^5$ $\theta = 214^\circ$ 

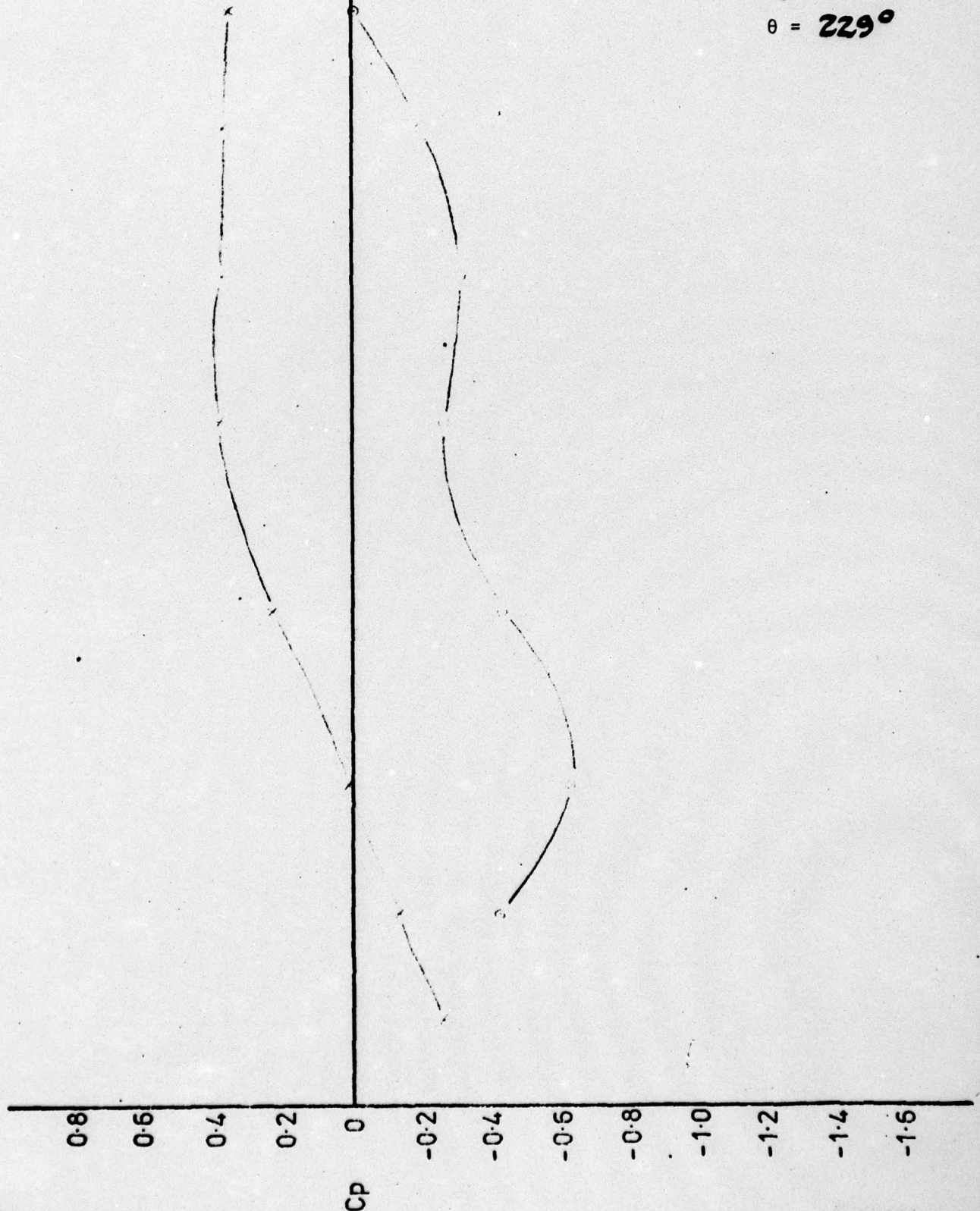
ROTOR UNSTEADY PRESSURE DISTRIBUTION

$N = 1250$ rev/min

$i = -3.5^\circ$

$R_e = 1.74 \times 10^5$

$\theta = 229^\circ$



ROTOR UNSTEADY PRESSURE DISTRIBUTION

$N = 1250$ rev/min

$i = -3.4^\circ$

$R_e = 1.77 \times 10^5$

$\theta = 244^\circ$



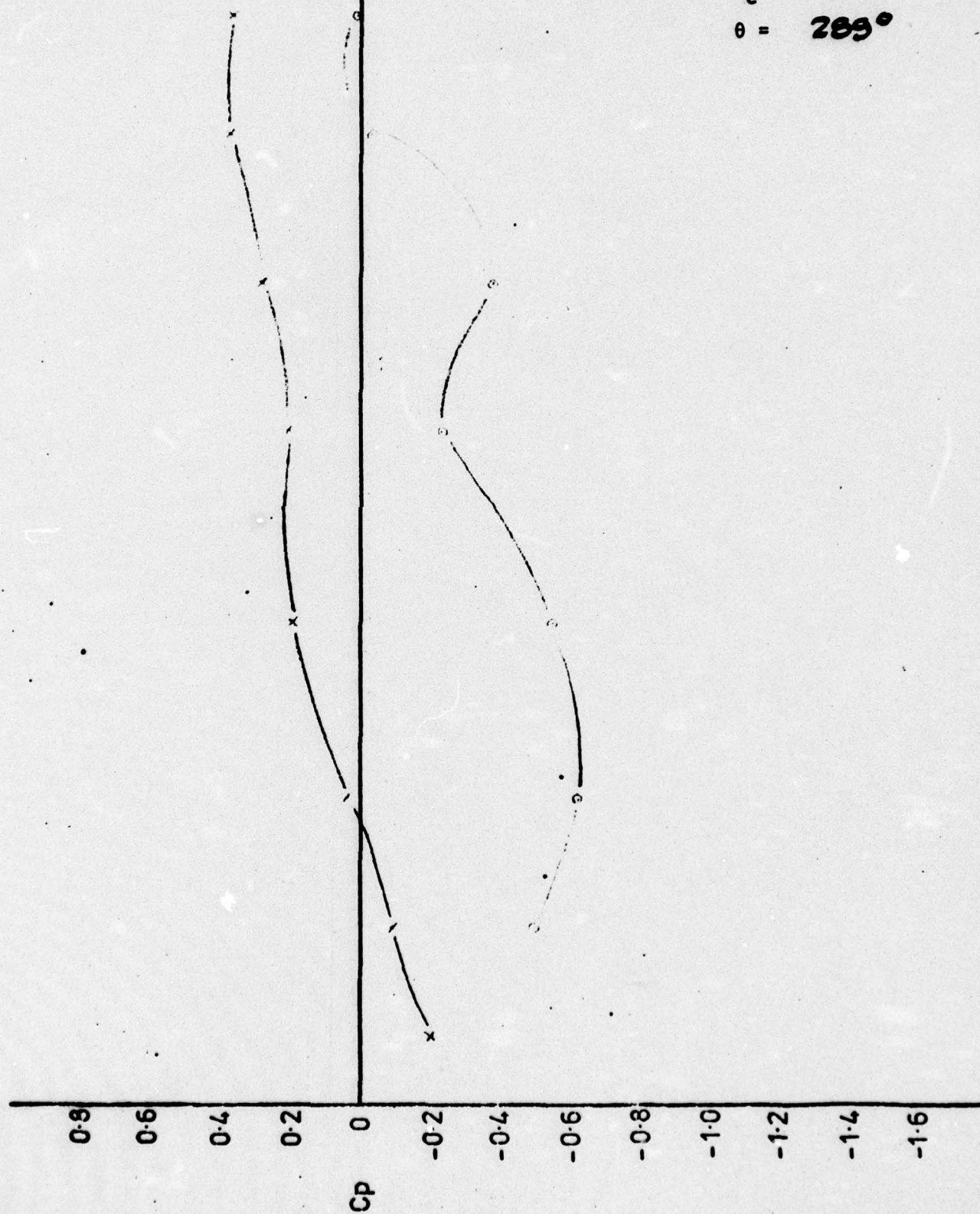
ROTOR UNSTEADY PRESSURE DISTRIBUTION

$N = 1250$ rev/min

$\dot{t} = -3.0^\circ$

$R_e = 1.75 \times 10^5$

$\theta = 289^\circ$



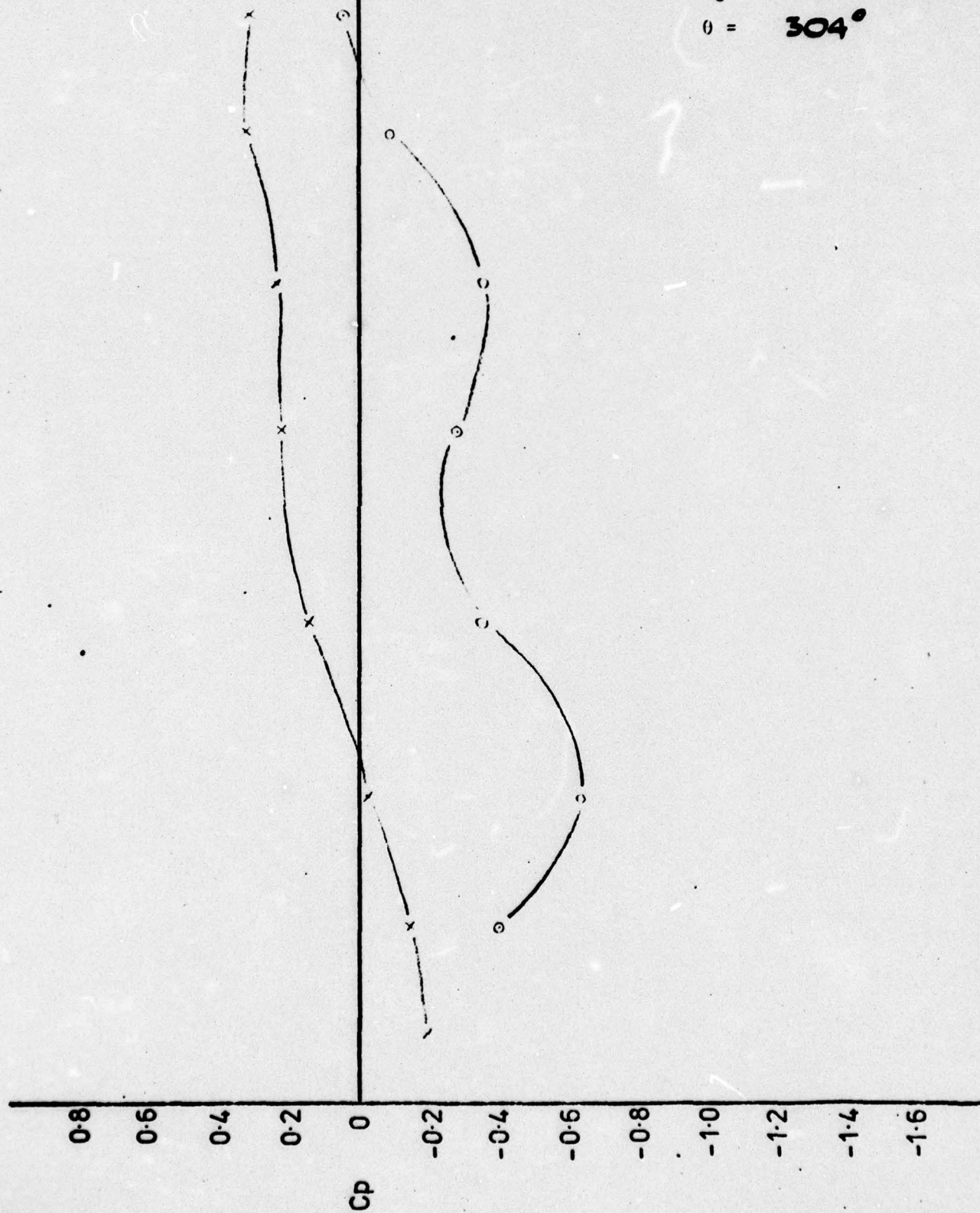
ROTOR UNSTEADY PRESSURE DISTRIBUTION

$N = 1250$ rev/min

$i = -3.0^\circ$

$R_e = 1.81 \times 10^5$

$\theta = 304^\circ$



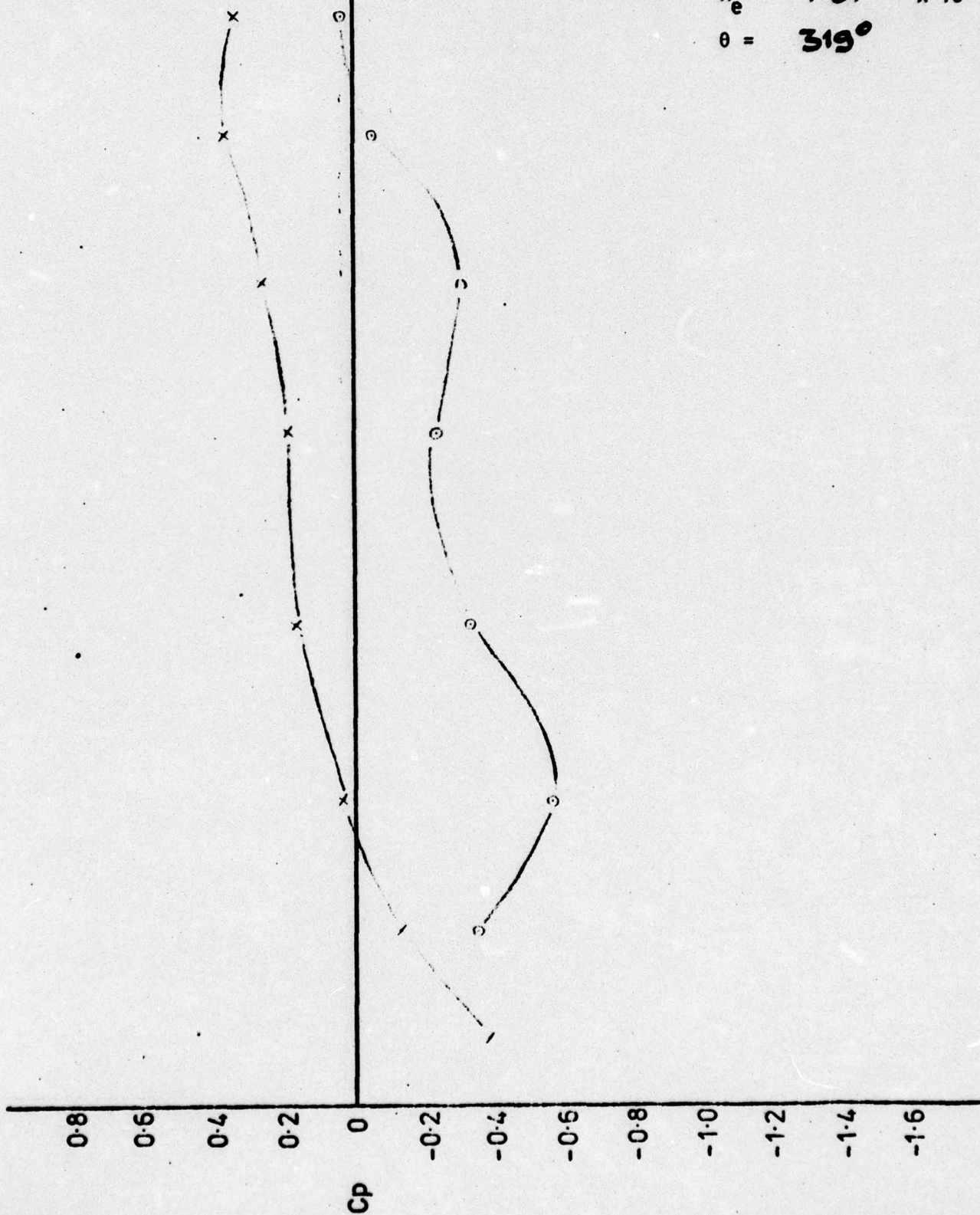
ROTOR UNSTEADY PRESSURE DISTRIBUTION

$N = 1250$ rev/min

$i = -32^\circ$

$R_e = 1.81 \times 10^5$

$\theta = 319^\circ$



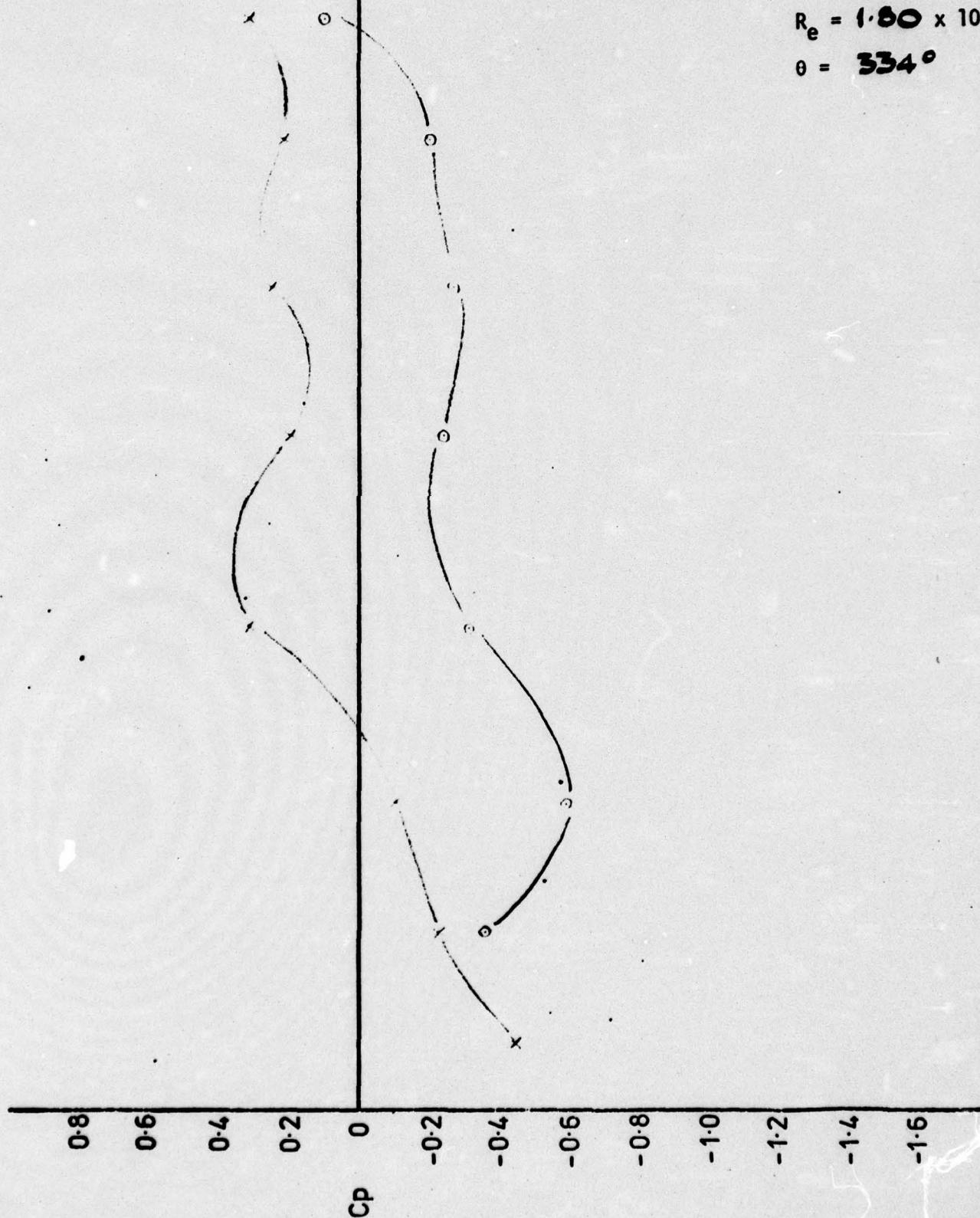
ROTOR UNSTEADY PRESSURE DISTRIBUTION

$N = 1250$ rev/min

$i = -55^\circ$

$Re = 1.80 \times 10^5$

$\theta = 334^\circ$



ROTOR UNSTEADY PRESSURE DISTRIBUTION

$N = 1250$ rev/min

$i = -8.4^\circ$

$R_e = 1.06 \times 10^5$

$\theta = 349^\circ$



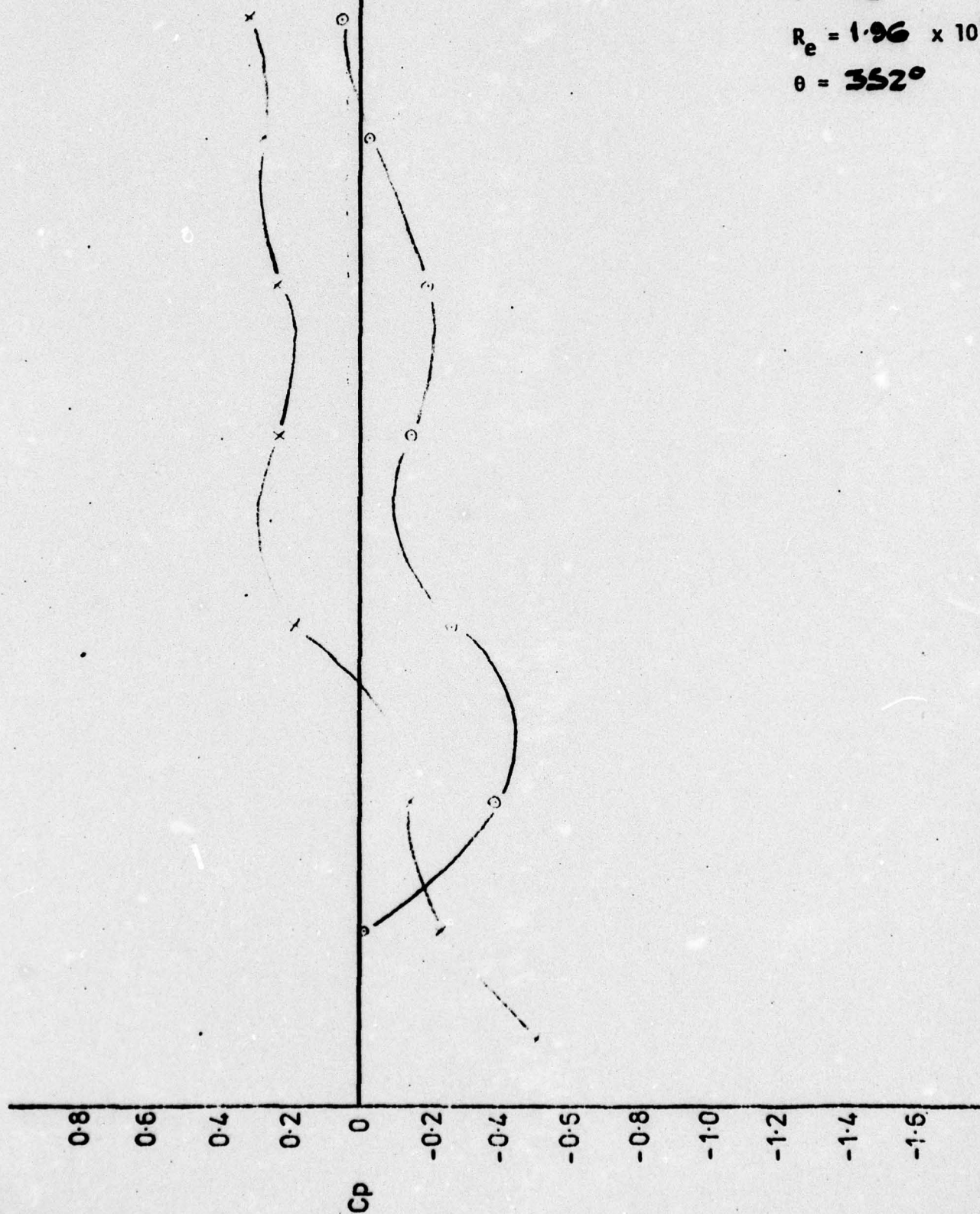
ROTOR UNSTEADY PRESSURE DISTRIBUTION

$N = 1250$ rev/min

$i = -10^\circ$

$R_e = 1.96 \times 10^5$

$\theta = 352^\circ$



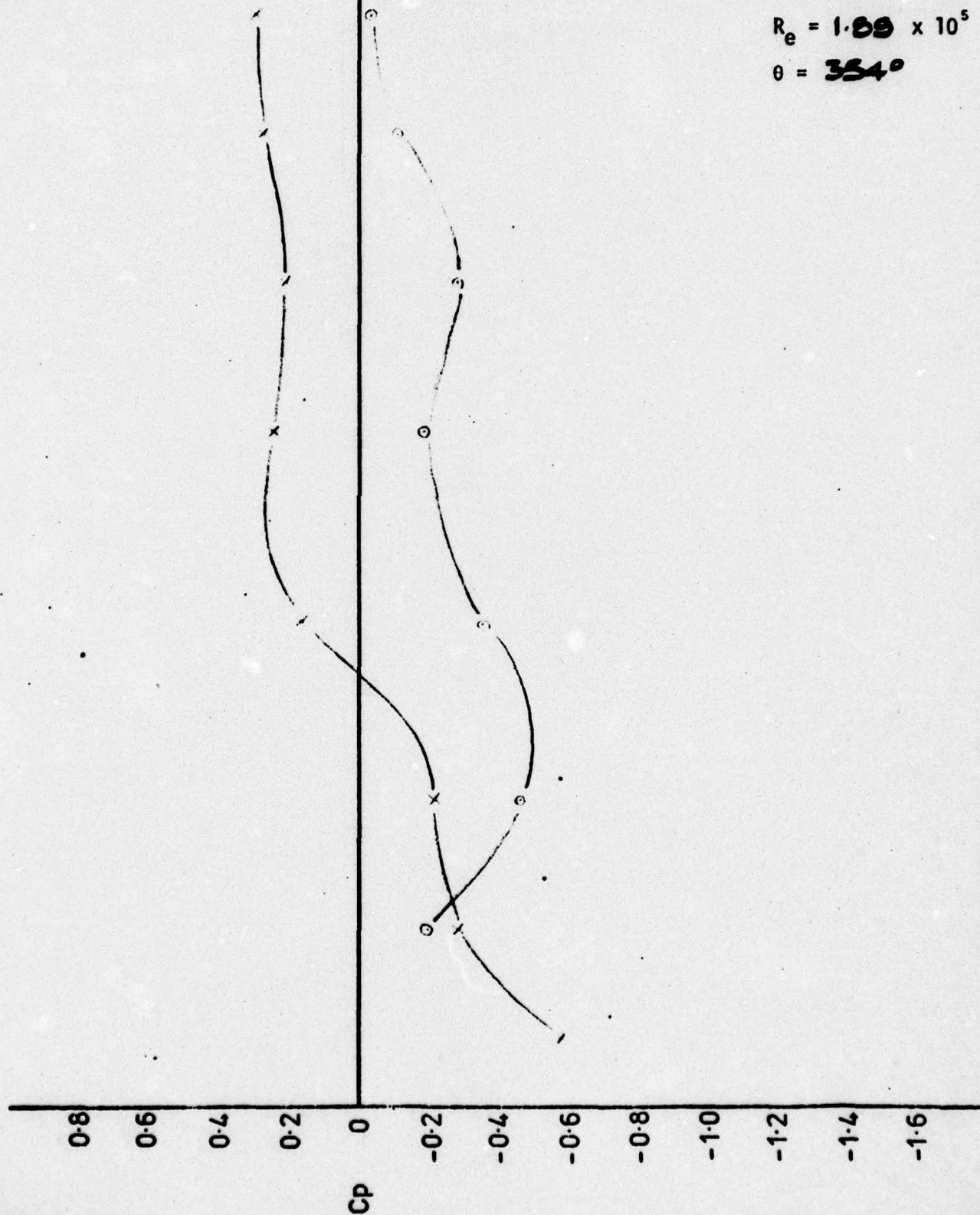
ROTOR UNSTEADY PRESSURE DISTRIBUTION

$N = 1250$ rev/min

$i = -13^\circ$

$R_e = 1.09 \times 10^5$

$\theta = 354^\circ$



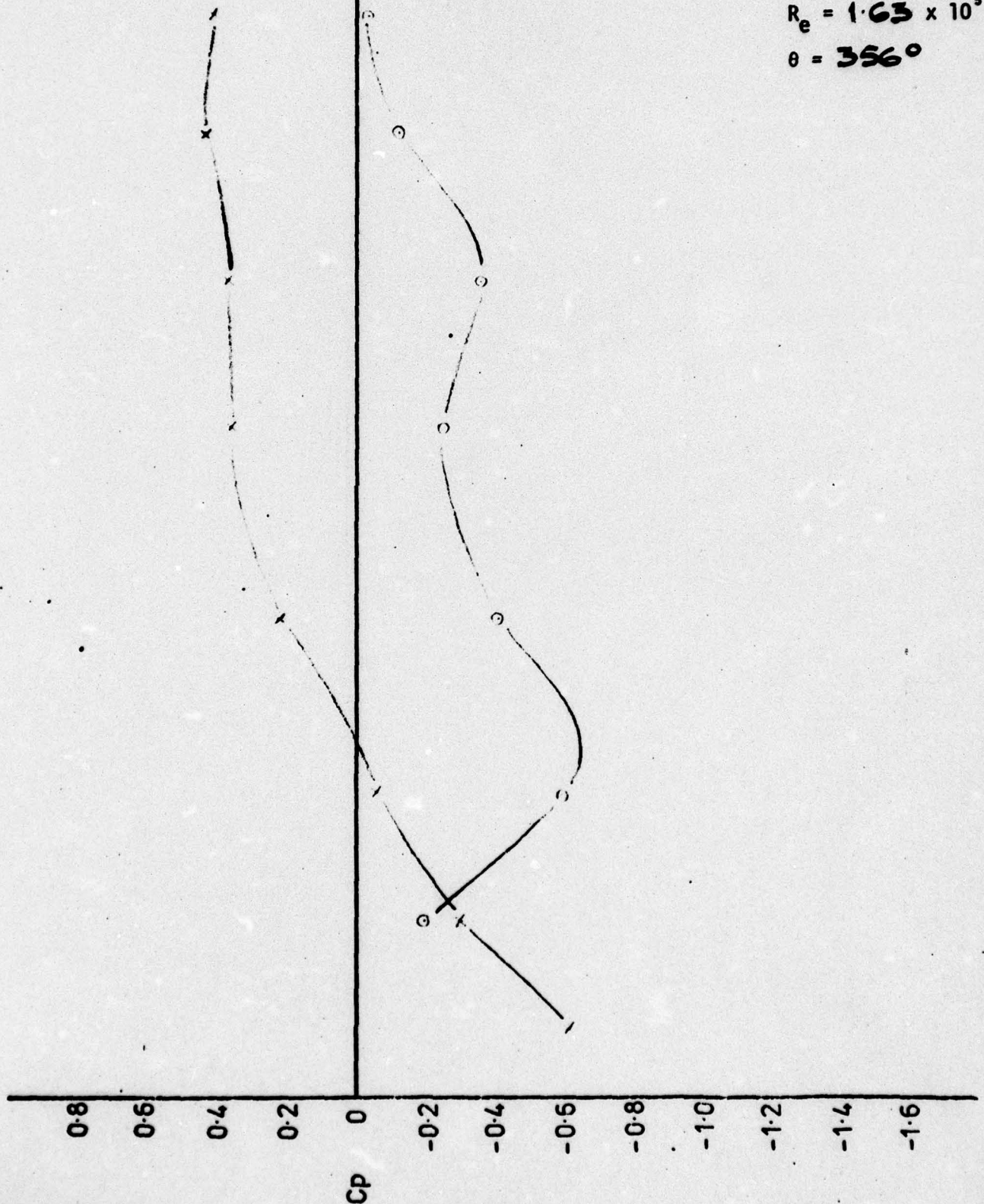
ROTOR UNSTEADY PRESSURE DISTRIBUTION

$N = 1250$ rev/min

$i = -80^\circ$

$R_e = 1.63 \times 10^5$

$\theta = 356^\circ$



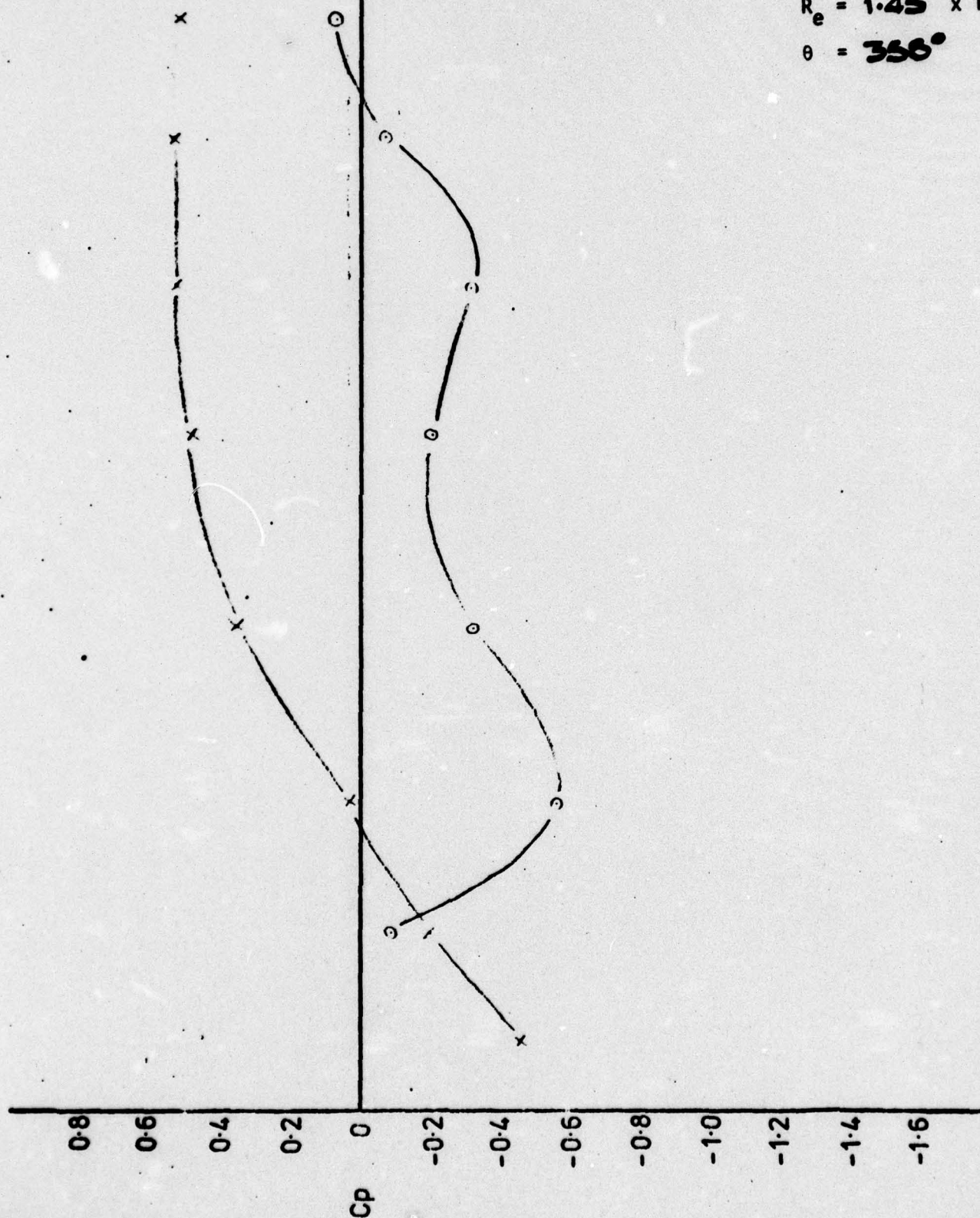
ROTOR UNSTEADY PRESSURE DISTRIBUTION

$N = 1250$ rev/min

$i = 0^\circ$

$R_e = 1.45 \times 10^5$

$\theta = 356^\circ$



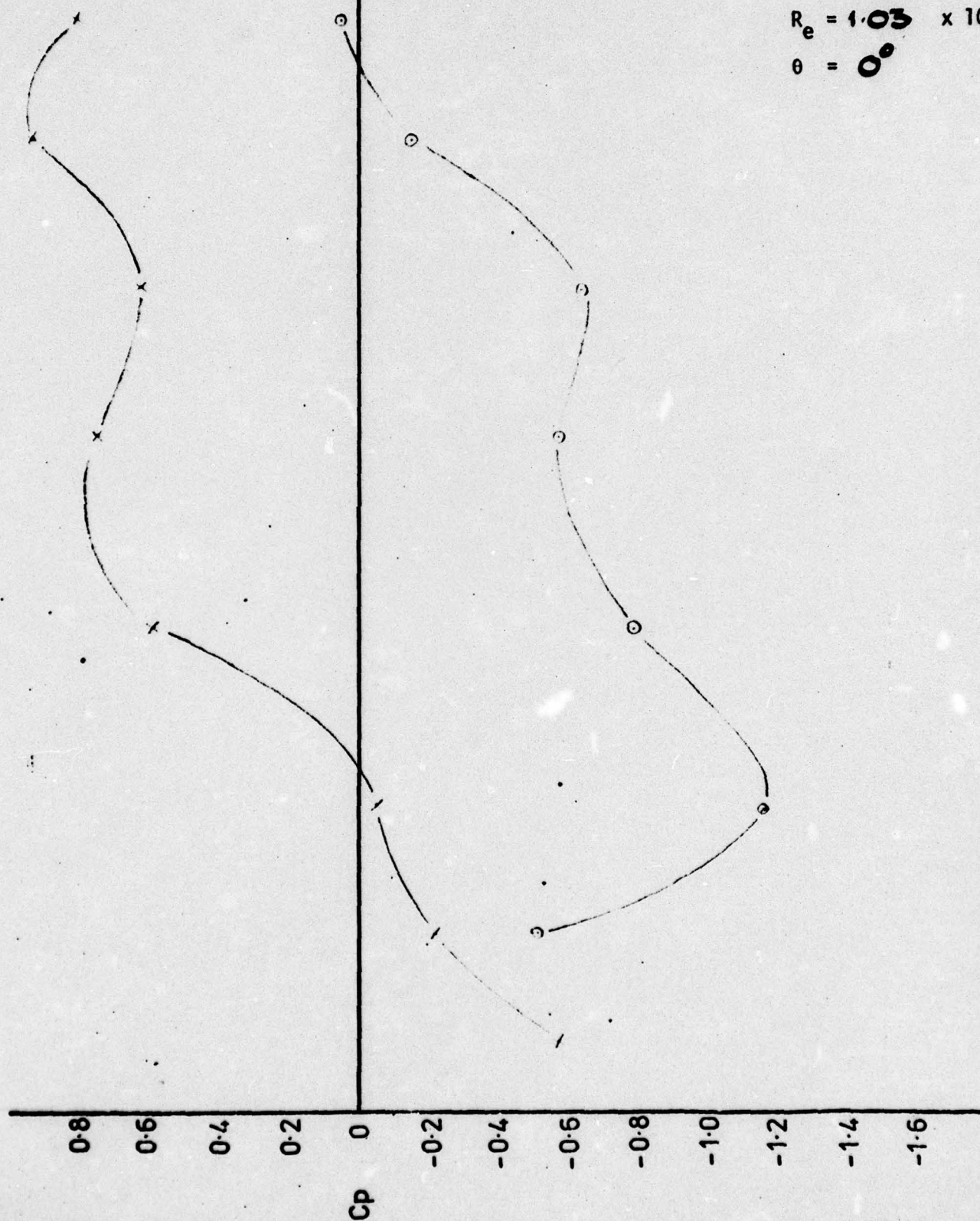
ROTOR UNSTEADY PRESSURE DISTRIBUTION

$N = 1250$ rev/min

$i = 50^\circ$

$R_e = 1.03 \times 10^5$

$\theta = 0^\circ$



ROTOR UNSTEADY PRESSURE DISTRIBUTION

$N = 1250$ rev/min

$i = 15.0^\circ$

$R_e = 1.35 \times 10^5$

$\theta = 2^\circ$



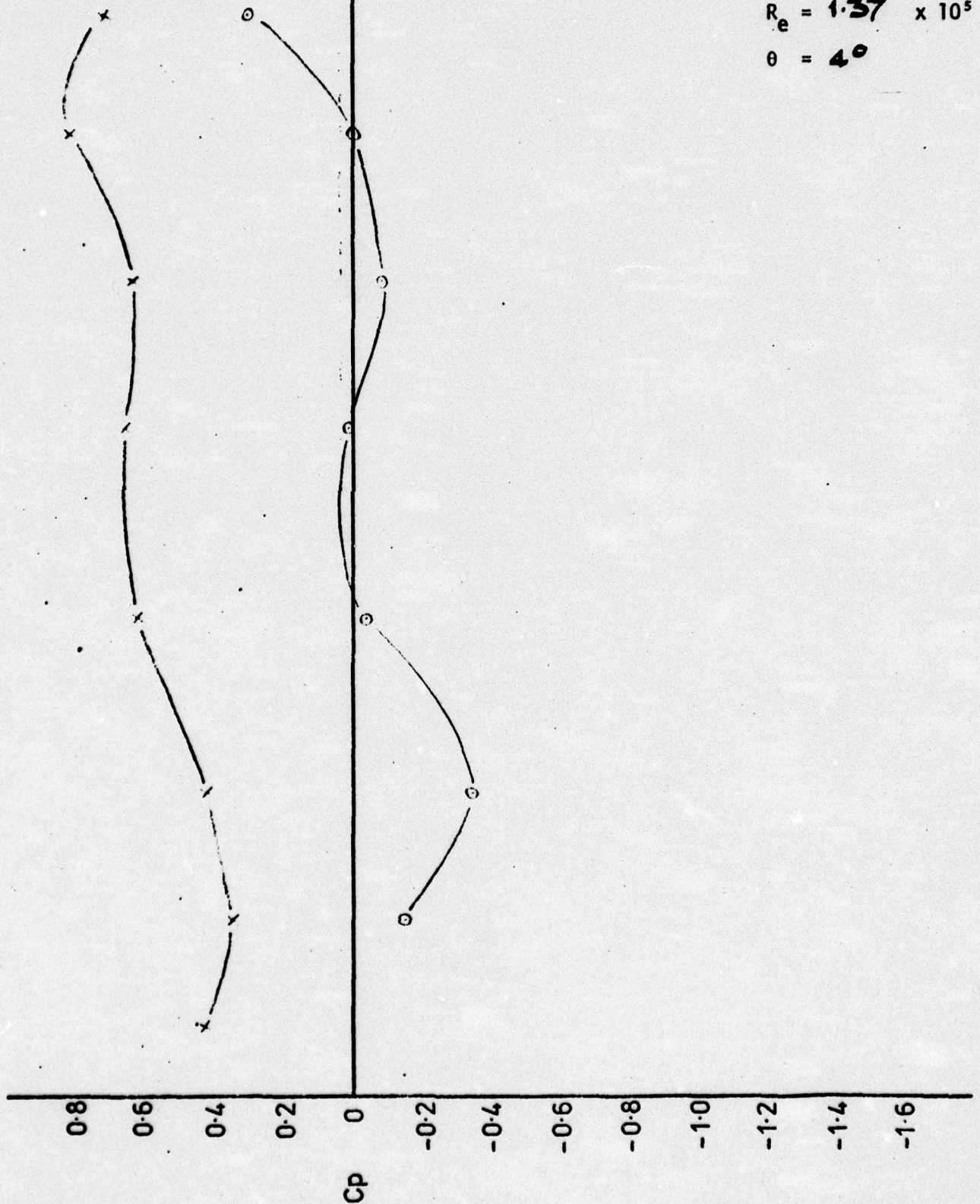
ROTOR UNSTEADY PRESSURE DISTRIBUTION

$N = 1250$ rev/min

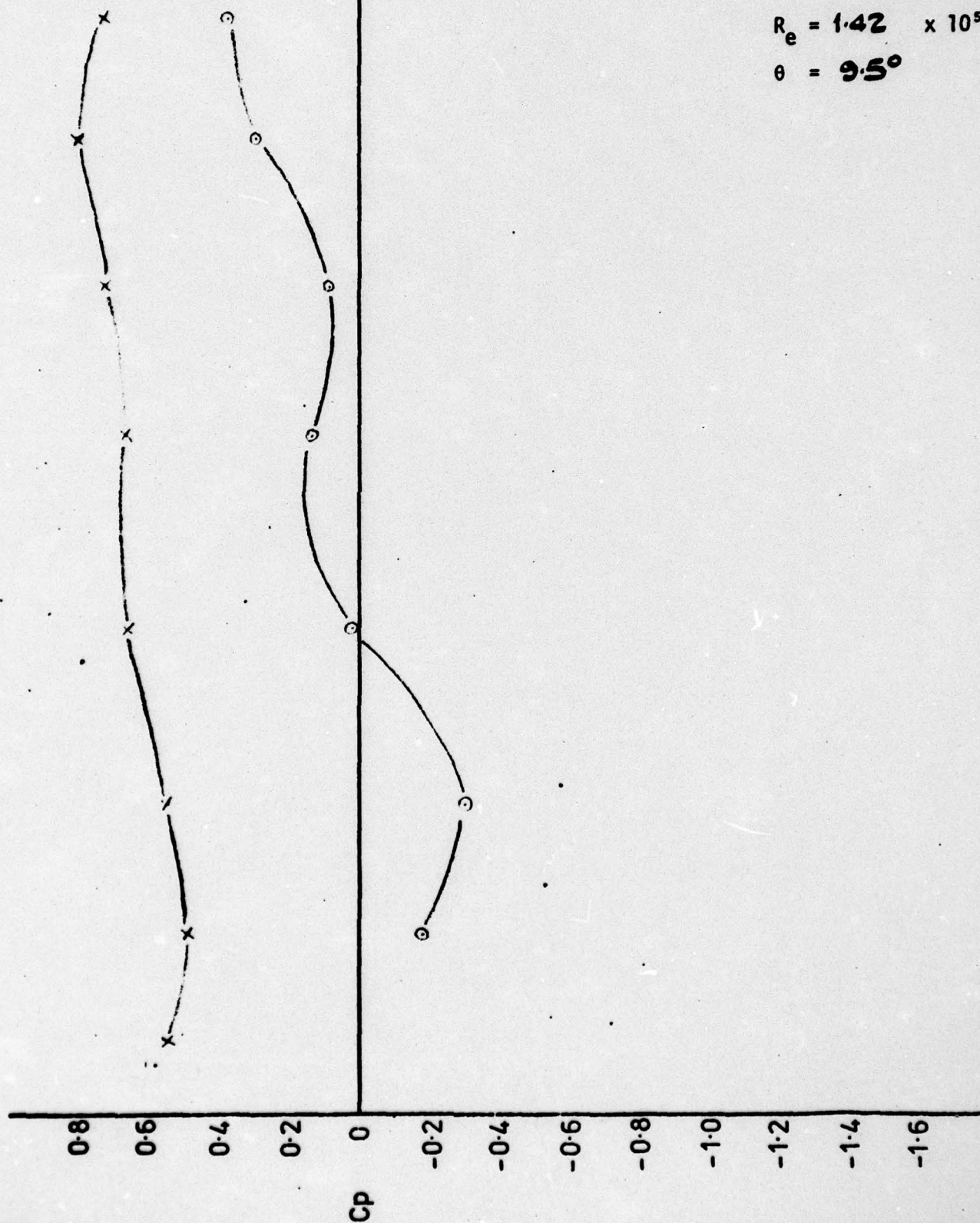
$i = 15.0^\circ$

$R_e = 1.37 \times 10^5$

$\theta = 4^\circ$



ROTOR UNSTEADY PRESSURE DISTRIBUTION

 $N = 1250$ rev/min $i = 15^\circ$ $R_e = 1.42 \times 10^5$ $\theta = 9.5^\circ$ 

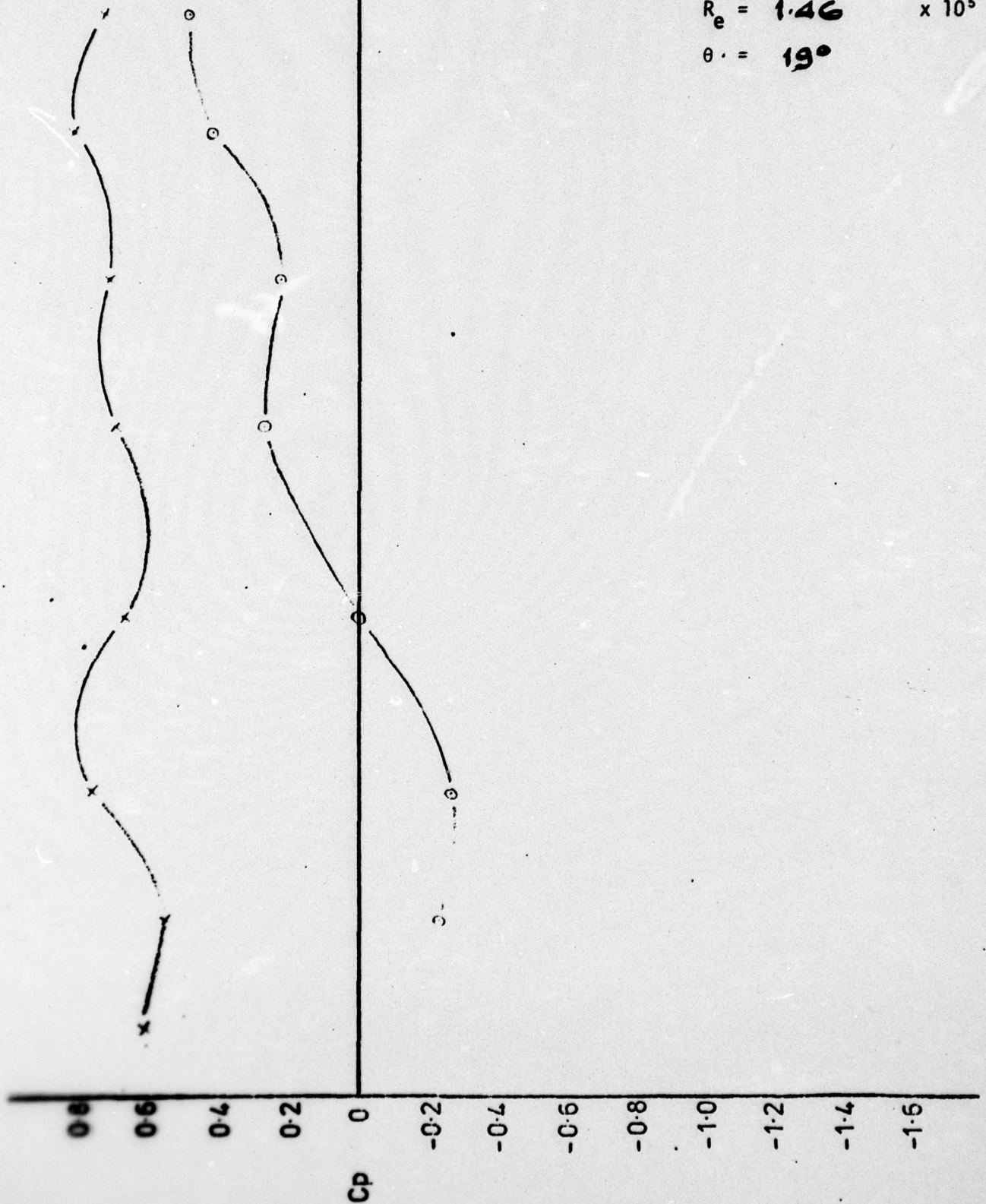
ROTOR UNSTEADY PRESSURE DISTRIBUTION

$N = 1250$ rev/min

$i = 14.4^\circ$

$R_e = 1.46 \times 10^5$

$\theta = 19^\circ$



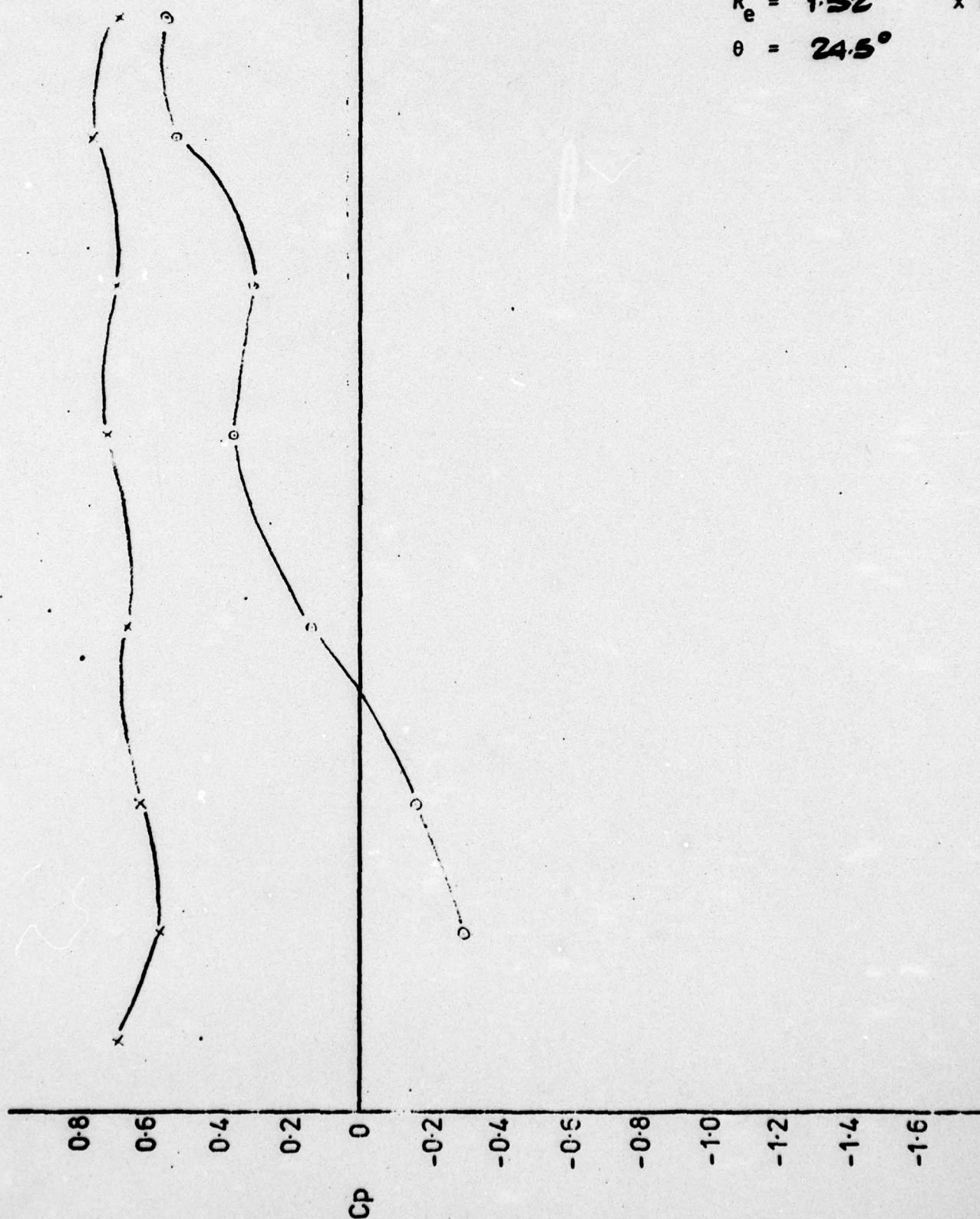
ROTOR UNSTEADY PRESSURE DISTRIBUTION

$N = 1250$ rev/min

$i = 15.0^\circ$

$R_e = 1.52 \times 10^5$

$\theta = 24.5^\circ$



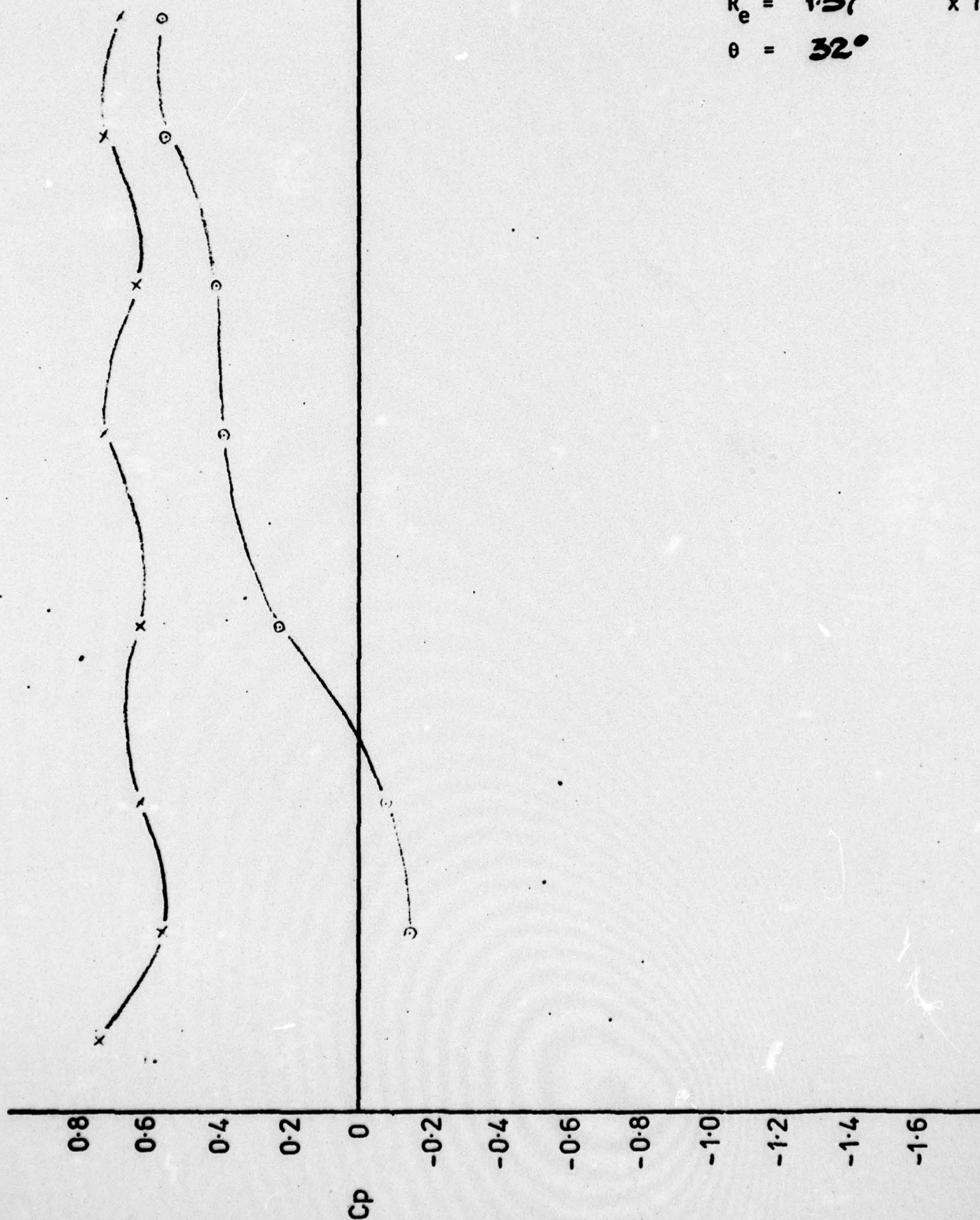
ROTOR UNSTEADY PRESSURE DISTRIBUTION

$N = 1250$ rev/min

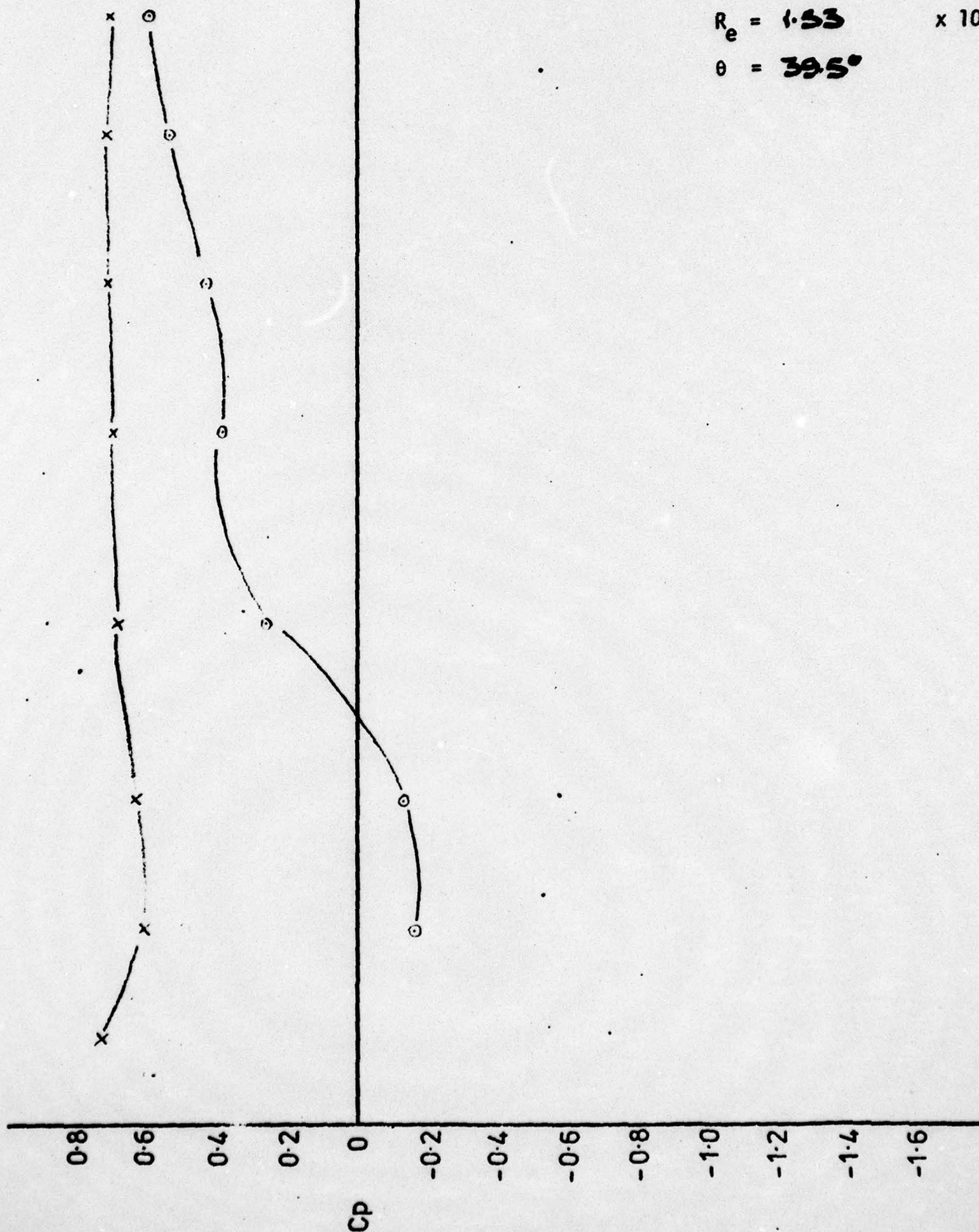
$i = 16.0^\circ$

$R_e = 1.57 \times 10^5$

$\theta = 32^\circ$



ROTOR UNSTEADY PRESSURE DISTRIBUTION

 $N = 1250$ rev/min $i = 16.0^\circ$ $R_e = 1.53 \times 10^5$ $\theta = 39.5^\circ$ 

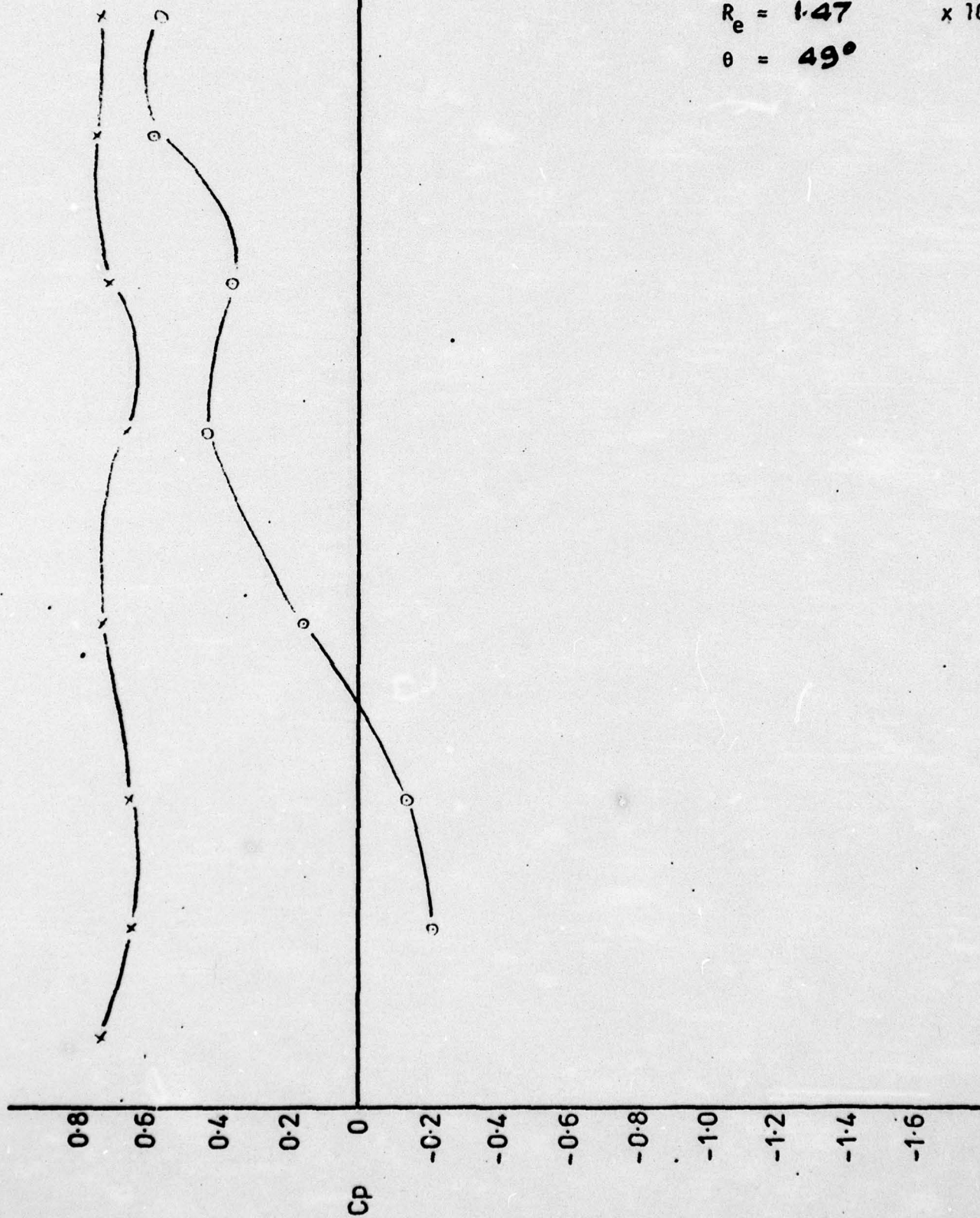
ROTOR UNSTEADY PRESSURE DISTRIBUTION

$N = 1250$ rev/min

$i = 16.1^\circ$

$R_e = 1.47 \times 10^5$

$\theta = 49^\circ$



ROTOR UNSTEADY PRESSURE DISTRIBUTION

$N = 1250$ rev/min

$i = 18.0^\circ$

$R_e = 1.50 \times 10^5$

$\theta = 64.0^\circ$



ROTOR UNSTEADY PRESSURE DISTRIBUTION

 $N = 1250$ rev/min $i = 19.2^\circ$ $R_e = 1.46 \times 10^5$ $\theta = 69.5^\circ$ 

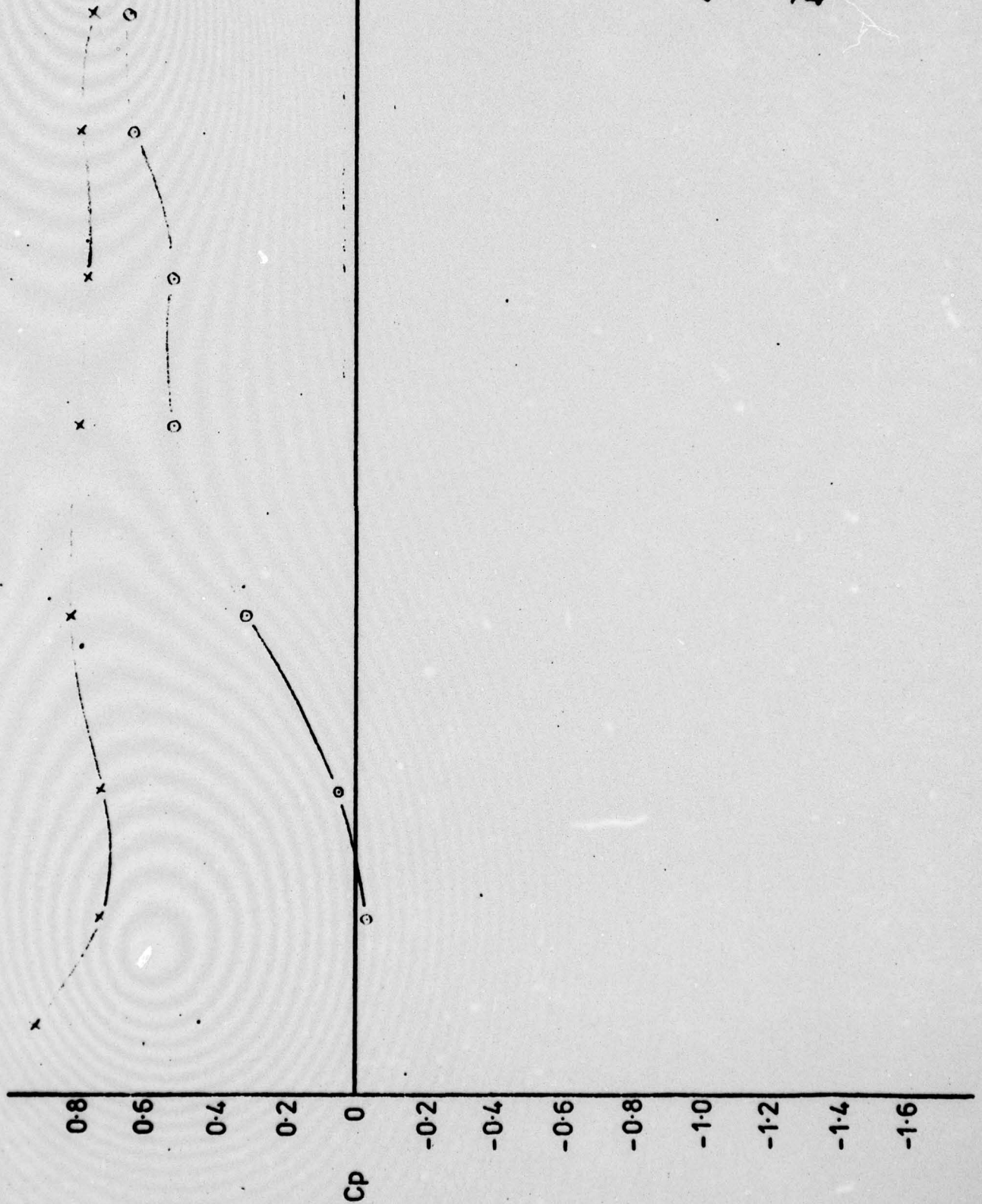
ROTOR UNSTEADY PRESSURE DISTRIBUTION

$N = 1250$ rev/min

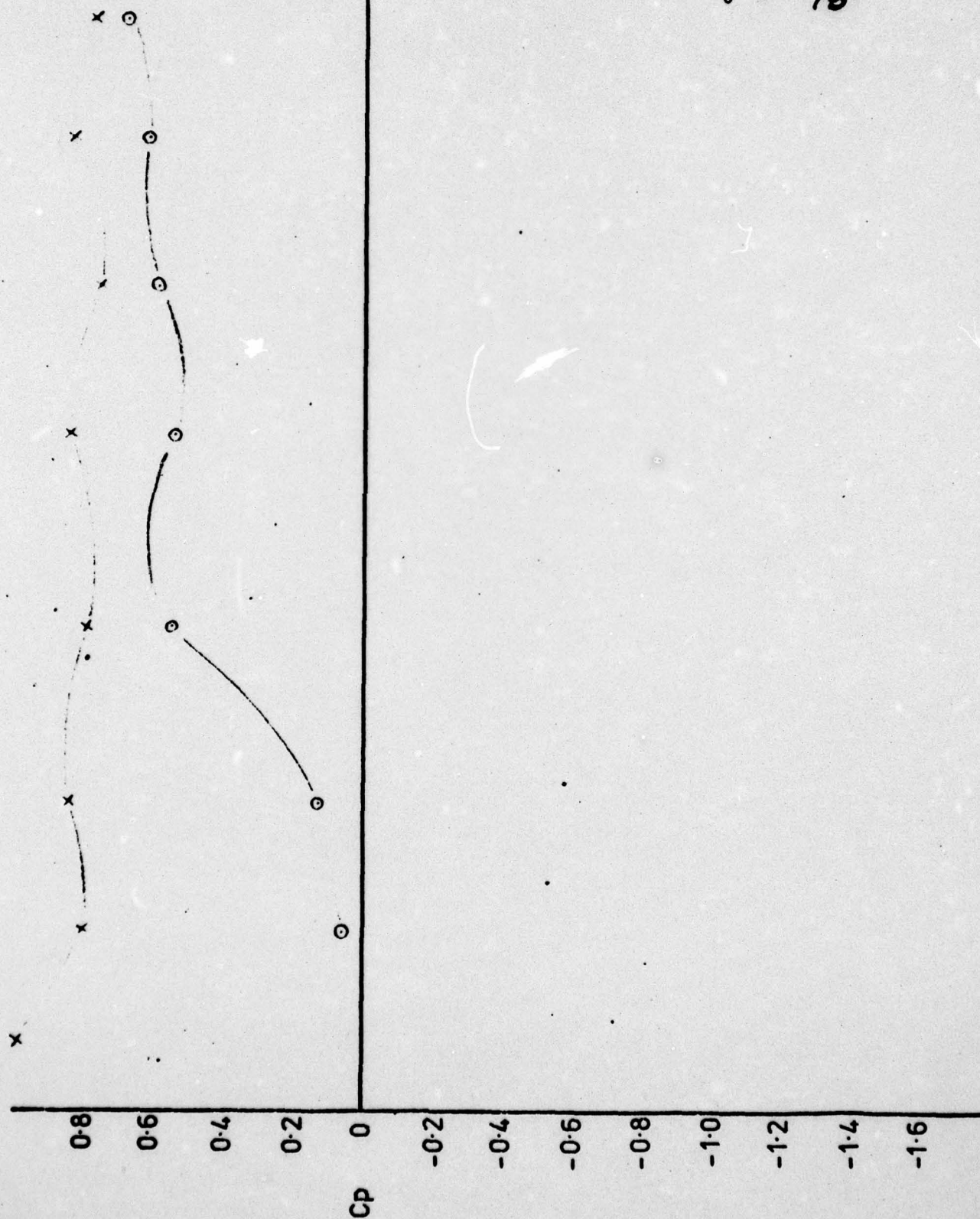
$i = 21.0^\circ$

$R_e = 1.49 \times 10^5$

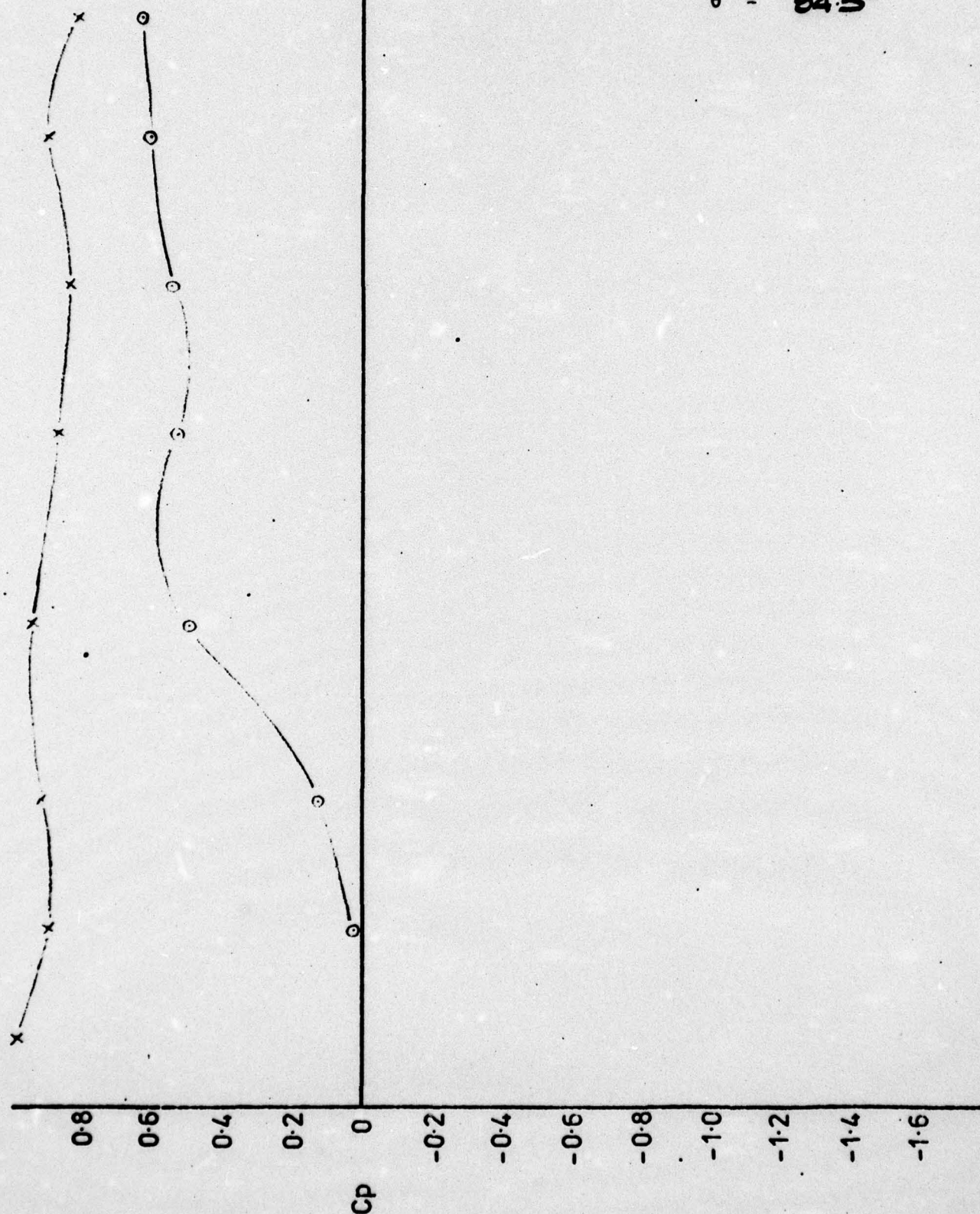
$\theta = 74^\circ$



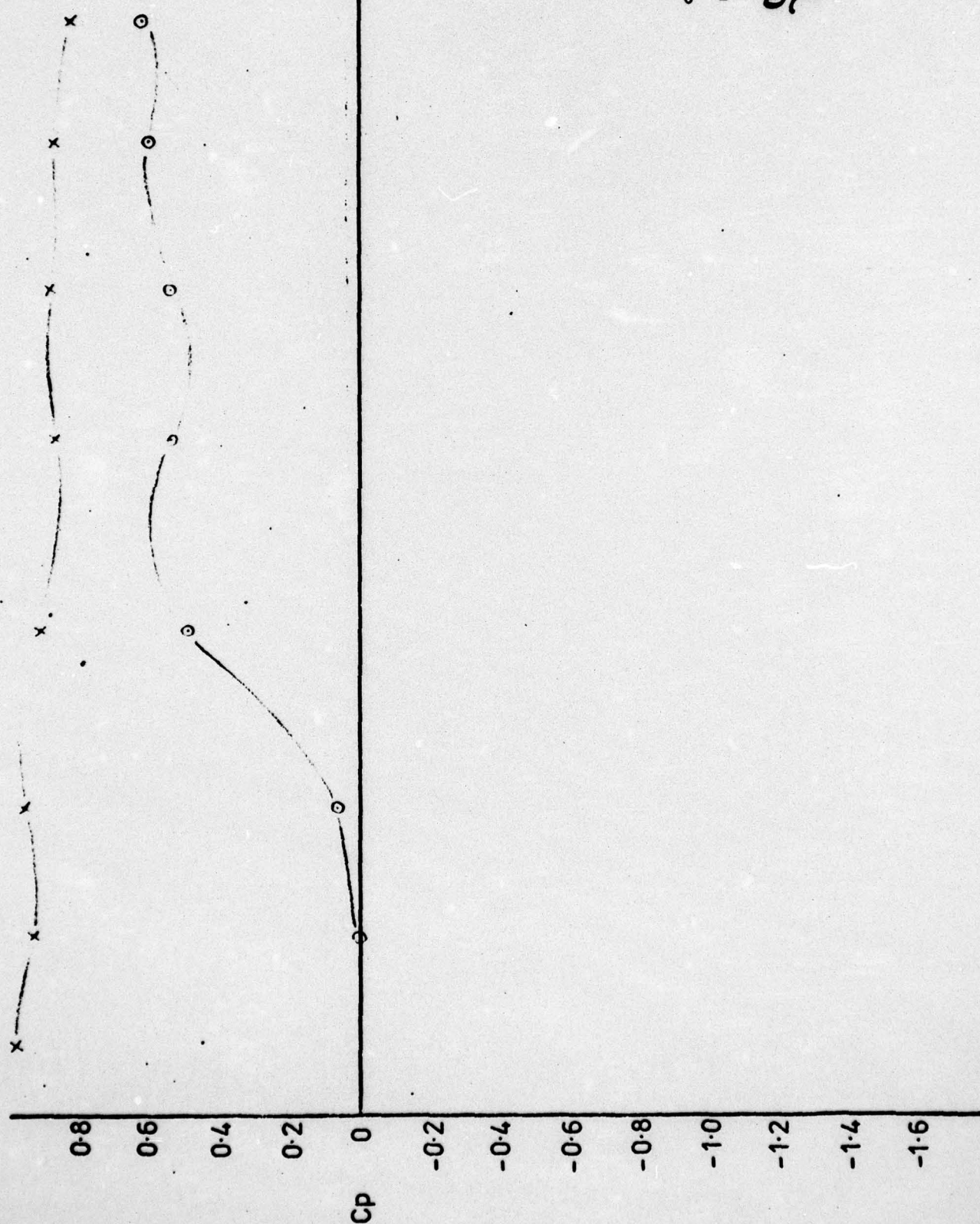
ROTOR UNSTEADY PRESSURE DISTRIBUTION

 $N = 1250$ rev/min $i = 23.5^\circ$ $R_e = 1.46 \times 10^5$ $\theta = 79^\circ$ 

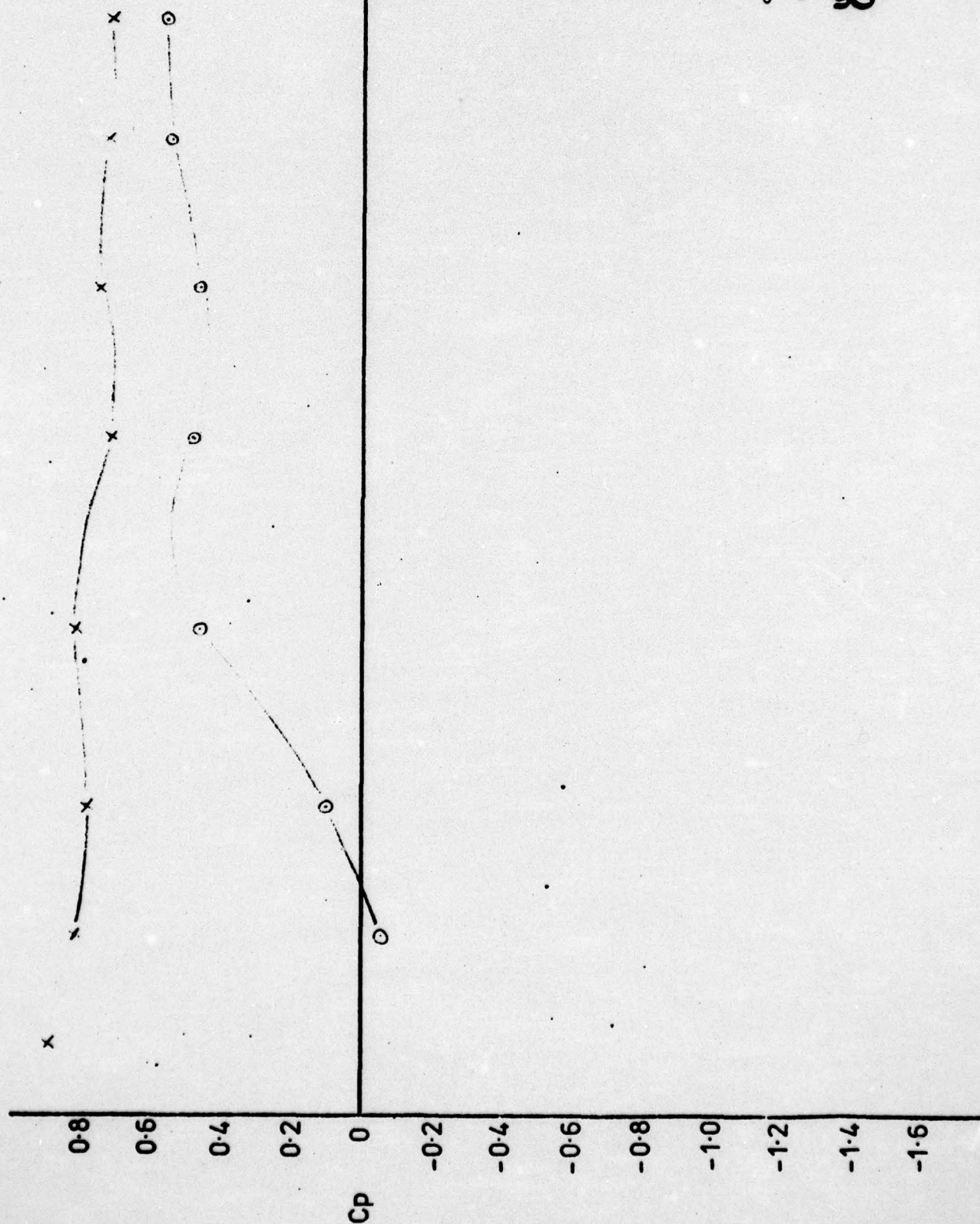
ROTOR UNSTEADY PRESSURE DISTRIBUTION

 $N = 1250$ rev/min $i = 23^\circ$ $R_e = 1.42 \times 10^5$ $\theta = 84.5^\circ$ 

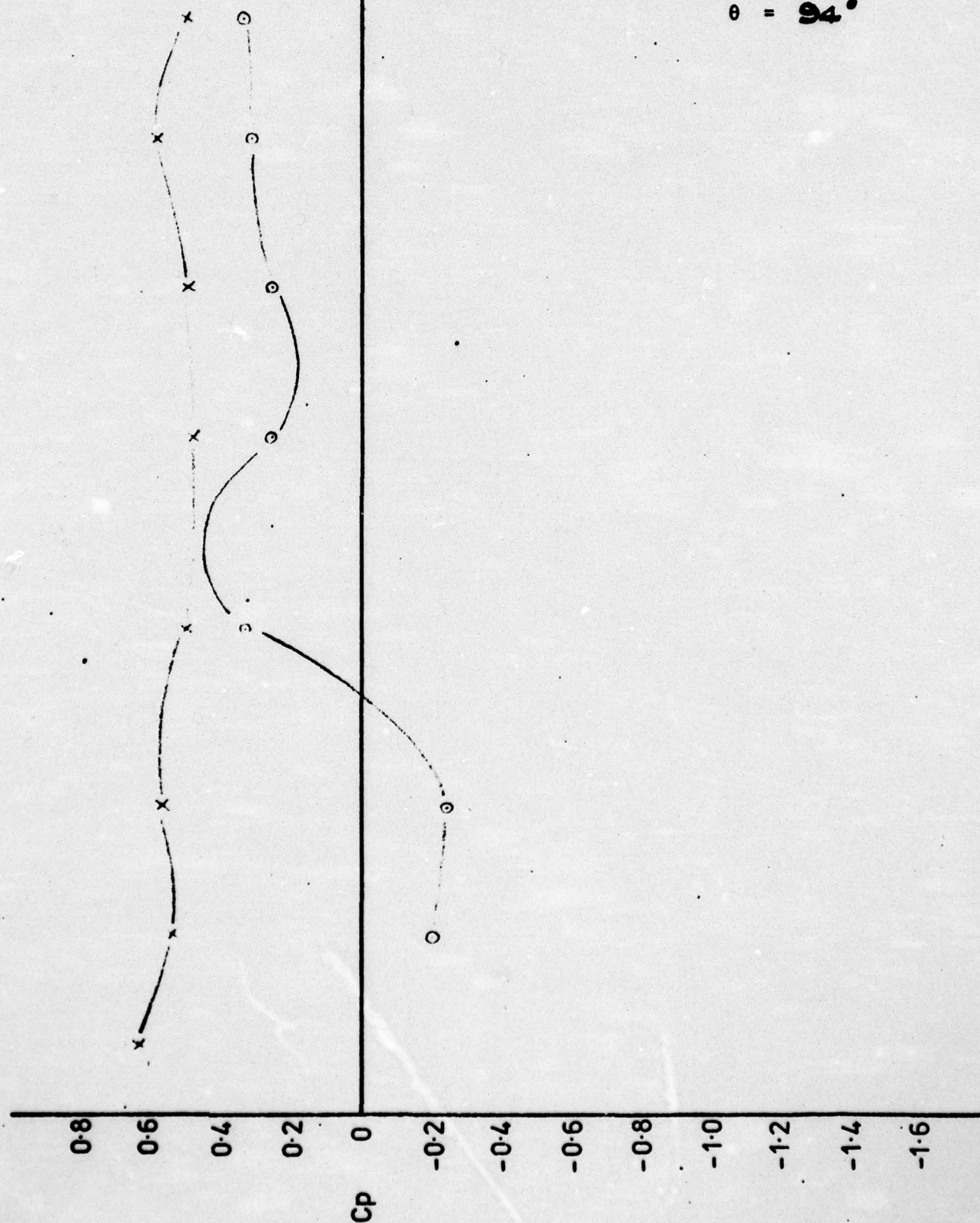
ROTOR UNSTEADY PRESSURE DISTRIBUTION

 $N = 1250$ rev/min $i = 24^\circ$ $R_e = 1.38 \times 10^5$ $\theta = 87^\circ$ 

ROTOR UNSTEADY PRESSURE DISTRIBUTION

 $N = 1250$ rev/min $i = 19.0^\circ$ $R_e = 1.59 \times 10^5$ $\theta = 90^\circ$ 

ROTOR UNSTEADY PRESSURE DISTRIBUTION

 $N = 1250$ rev/min $i = 2.5^\circ$ $R_e = 1.02 \times 10^5$ $\theta = 94^\circ$ 

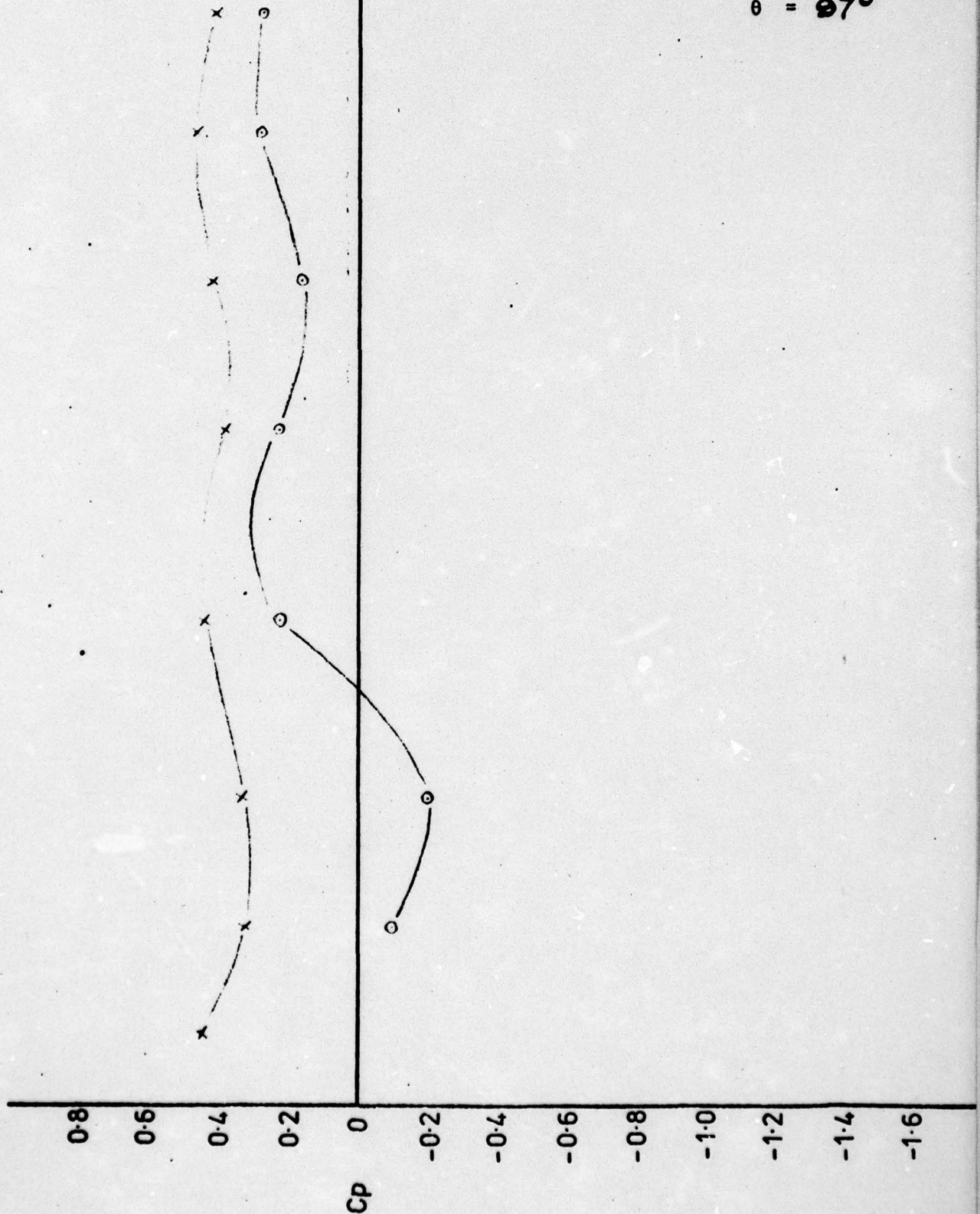
ROTOR UNSTEADY PRESSURE DISTRIBUTION

$N = 1250$ rev/min

$i = 0^\circ$

$R_e = 1.93 \times 10^5$

$\theta = 97^\circ$



AD-A041 726

CRANFIELD INST OF TECH (ENGLAND) SCHOOL OF MECHANICA--ETC F/G 20/4
SQUARE-WAVE CIRCUMFERENTIAL PRESSURE DISTORTION EFFECTS IN COMP--ETC(U)
MAR 77 R E PEACOCK AF-AFOSR-2708-74

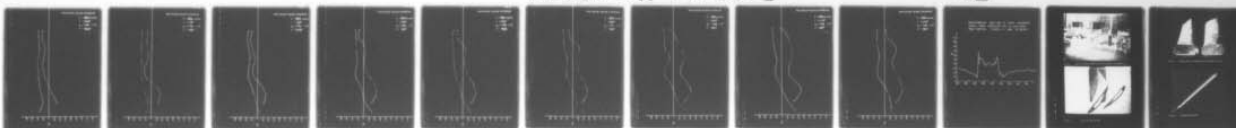
UNCLASSIFIED

AFOSR-TR-77-0075

NL

2 OF 2

AD
A041 726



END

DATE
FILMED
8-77

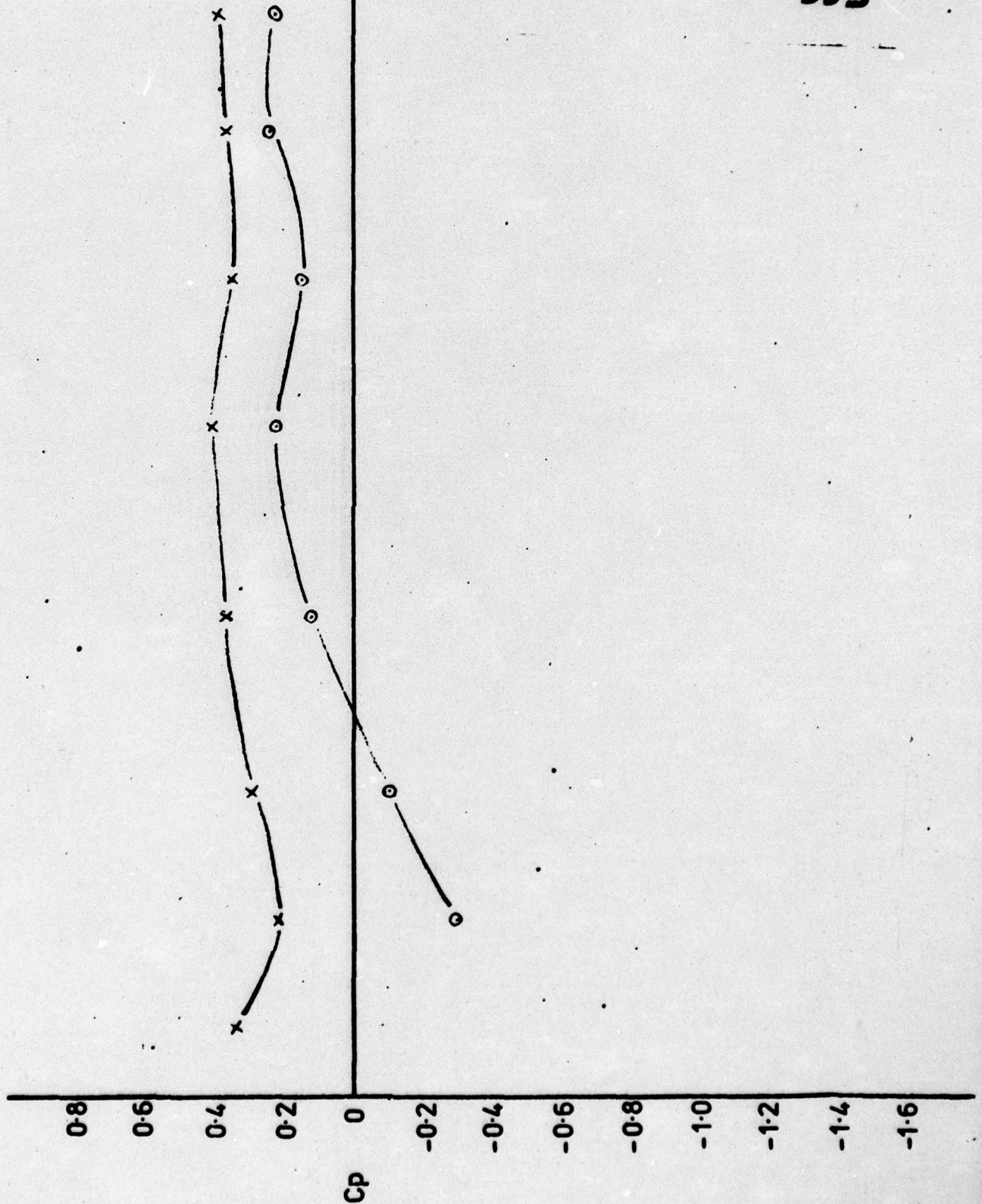
ROTOR UNSTEADY PRESSURE DISTRIBUTION

$N = 1250$ rev/min

$\beta = -0.5^\circ$

$R_e = 1.89 \times 10^5$

$\theta = 99.5^\circ$



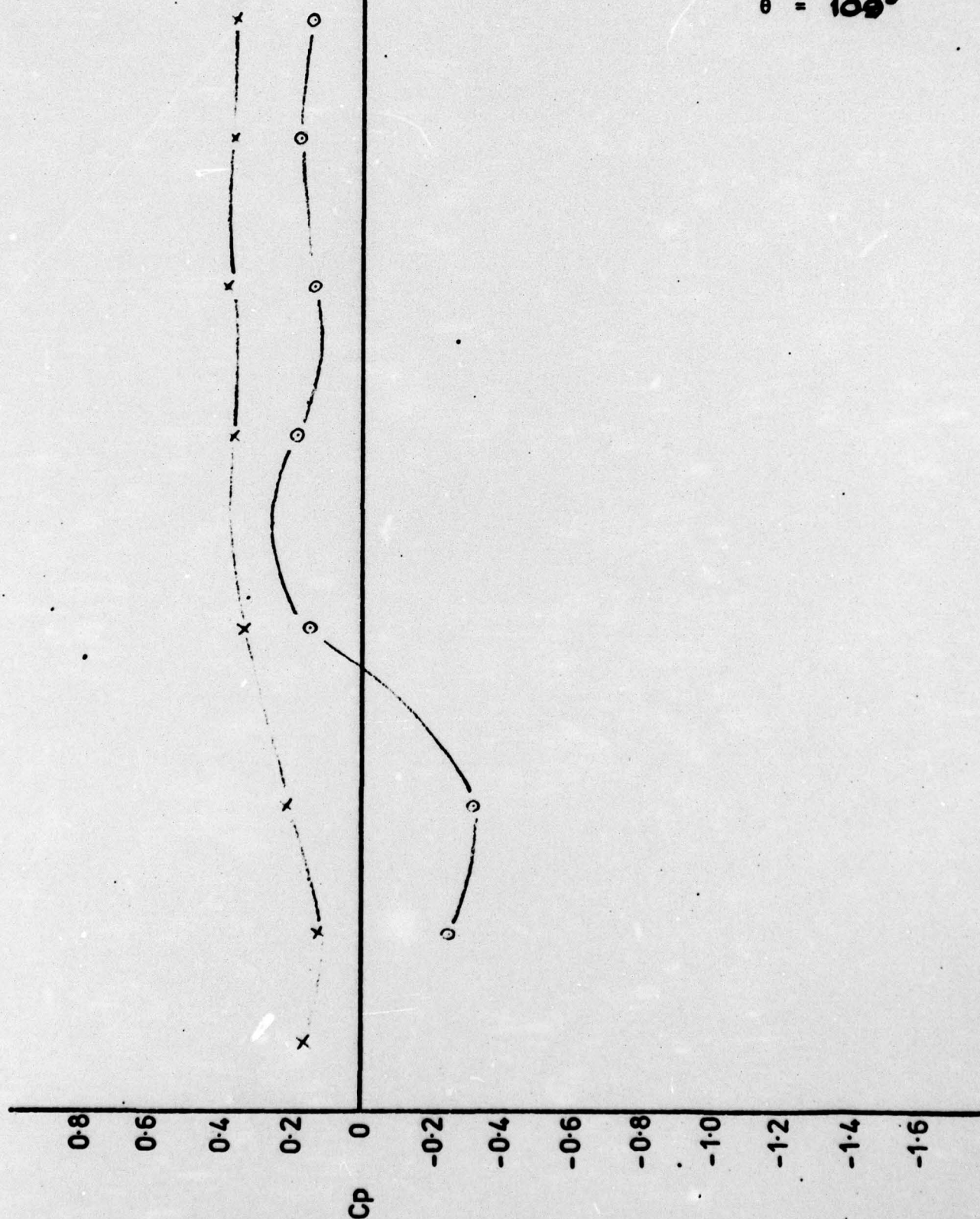
ROTOR UNSTEADY PRESSURE DISTRIBUTION

$N = 1250$ rev/min

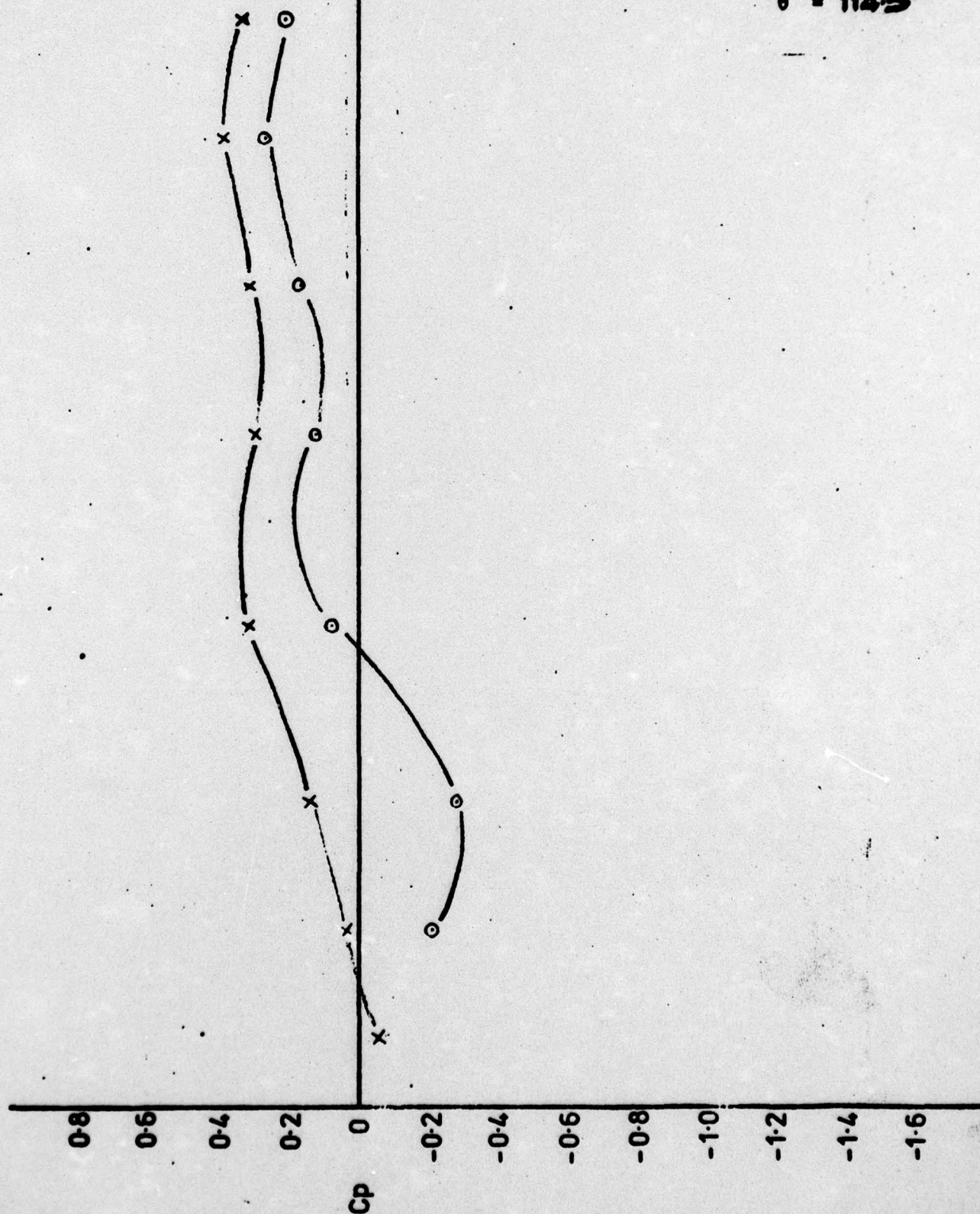
$i = -1.5^\circ$

$R_e = 1.79 \times 10^5$

$\theta = 109^\circ$



ROTOR UNSTEADY PRESSURE DISTRIBUTION

 $N = 1250$ rev/min $\beta = -20^\circ$ $R_e = 1.76 \times 10^5$ $\theta = 114.5^\circ$ 

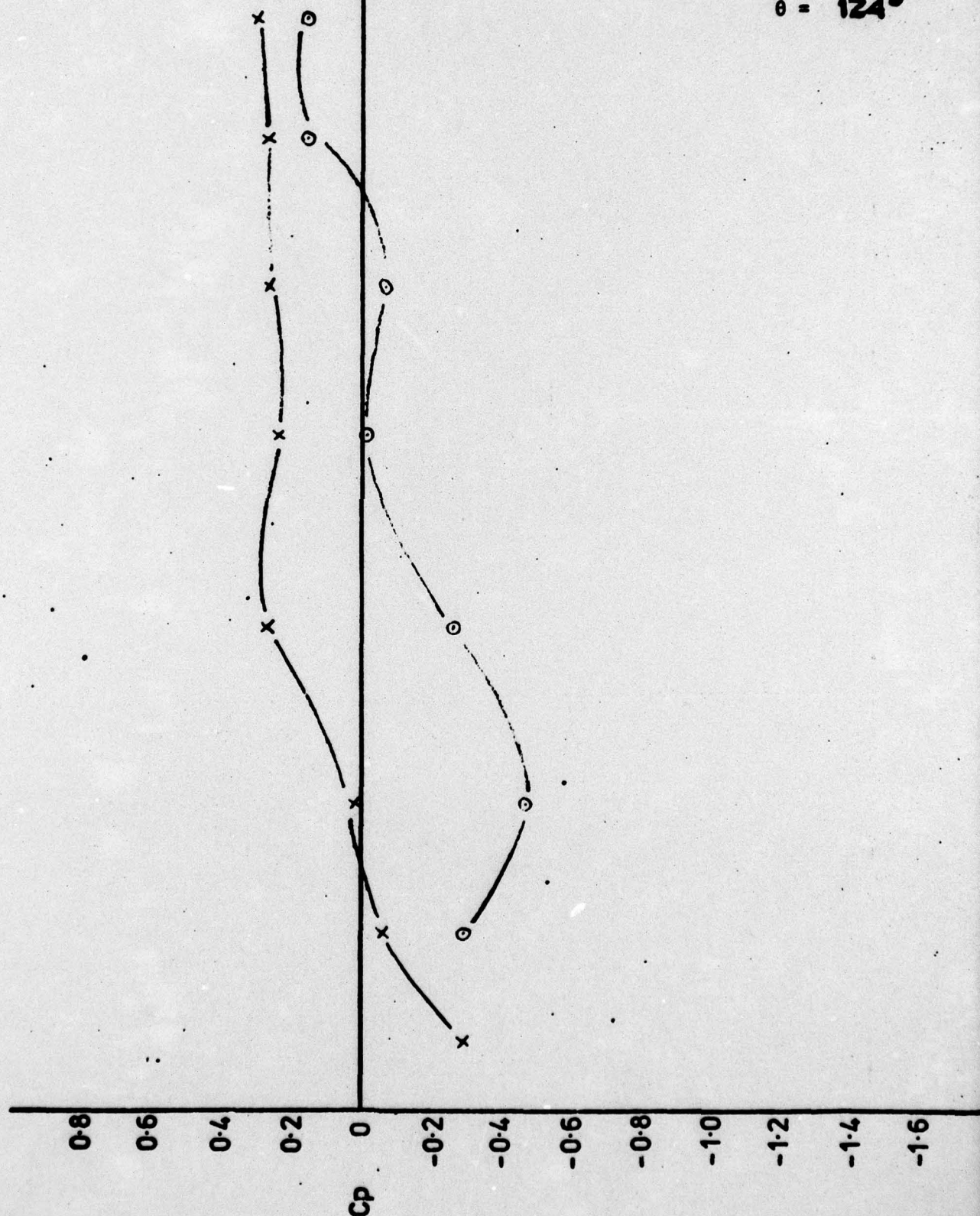
ROTOR UNSTEADY PRESSURE DISTRIBUTION

$N = 1260$ rev/min

$i = -26^\circ$

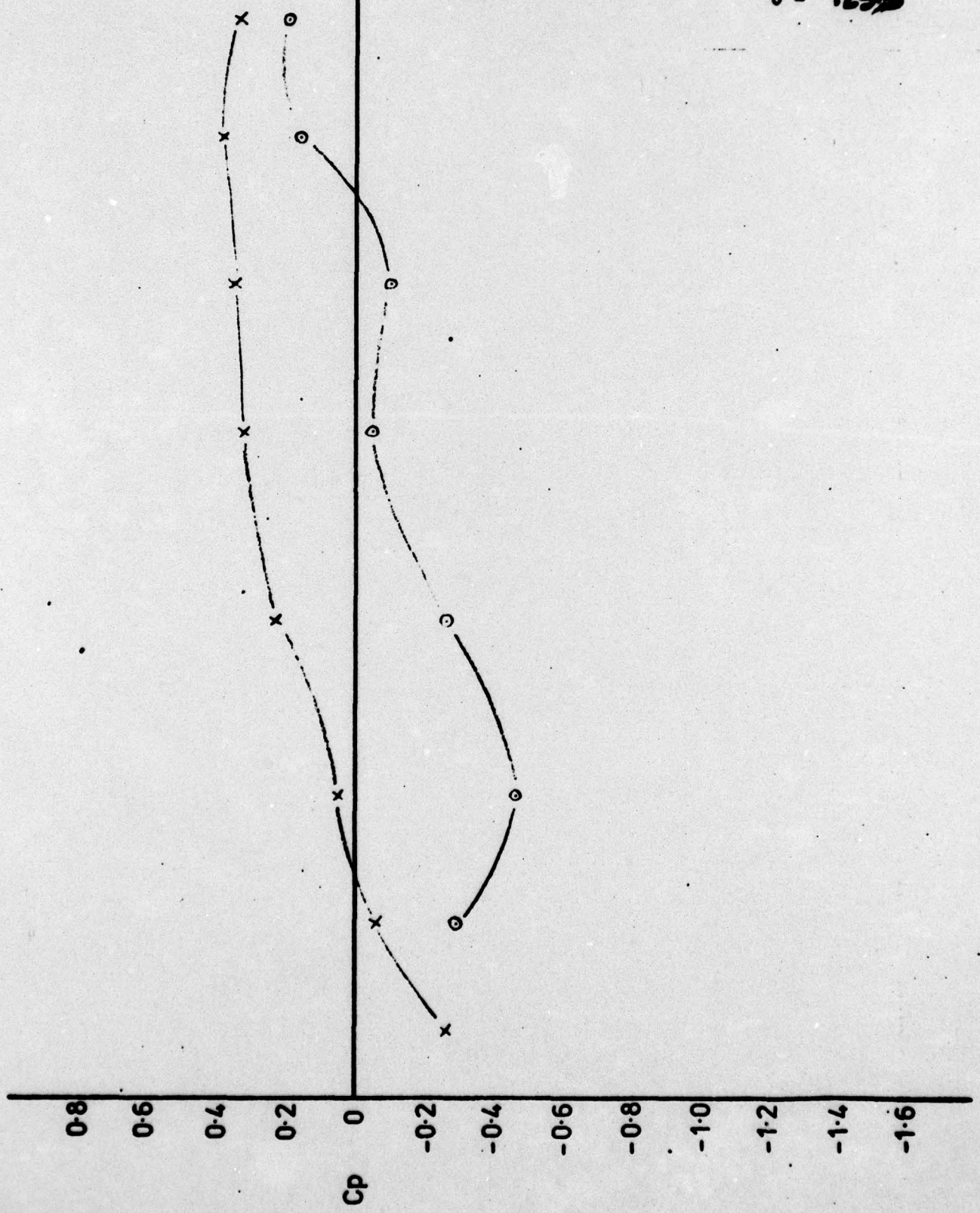
$Re = 1.73 \times 10^5$

$\theta = 124^\circ$



ROTOR UNSTEADY PRESSURE DISTRIBUTION

$N = 1250$ rev/min
 $\beta = -2.6^\circ$
 $R_e = 1.73 \times 10^5$
 $\theta = 129.6$



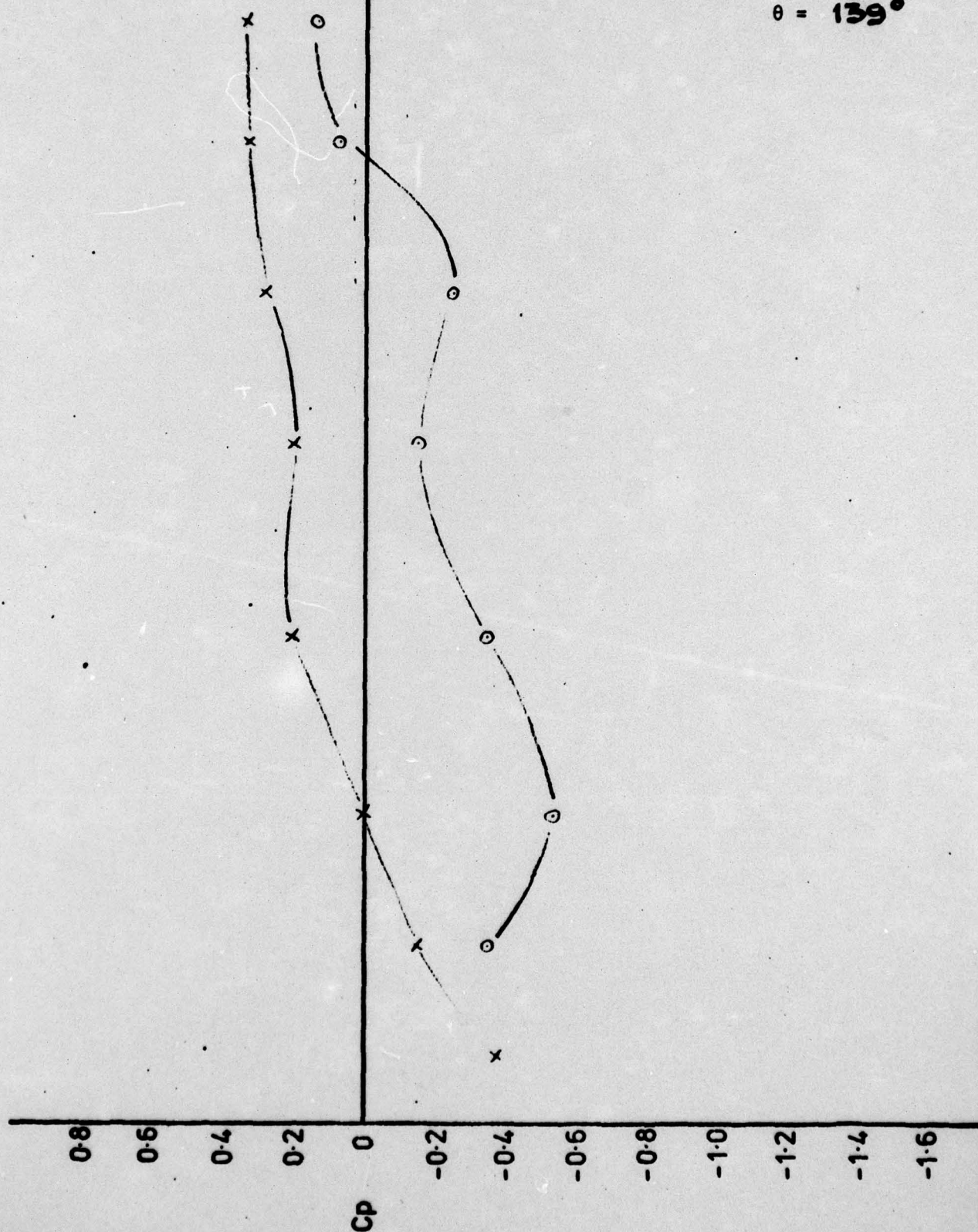
ROTOR UNSTEADY PRESSURE DISTRIBUTION

$N = 1250$ rev/min

$i = -32^\circ$

$R_e = 1.71 \times 10^5$

$\theta = 139^\circ$



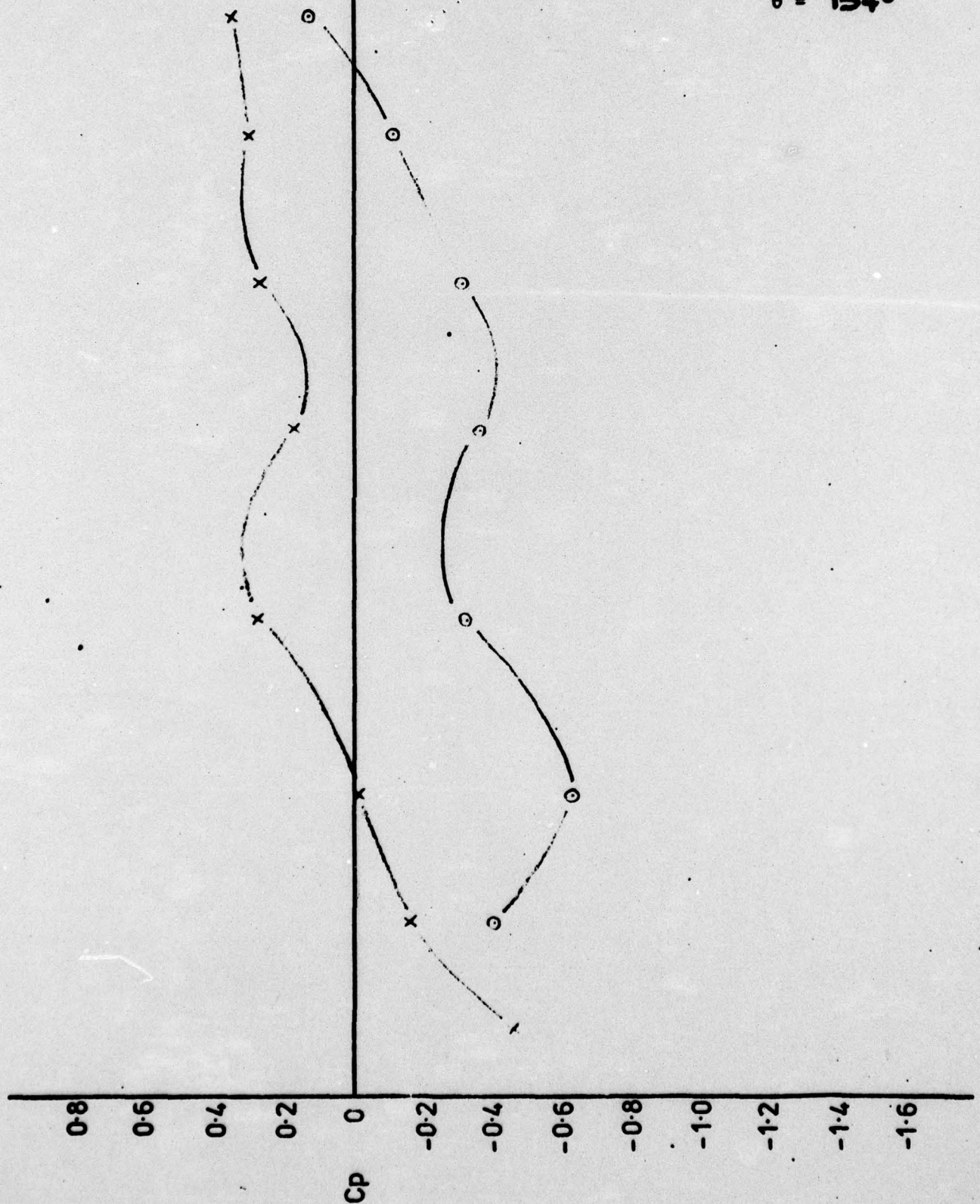
ROTOR UNSTEADY PRESSURE DISTRIBUTION

$N = 1250$ rev/min

$\Gamma = -3.8^\circ$

$R_e = 1.68 \times 10^5$

$\theta = 154^\circ$



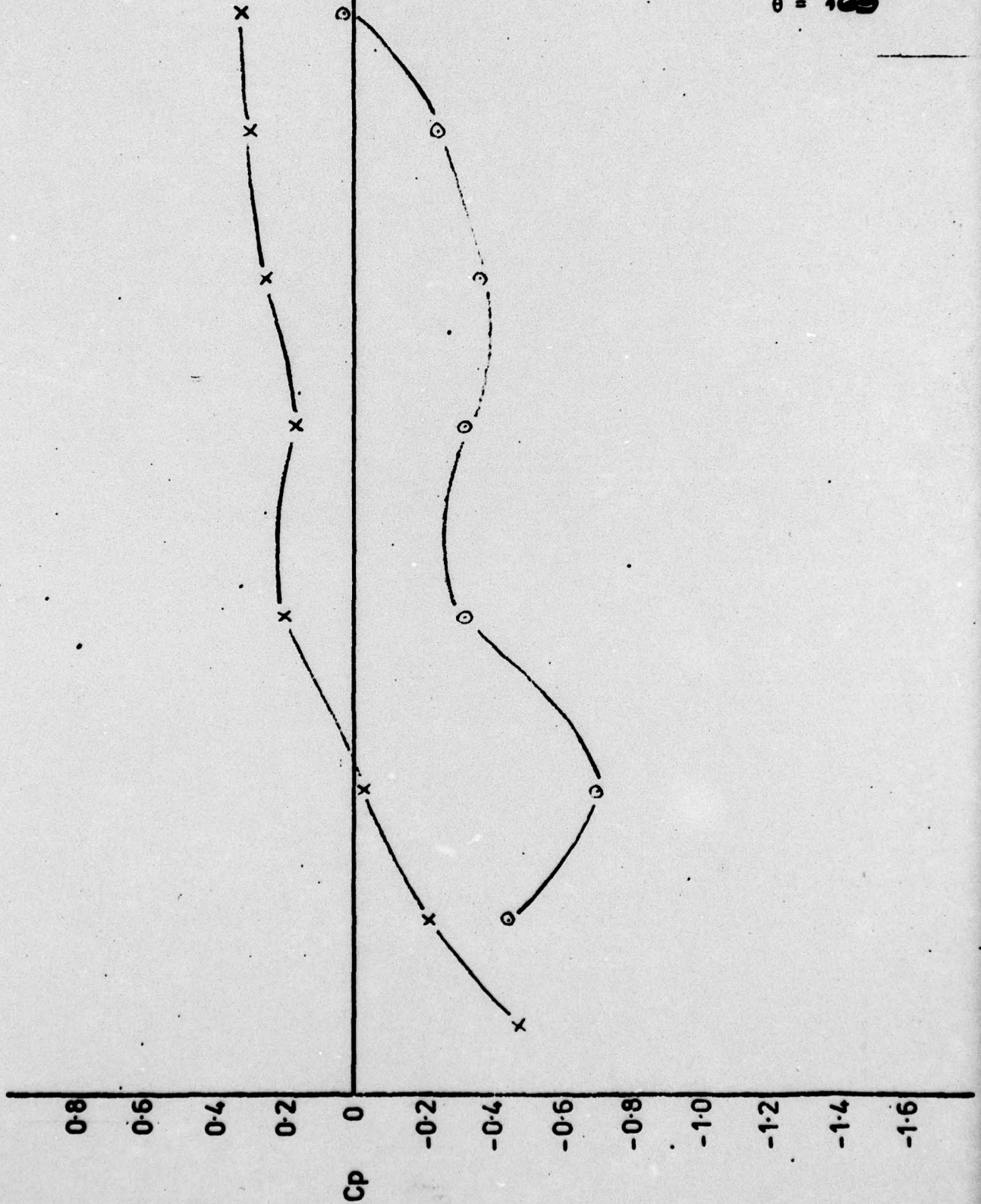
ROTOR UNSTEADY PRESSURE DISTRIBUTION

$N = 1250$ rev/min

$\beta = -4.0^\circ$

$R_e = 1.69 \times 10^6$

$\theta = 169^\circ$



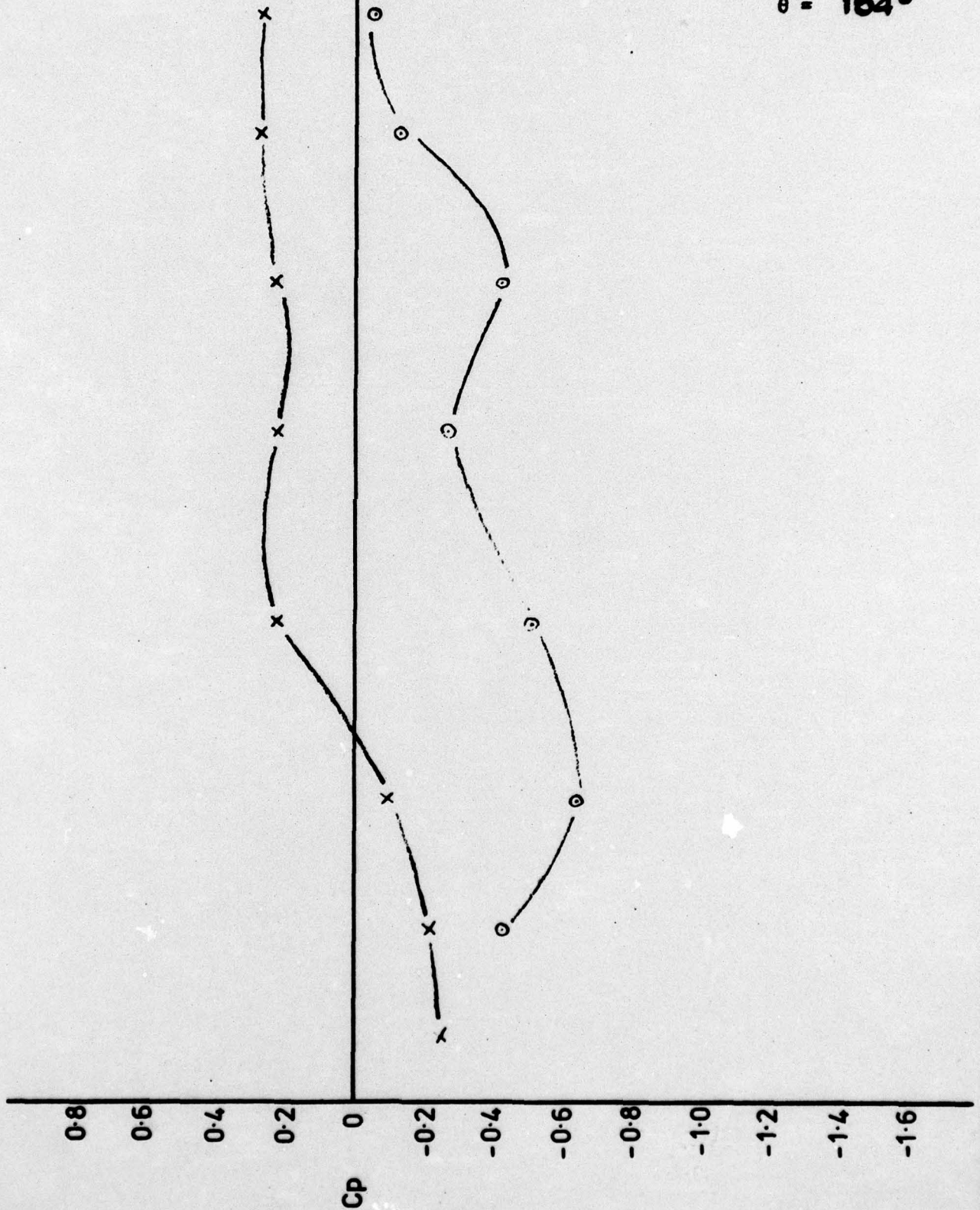
ROTOR UNSTEADY PRESSURE DISTRIBUTION

$N = 1250$ rev/min

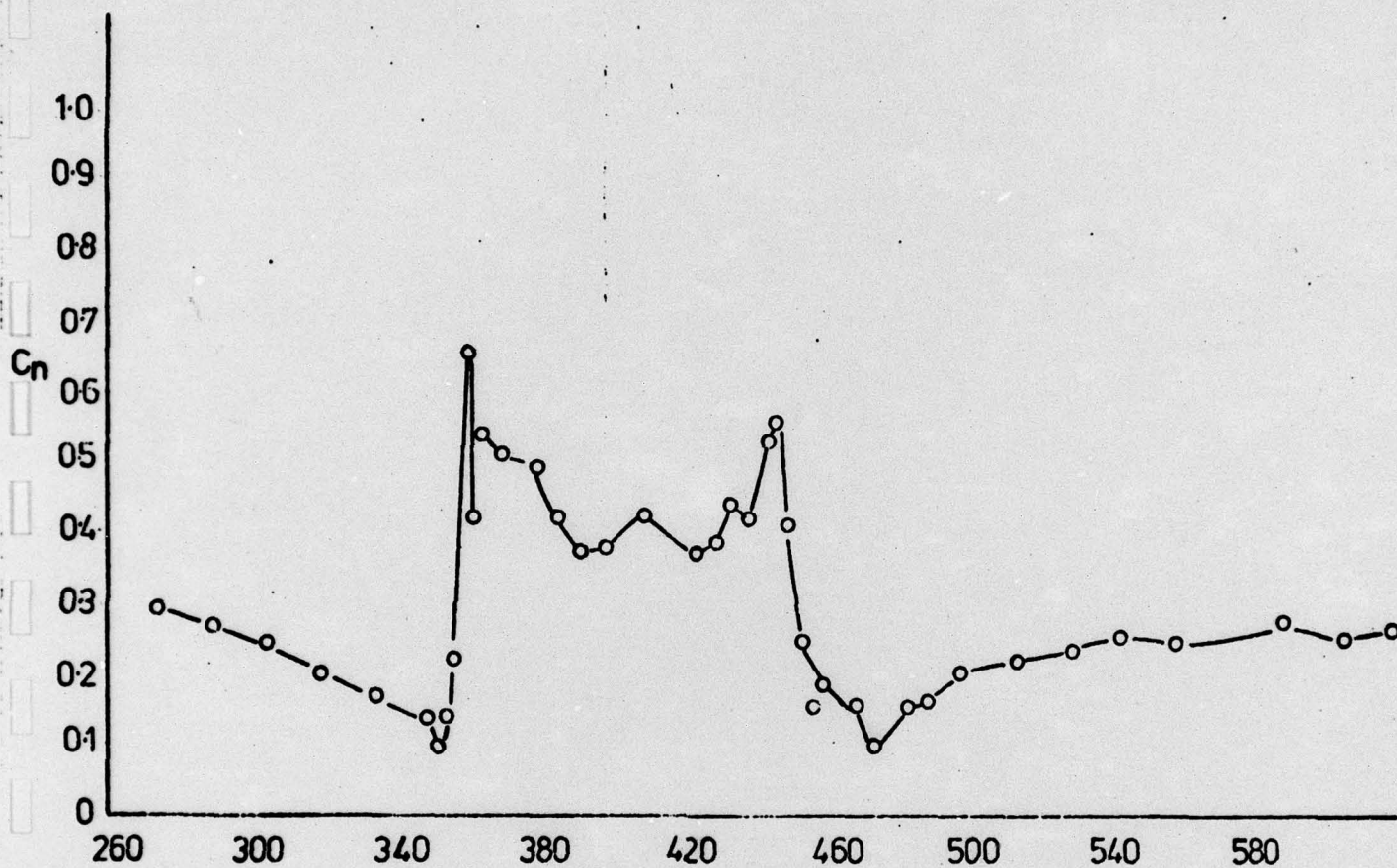
$i = -4.0^\circ$

$R_e = 1.70 \times 10^5$

$\theta = 104^\circ$



CIRCUMFERENTIAL VARIATION OF ROTOR INTEGRATED
 NORMAL FORCE COEFFICIENT FOR $N = 1250$ rev/min
 OPEN THROTTLE SCREEN $K = 3.183$ 90° SECTOR



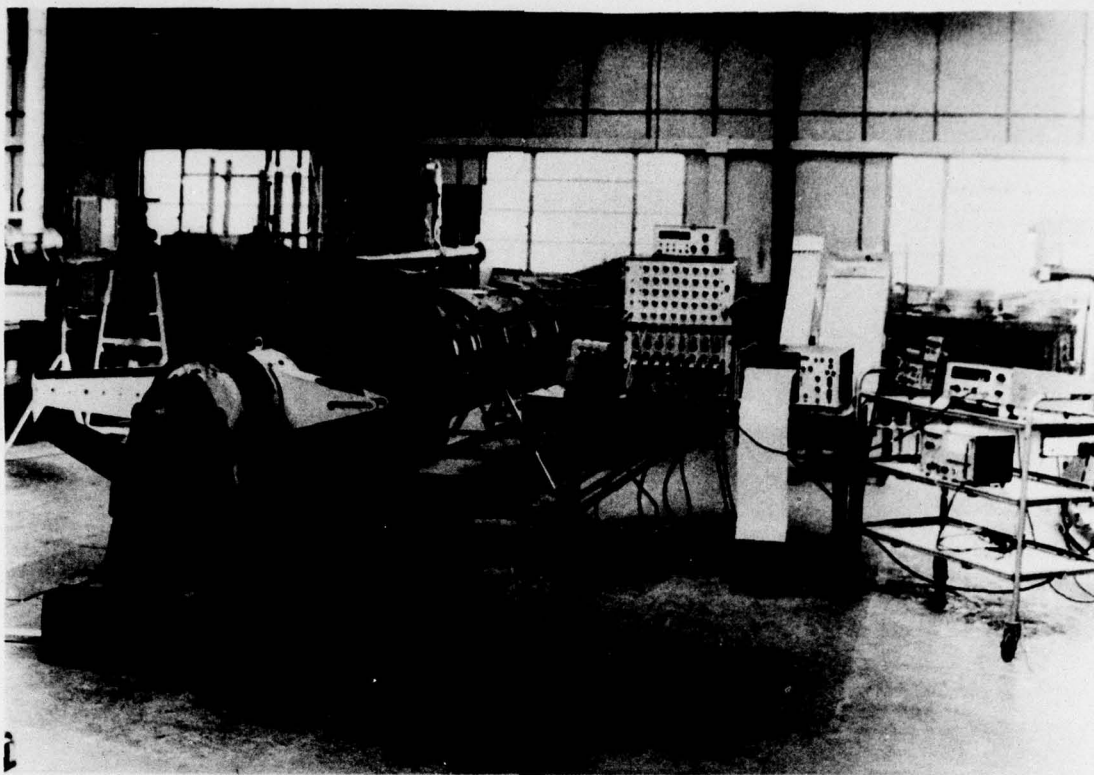


PLATE 1 VIEW OF RESEARCH COMPRESSOR AND PERIPHERAL INSTRUMENTATION

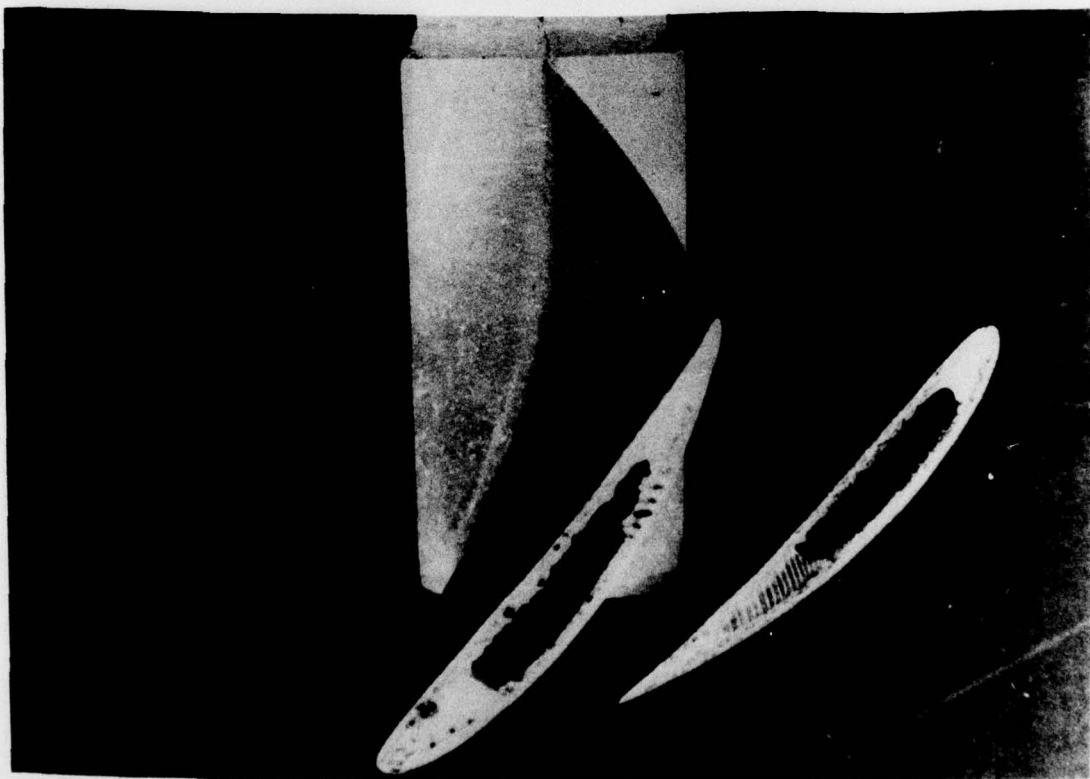


PLATE 2 VOIDS IN BLADE CASTING

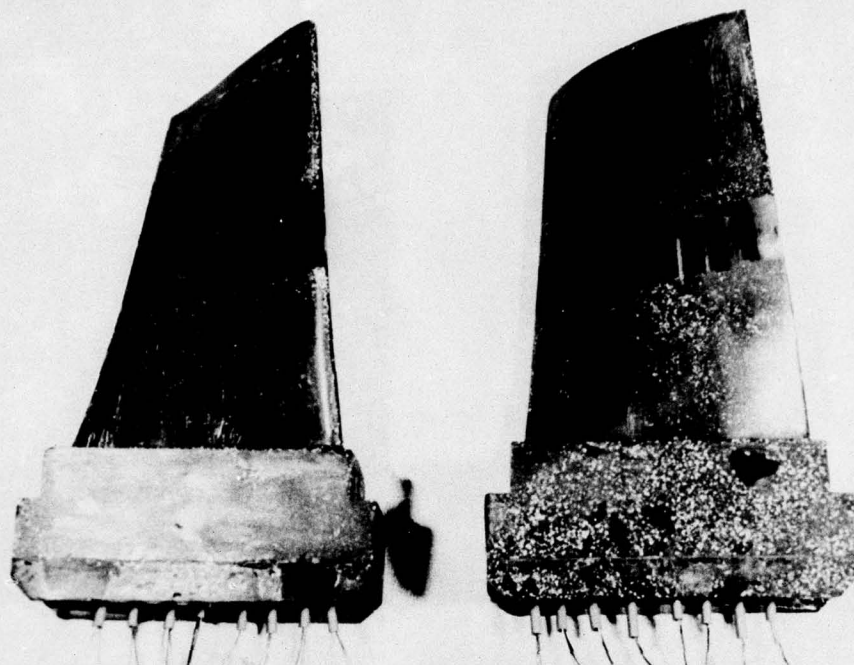


PLATE 3 ROTOR BLADES INSTRUMENTED AT MID-HEIGHT SECTION

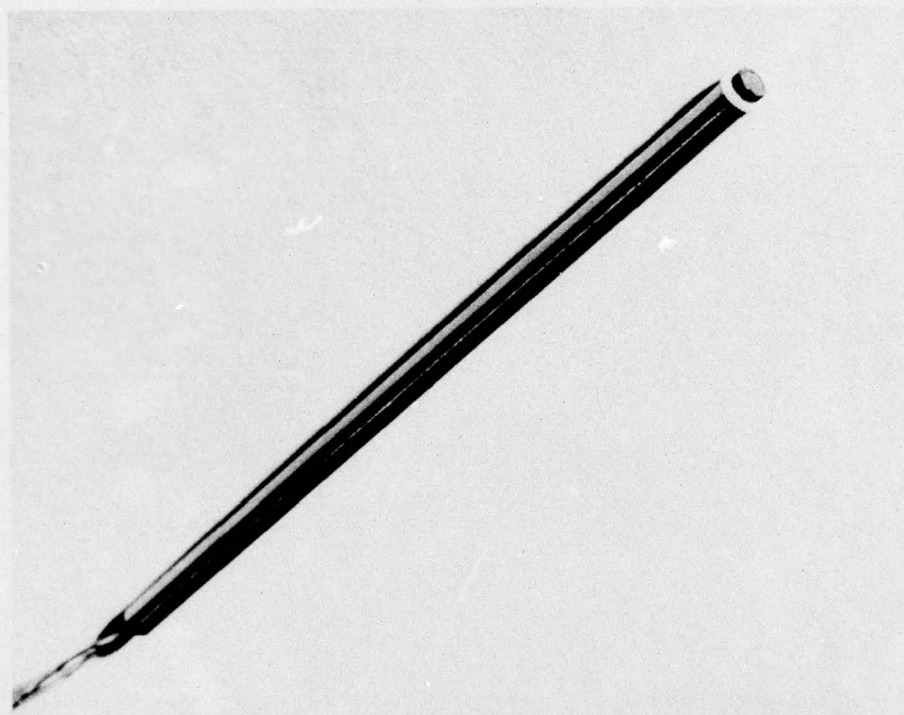


PLATE 4 TRANSDUCER MOUNTING

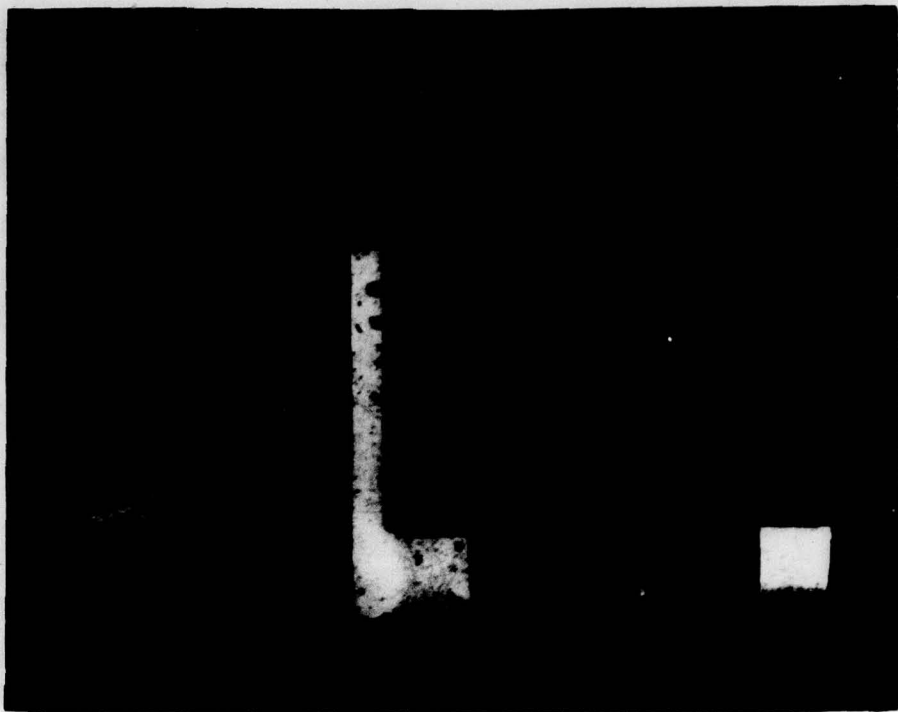


PLATE 5 TRANSDUCER LOCATION IN BLADE WITH STATIC PRESSURE HOLE

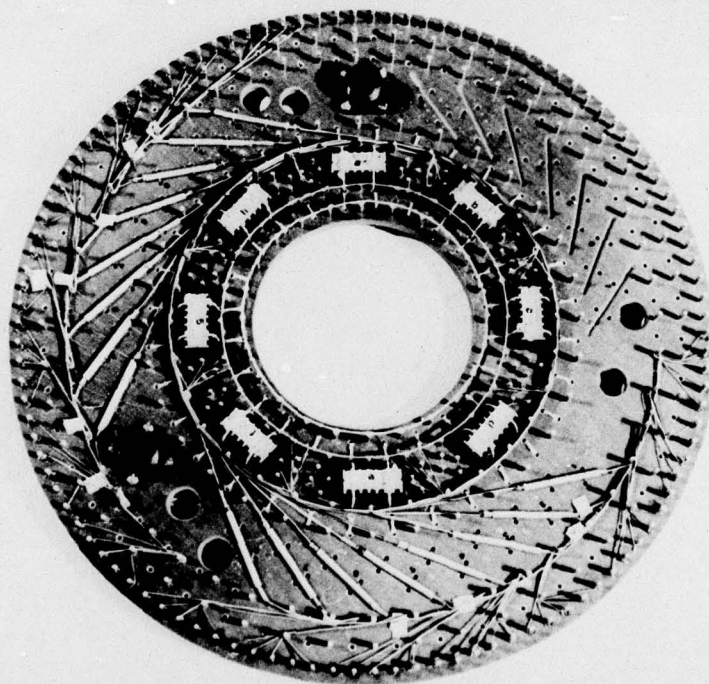


PLATE 6 ROTOR MOUNTED PROCESSING BOARD

19 REPORT DOCUMENTATION PAGE		READ INSTRUCTIONS BEFORE COMPLETING FORM
1. REPORT NUMBER (18) AFOSR-TR-77-0075	2. GOVT ACCESSION NO.	3. RECIPIENT'S CATALOG NUMBER
4. TITLE (and Subtitle) (6) SQUARE-WAVE CIRCUMFERENTIAL PRESSURE DISTORTION EFFECTS IN COMPRESSORS	5. TYPE OF REPORT & PERIOD COVERED (9) FINAL rept. 15 Apr 1975-15 Jun 1976	
7. AUTHOR(s) (10) R. E. PEACOCK	6. PERFORMING ORG. REPORT NUMBER	
9. PERFORMING ORGANIZATION NAME AND ADDRESS CRANFIELD INSTITUTE OF TECHNOLOGY SCHOOL OF MECHANICAL ENGINEERING CRANFIELD, BEDFORD, GREAT BRITAIN	8. CONTRACT OR GRANT NUMBER(s) (25) VAF AFOSR 2708-74	
11. CONTROLLING OFFICE NAME AND ADDRESS AIR FORCE OFFICE OF SCIENTIFIC RESEARCH/NA BLDG 410 BOLLING AIR FORCE BASE, D C 20332	10. PROGRAM ELEMENT, PROJECT, TASK AREA & WORK UNIT NUMBERS (16) 978140147 61102F	
14. MONITORING AGENCY NAME & ADDRESS (if different from Controlling Office) (13) 110 p.	12. REPORT DATE (11) Mar 1977	
	13. NUMBER OF PAGES 107	
	15. SECURITY CLASS. (of this report) UNCLASSIFIED	
16. DISTRIBUTION STATEMENT (of this Report) Approved for public release; distribution unlimited.		
17. DISTRIBUTION STATEMENT (of the abstract entered in Block 20, if different from Report)		
18. SUPPLEMENTARY NOTES		
19. KEY WORDS (Continue on reverse side if necessary and identify by block number) TURBOMACHINERY COMPRESSORS UNSTEADY AERODYNAMICS INLET MALDISTRIBUTION EFFECTS		
20. ABSTRACT (Continue on reverse side if necessary and identify by block number) A lightly loaded single stage compressor, in whose intake was set a series of distortion screens, was used in an experimental program to determine the effect of square-wave distortions on overall performance and detailed internal aerodynamics. It was found that a cross-coupling effect existed between the rotor and screen and under certain operating conditions this produced an asymmetry in the generated distortion. On rotor measurements recording the unsteady response of the rotor row to the distortion it was found that, for the operating point investigated, the rotor did not go into a previously observed dynamic stall. As		

✓ a consequence it was possible to relate the stall behaviour of the rotor to the observed cross-coupling. Two sets of rotor blades were used and it was found that with a low aspect ratio, away from the design incidence, the pressure distributions were disturbed by what are concluded tentatively to be three-dimensional effects. ✕

UNCLASSIFIED